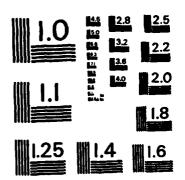
OPTICAL INVESTIGATIONS OF RECOMBINATION PROCESSES IN LASER-ANNEALED AND T. (U) CALIFORNIA UNIV SANTA BARBARA J L MERZ AUG 82 RADC-TR-82-226 F19628-79-C-0128 F/G 20/5 AD-A121 147 1/3 UNCLASSIFIED NL Ĭ.



MICROCOPY RESOLUTION TEST CHART MATIONAL BUREAU OF STANDARDS-1963-A



RADC-TR-82-226
Final Technical Report
August 1982



OPTICAL INVESTIGATIONS OF RECOMBINATION PROCESSES IN LASER-ANNEALED AND THERMALLY-ANNEALED SEMICONDUCTORS

University of California

James L. Merz

APPROVED FOR PUBLIC RELEASE; DISTRIBUTION UNLIMITED

ROME AIR DEVELOPMENT CENTER Air Force Systems Command Griffiss Air Force Base, NY 13441



E

This report has been reviewed by the RADC Public Affairs Office (PA) and is releasable to the National Technical Information Service (NTIS). At NTIS it will be releasable to the general public, including foreign nations.

RADC-TR-82-226 has been reviewed and is approved for publication.

APPROVED:

KENNETH J. SODA, Capt, USAF

Project Engineer

APPROVED:

HAROLD ROTH, Director

Solid State Sciences Division

FOR THE COMMANDER: On P. Kuss

JOHN P. HUSS

Acting Chief, Plans Office

If your address has changed or if you wish to be removed from the RADC mailing list, or if the addressee is no longer employed by your organization, please notify RADC (ESO), Hanscom AFB MA 01731. This will assist us in maintaining a current mailing list.

Do not return copies of this report unless contractual obligations or notices on a specific document requires that it be returned.

SECURITY CLASSIFICATION OF THIS PAGE (When Deta Entered)

	N PAGE READ INSTRUCTIONS BEFORE COMPLETING FORM
1. REPORT NUMBER	2. GOVT ACCESSIONN . 3. RECIPIENT'S CATALOG NUMBER
RADC-TR-82-226	H12/14.
4. TITLE (and Subtitle)	S. TYPE OF REPORT & PERIOD COVERED
OPTICAL INVESTIGATIONS OF RECOM	
PROCESSES IN LASER-ANNEALED AND	
ANNEALED SEMICONDUCTORS	6. PERFORMING ORG. REPORT NUMBER N/A
7: AUTHOR(a)	8. CONTRACT OR GRANT NUMBER(s)
James L. Merz	F19628-79-C-0128
James L. Mel2	12,020
PERFORMING ORGANIZATION NAME AND ADDRE	10. PROGRAM ELEMENT, PROJECT, TASK AREA & WORK UNIT NUMBERS
University of California	61102F
Santa Barbara CA 93106	2306J234
	23063234
1. CONTROLLING OFFICE NAME AND ADDRESS	12. REPORT DATE
Rome Air Development Center (ES	O) August 1982
Hanscom AFB MA 01731	13. NUMBER OF PAGES 216
14. MONITORING AGENCY NAME & ADDRESS(If ditte	
14. MORITORING AGENCY NAME & ADDRESS(II dille)	
Same	UNCLASSIFIED
	154. DECLASSIFICATION/DOWNGRADING
6. DISTRIBUTION STATEMENT (of this Report)	
Approved for public release; di	stribution unlimited
••	
•	
17. DISTRIBUTION STATEMENT (of the obstract enters	
17. DISTRIBUTION STATEMENT (of the abetract enter Same 18. SUPPLEMENTARY NOTES	ed in Block 20, il different from Report)
17. DISTRIBUTION STATEMENT (of the obstract enter	ed in Block 20, il different from Report)
17. DISTRIBUTION STATEMENT (of the obstract enter Same	ed in Block 20, il different from Report)
Same Same Same RADC Project Engineer: Kenneth	od in Block 20, if different from Report) Soda, Capt, USAF (ESO)
Same Same Same RADC Project Engineer: Kenneth	od in Block 20, if different from Report) Soda, Capt, USAF (ESO)
Same Same Same RADC Project Engineer: Kenneth	od in Block 20, if different from Report) Soda, Capt, USAF (ESO)
Same Same Same S. SUPPLEMENTARY NOTES RADC Project Engineer: Kenneth S. KEY WORDS (Continue on reverse side if necessary Laser beams Electron beams	od in Block 20, if different from Report) Soda, Capt, USAF (ESO)
Same Same Same S. SUPPLEMENTARY NOTES RADC Project Engineer: Kenneth S. KEY WORDS (Continue on reverse side if necessary Laser beams Electron beams	od in Block 20, if different from Report) Soda, Capt, USAF (ESO)
Same Same	Soda, Capt, USAF (ESO) and Identify by block number) Indium Phosphide
Same Same	Soda, Capt, USAF (ESO) and Identify by block number) Indium Phosphide
Same Same	Soda, Capt, USAF (ESO) and identify by block number) indium Phosphide and identify by block number) indium identify by block number) indium Phosphide
Same Same	Soda, Capt, USAF (ESO) and identify by block number) Indium Phosphide and identify by block number) EBIC) and low-temperature photoluminescences—carrier recombination processes in ion-
Same 18. SUPPLEMENTARY HOTES RADC Project Engineer: Kenneth 19. KEY WORDS (Continue on reverse side if necessary Laser beams Electron beams Pulse Heating Semiconductor Traps Silicon 10. ABSTRACT (Continue on reverse side if necessary Electron-beam-induced current (have been used to study minority planted Si subjected to scanned	Soda, Capt, USAF (ESO) and identify by block number) indium Phosphide and identify by block number) EBIC) and low-temperature photoluminescency-carrier recombination processes in ion- I laser or electron beam annealing. Dark
Same 18. SUPPLEMENTARY NOTES RADC Project Engineer: Kenneth 19. KEY WORDS (Continue on reverse side if necessary Laser beams Electron beams Pulse Heating Semiconductor Traps Silicon 10. ABSTRACT (Continue on reverse side if necessary Electron—beam—induced current (have been used to study minority planted Si subjected to scanned stripes parallel to the laser services.	Soda, Capt, USAF (ESO) and identify by block number) indium Phosphide and identify by block number) EBIC) and low-temperature photoluminescency-carrier recombination processes in ion- i laser or electron beam annealing. Dark scanning direction always appear in the EBI
Same 16. SUPPLEMENTARY NOTES RADC Project Engineer: Kenneth 19. KEY WORDS (Continue on reverse side if necessary Laser beams Electron beams Pulse Heating Semiconductor Traps Silicon 10. ABSTRACT (Continue on reverse side if necessary Electron-beam-induced current (have been used to study minority planted Si subjected to scanned stripes parallel to the laser side of study of laser-annealed samples.	Soda, Capt, USAF (ESO) and identify by block number) indium Phosphide and identify by block number)
Same 16. SUPPLEMENTARY NOTES RADC Project Engineer: Kenneth 19. KEY WORDS (Continue on reverse side if necessary Laser beams Electron beams Pulse Heating Semiconductor Traps Silicon 16. ABSTRACT (Continue on reverse side if necessary Electron-beam-induced current (have been used to study minority planted Si subjected to scanned stripes parallel to the laser sed isplay of laser-annealed sample increases with laser power, white	Soda, Capt, USAF (ESO) and identify by block number) indium Phosphide med identify by block number) indium Phosphide and id
Same Same Same S. SUPPLEMENTARY NOTES RADC Project Engineer: Kenneth S. KEY WORDS (Continue on reverse side if necessary) Laser beams Electron beams Pulse Heating Semiconductor Traps Silicon S. ABSTRACT (Continue on reverse side if necessary) Electron—beam—induced current (have been used to study minority planted Si subjected to scanned stripes parallel to the laser sed is play of laser—annealed samplincreases with laser power, white	Soda, Capt, USAF (ESO) and identify by block number) indium Phosphide and identify by block number)

SECURITY CLASSIFICATION OF THIS PAGE(When Data Entered)

the annealing laser beam, and that this laser-induced damage extends several microns below the implanted layer. On the other hand, electron-beam annealing yields a laterally uniform pattern and superior charge collection efficiency.

Deep Level Transient Spectroscopy (DLTS) is also used to study deep deflect levels in beam annealed silicon. A dominant hole (E_y + 0.45 eVO) was observed in CW laser-annealed samples immediately after sample preparation. In contrast, only a low concentration of hole traps appears in electron-beam-annealed Si. By correlating these results with published literature, the laser-induced quenched-in defects are identified as interstitial Fe and Fe-B pair reactions in Si. Possible sources of Fe in Si will be discussed.

COART	
GRA&I	
tab	4
ounced	ō
Pication_	
lability	
Special	-
-	
ì	
	ounced fication ibution/ lability



ABSTRACT

Part I: Minority-Carrier Recombination Processes and Electronically

Active Defects in CW Beam-Annealed Si

In recent years, high-intensity beam sources have been used to anneal the ion-implantation damage in Si. The beam-annealing idea was supported by some early encouraging results: the recrystallized lattice structure appeared to be defect-free and the resulting electrical activation was 100%. However, to explore beam annealing as a new technology for device fabrication, minority-carrier effects and electronic active defects in beam annealed Si must be investigated.

Electron-beam-induced current (EBIC) and low-temperature photoluminescence have been used to study minority-carrier recombination processes in ion-implanted Si subjected to scanned laser or electron beam annealing. Dark stripes parallel to the laser scanning direction always appear in the EBIC display of laser-annealed samples. The contrast of these dark stripes increases with laser power, while the charge collection efficiency decreases. Both EBIC and photoluminescence results indicate that damage is induced by the annealing laser beam, and that this laser-induced damage extends several microns below the implanted layer. On the other hand, electron-beam annealing yields a laterally uniform pattern and superior charge collection efficiency.

Deep Level Transient Spectroscopy (DLTS) is perhaps the most recent and most popular capacitance method for the study of deep

defect levels in semiconductors. The background of this technique will be briefly reviewed. A dominant hole trap ($E_{_{\mbox{\scriptsize V}}}$ + 0.45 eV), whose concentration increases by more than one order of magnitude with increasing laser power, was observed in CW laser-annealed samples immediately after sample preparation. In contrast, only a low concentration of hole traps appears in electron-beam-annealed This laser-induced defect is not stable at room temperature; instead it decays as a function of time and transmutes to a shallow level at E_v + 0.10 eV. The recovery of the E_v + 0.45 eV level can be stimulated by low-temperature annealing or by minority carrier injection. For the furnace-annealed control samples, rapid quenching from sufficiently high temperature into water produces the same defect energy level and annealing characteristics as the laser-induced defects. By correlating these results with those in the published literature, the laser-induced quenched-in defects are identified as interstitial Fe and Fe-B pair reactions in Si. Possible sources of Fe in Si will be discussed.

Part I of this report was written as a dissertation by Neng-Haung Sheng, and was submitted in partial satisfaction of the requirements for the degree of Doctor of Philosophy in the Department of Electrical and Computer Engineering, University of California, Santa Barbara.

ABSTRACT

Part II: LASER ANNEALING OF InP

CW Ar $^+$ laser annealing is used to activate semi-insulating InP after ion-implantation with Se. Electrical activation has been measured for a wide range of implant doses $(3\times10^{12}-5\times10^{15}~{\rm cm}^{-2})$ using a phosphosilicate glass cap during laser annealing. The dependence of the resulting electrical properties on laser power and scan speed are investigated in terms of surface decomposition and slip line formation.

Part II of this report was written as a journal article by M. Mizuta and J.L. Merz, and was submitted for publication in the Journal of Applied Physics.

TABLE OF CONTENTS

		<u>Di</u>	age
PART	I:	Minority-Carrier Recombination Processes and Electronically Active Defects in CW Beam-Annealed Silicon	
CHAP	TER 1	- INTRODUCTION	1
	1.1	Ion Implantation - Problems and Perspectives	1
	1.2	Beam Annealing	2
		References	7
CHAP	TER 2	- CW BEAM-ANNEALING OF ION-IMPLANTATION DAMAGE	8
	2.1	Ion-Implantation Process	8
	2.2	CW Laser-Annealing Apparatus	10
	2.3	Scanning-Electron-Beam-Annealing Apparatus	14
	2.4	CW Beam-Annealing Processes	15
	2.5	Mechanisms and Important Parameters for CW Beam-	
		Annealing	17
	2.6	Principal Majority-Carrier Results in the Implanted	
•		Layer	25
		References	29
CHAP	TER 3	- ELECTRON-BEAM-INDUCED-CURRENT INVESTIGATION OF CW	
		BEAM-ANNEALED Si	31
	3.1	Sample Preparation	32
	3.2	EBIC Measurements	33
	3.3	EBIC Evaluation of Laser-Annealed Si	38
	3.4	Substrate Temperature Dependence for Laser Annealing	48
	3.5	FRIC Evaluation of Flectron-Ream-Annealed Si	48

			oage
3	3.6	Determination of Minority-Carrier Diffusion Length	
		by EBIC	56
3	3.7	Relation of Laser-Induced Damage with Original	
		Crystal Quality	63
3	3.8	The Nature of Laser-Induced Damage	67
		References	74
CHAPTE	ER 4	- LUMINESCENCE INVESTIGATION OF LASER-ANNEALED ST	77
4	4. 1	Luminescence and Exciton States	77
4	4.2	Experimental System	81
4	4.3	Photoluminescence Evaluation of Laser-Annealed Si	83
4	4.4	Defect Luminescence in CW Laser-Annealed Si	91
		References	96
CHAPTE	ER 5	- DEEP LEVELS IN CW BEAM-ANNEALED Si	98
Ş	5.1	Transient Response of a Semiconductor Junction with	
		Traps and DLTS Spectrum	100
į	5.2	DLTS Spectrometer System	112
5	5.3	Sample Preparation for DLTS Measurement	115
į	5.4	Deep Levels in Ion-Implanted Si after Beam-Annealing	116
	5.5	Thermal Behavior of Laser-Induced Defects	122
į	5.6	Recombination-Enhanced Defect Reaction	129
	5. 7	Deep Levels in Laser-Annealed Self-Implant Si	133
;	5.8	Comparison with Furnace-Annealed Control Samples	136
;	5.9	Identification of Quenched-In Defects in CW Laser-	
		Annealed Si	138

		page
5.10	O Sources of Fe in Si	140
	References	147
CHAPTER	6 - CONCLUSIONS	150
6.1	Summary	150
6.2	Discussions	152
	References	157
Part II:	CW Laser Annealing of InP	
CHAPTER	7 - CW LASER-ANNEALING OF InP	158
7.1	Introduction	158
7.2	Experimental	160
7.3	Results and Discussion	161
7.4	Conclusion	180
	References	181
APPENDIC	ES	184
A	STEPPING-MOTOR CONTROLLER	184
В	DLTS SIGNAL PROCESSOR	195
r	TEMPERATURE-SCANNING LINIT	200

1.1 <u>Ion Implantation - Problems and Perspectives</u>

Ion-implantation is a well-known, important technique for doping semiconductors for device fabrication. In this process, the dopant atoms are implanted into the semiconductor surface by ionizing and accelerating the impurity atoms to the desired energy, and impinging them upon the wafers. By controlling the impurity dose in the ion beam, and energy of the beam, very precise control over the doping process can be achieved. However, the primary and secondary collisions of the ions with the atoms of the host crystal produce crystallographic damage in the form of interstitials, vacancies and complexes of these. In the case of high-dose implantation, the crystalline structure of the surface of the semiconductor wafer is destroyed and becomes amorphous. The formation of this amorphous layer is accompanied by a distinctive change in the optical properties of the semiconductor surface. The reflectivity of the amorphous surface is different from that of single-crystal semiconductor, which gives a milky appearance to heavily implanted semiconductor surfaces. In addition, the implanted ions are generally located in electrically inactive sites. Consequently, implantation is followed by an annealing treatment to serve the purpose of crystallizing the amorphous layer, electrically activating the dopant atoms as well as reducing the degree of radiation damage in the crystal. Conventional furnace thermal annealing of implanted wafers, however, generally leads to several undesirable effects: (a) such a long-time, high-temperature solid-phase epitaxial process leads to undesirable changes of the doping profile. Inward diffusions of dopants and surface contaminants occur which degrade subsequent device performance, (b) the implanted and annealed region cannot be made to be entirely defect free by thermal annealing. A non-negligible density of dislocations is always present in such structures, (c) the heat treatment required following ion implantation can have a strong, adverse effect on the properties of the bulk crystal. In particular, the minority carrier lifetime in the bulk of the wafer can be reduced to values below that in the as-grown crystal. Therefore, one of the most important research directions for implantation doping physics is the search for ways to increase the efficiency of radiation defect annealing at reduced temperatures.

1.2 Beam Annealing

In recent years, high-intensity beam sources, such as lasers and electron beams, have been proposed as alternatives to conventional furnace annealing of ion-implantation damage in Si. These beam annealing ideas were initiated by Russian⁽¹⁾ and Italian⁽²⁾ research groups; they observed that the damage produced in the lattice during implantation can be annealed with intense pulses of laser radiation. This so-called "laser annealing" of the lattice damage offers a high degree of lateral control over the annealed

region of the device. Moreover, the annealing takes place on a time scale considerably shorter than that associated with conventional thermal-annealing processes, reducing the possibility of sample contamination or even decomposition. In this "giant-pulse" regime of laser annealing, the sample melts and recrystallizes in times of the order of several 100 nsec. Subsequently, another regime of laser annealing has been explored. (3,4) in which a scanned CW ion laser is used to produce a solid-phase epitaxial regrowth of the implanted layer in times of the order of milli-Both the pulsed and CW annealing regimes can also be effected by the use of electron beams instead of laser beams. A number of encouraging results have already been reported for laser annealing of implanted Si: the residual damage, as measured by Rutherford backscattering, is low after laser annealing, the percent of substitutional dopant impurities is high and the resulting electrical activity of annealed layers is good.

In particular, it has been reported that CW laser annealing of implanted Si with a scanned Ar^+ ion laser produces good-quality, defect-free single-crystal material over a reasonable range of laser power (approximately 80-95% of the laser power necessary to melt the Si crystal surface). (3-5) In some instances the solid solubility of the implanted species has been exceeded by laser annealing compared with thermal treatments. (6) The current pace of research on beam annealing of semiconductors was set by the hope of "low temperature" annealing of ion implantation without degrading

minority-carrier lifetime in the substrate. However, preliminary $DLTS^{(7)}$ and photoluminescence $^{(8,9)}$ studies have shown that electrically and optically active defects are present in the laser-annealed material. Such defects can dominate the minority-carrier lifetime, one of the most important indications of material quality for actual device performance. Therefore, beam annealing (using both lasers and electron beams) requires additional characterization using techniques which reflect minority-carrier effects rather than majority-carrier properties.

The aim of the research program described in this dissertation is to conduct an investigation of minority-carrier recombination processes and electronically active defects in ion-implanted silicon which have been annealed by a CW Ar laser or scanned electron The principal techniques to be employed to measure beams. minority-carrier effects include Electron-Beam-Induced-Current (EBIC) and photo-generated short-circuit currents (I_{photo}), lowtemperature photoluminescence (PL), and Deep-Level-Transient-Spectroscopy (DLTS). Preliminary EBIC results were reported earlier on CW Ar laser-annealed Si using a spiral anneal pattern system. (10) Faint circular variations of charge collection were observed but not given serious attention. Although electrically and optically active defects have been detected by the pioneering $DLTS^{(7)}$ and photoluminescence studies (8,9) as mentioned above, however, the origin of these active defects was not clear. Two

different mechanisms for the origin of these defects can be proposed; the incomplete removal of ion-implantation damage, and laser-induced defect introduction resulting from the interaction between the laser beam and the crystal. The respective contributions of these two mechanisms have, however, not yet been established. The identification of these active defects is by no means trivial; to date there is no evidence that oxygen, for example, is involved in this defect, as was suggested earlier by Johnson et al. (7) Optimum beam-annealing conditions for minimum defect densities have not been clearly identified. These questions must be answered to evaluate the potential of this new technology.

This dissertation is organized as follows. The next chapter introduces CW laser-annealing and scanned-electron-beam annealing systems and techniques. The majority-carrier results published in the literature will be summarized. The results of Electron-Beam-Induced-Current (EBIC) mode of the SEM used to investigate the beam-induced damage in Si are reported in the third chapter. These experiments show that the laser power "window" for successful laser annealing is quite narrow; low charge-collection efficiency and dark stripe images on the EBIC display usually result. Superior results are obtained with the use of a scanning electron beam for annealing. In Chapter 4, low-temperature photoluminescence was used as a minority-carrier probe to investigate the perfection of laser-annealed Si. At relatively high laser power, the radiative recombination efficiency decreases. Both EBIC and photolumines-

cence results indicate that the laser-induced damage is produced deeper in the substrate than the implanted layers. The results of Deep Level Transient Spectroscopy (DLTS) used to investigate deep levels in beam-annealed Si are reported in Chapter 5. laser annealing, a dominant hole trap (E_v + 0.45eV), whose concentration increases by more than one order of magnitude with increasing laser power, has been measured in slip-free samples. In contrast, only a low concentration of hole traps appears in electron-beam-annealed Si. This laser-induced deep level is not stable at room temperature; it decays with time and transmutes to another shallower level, $\rm E_{_{V}}$ + 0.10eV. The recovery of the deep level at $E_{\rm V}$ + 0.45eV can be stimulated by low temperature thermal annealing (100-200°C) and by minority-carrier injection. For the furnace-annealed control samples, rapid quenching from sufficiently high temperature into water produces the same defect energy levels and annealing characteristics as that for laser-induced defects. annealing characteristics of laser-induced defects and thermally induced, quenched-in defects are correlated with interstitial Fe and Fe-B pair reactions in Si. Finally, conclusions will be drawn at the end of this dissertation.

REFERENCES

- E.I. Shtyrkov et al., Sov. Phys. Semicond. 9, 1309 (1976);
 A.Kh. Antonenko et al., ibid 10, 81 (1976); O.G. Kutukova et al., ibid 10, 265 (1976).
- H.D. Geiler et al., Phys. Stat. Sol. (a) 41, K171 (1977); G. Foti et al., Appl. Phys. 14, 189 (1977); J. Krynichi et al., Phys. Lett. A61, 181 (1977).
- 3. A. Gat, J.F. Gibbons, V.R. Deline, P. Williams, and C.A. Evans, Jr., Appl. Phys. Lett. 32, 276 (1978).
- L.D. Hess, R.A. Forber, S.A. Kokorowski, and G.L. Olson, Proc. Soc. Photo-Opt. Instr. Engineers <u>198</u>, 31 (1979).
- D.H. Auston, J.A. Golovchenki, P.R. Smith, C.M. Surko, and
 T.N.C. Venkatesan, Appl. Phys. Lett. 33, 539 (1978).
- 6. A. Lietoila, J.F. Gibbons, T.J. Magee, J. Peng, and J.D. Hong, Appl. Phys. Lett. 35, 532 (1979).
- N.M. Johnson, R.B. Gold, and J.F. Gibbons, Appl. Phys. Lett. 34, 704 (1979).
- R.A. Street, N.M. Johnson, and J.F. Gibbons, J. Appl. Phys. 50, 8201 (1979).
- 9. R.A. Street and N.M. Johnson, <u>Laser and Electron Beam Processing of Materials</u>, edited by C.W. White and P.S. Peercy (Academic Press, New York, 1980), p. 435.
- H.J. Leamy, S.D. Ferris, G.L. Miller, W.L. Brown, and G.K. Celler, <u>Laser-Solid Interactions and Laser-Processing-1978</u>,
 AIP Conf. Proc. No. 50, edited by S.D Ferris, H.J. Leamy, and J.M. Poate, (Amer. Inst. of Physics, New York, 1979), p. 556.

CHAPTER 2. CW BEAM ANNEALING OF ION-IMPLANTATION DAMAGE

Ion-implantation, CW laser-annealing and scanning-electron-beam-annealing systems will be briefly described in this chapter. Important parameters which control beam-annealing processes will be discussed. The principal majority-carrier results in the implanted layer will be summarized.

2.1 Ion-Implantation Process

The physical principles and experimental details of ion implantation have been reviewed by several books, especially one by Dearnaley et al., (1) and will not be repeated here. However, some special features associated with the UCSB implanter will be discussed in this section. A 200 keV heavy-ion accelerator with hot cathode arc source, produced by Accelerators Inc., was used in this work. Since the versatility and success of an implantation facility is particularly dependent upon the quality of the ion source, considerable attention must be paid to select the right species from the mass spectrum. In general, the mass spectrum of the above implanter is much more complicated than that of the standard. (2) due to poor vacuum conditions or residual sources from previous runs. The identification of each species in the mass spectrum must be made by measuring the mass-separating magnetic current. According to the principle that a charged particle traveling through a homogeneous magnetic field is constrained to a circular

trajectory, its radius is given by the well-known expression $^{(1)}$

$$R = \frac{143.95}{B} \sqrt{\frac{MV}{n}} , \qquad (2.1)$$

where M is the ion mass (a.m.u), V is the accelerating voltage (volts), R is the radius of the ion trajectory (cm), B is the magnetic field (gauss), n is the charge state of the ion. Therefore, the ratio of the magnetic field for two different species a and b to have the same radius can be derived as

$$\frac{B_a}{B_b} = \frac{I_a}{I_b} = \sqrt{\frac{M_a V_a n_b}{M_b V_b n_a}}, \qquad (2.2)$$

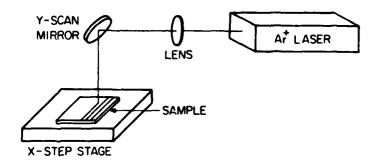
where I is the magnetic current which is linearly proportional to the magnetic field. The implanter used in this work has been calibrated by a Rutherford backscattering experiment in collaboration with Dr. L.C. Feldman at Bell Laboratories. The result shows that at 100 keV, the peak in the spectrum for a magnetic current of 96.5 ± 0.5 amp. corresponds to the As $^+$ ion. Using this result as the standard, the magnetic current required for any other species can be calculated from Eq. (2.2). The deviation was found to be within ± 0.5 amp. and the resolution of the mass spectrum can distinguish species with mass difference of one atomic mass unit (a.m.u.). The contamination by N_2^+ is serious, making it very difficult to implant Si^+ in this system because of the identical charge/mass ratio of these two species.

The other problem associated with the UCSB machine is the poor vacuum condition in the target chamber. It is known that ion-beam induced polymerization of absorbed hydrocarbons leads to the formation of a carbonaceous surface contamination layer on ion-implanted samples. The primary source of hydrocarbon molecules is the residual vacuum in the target chamber, $^{(3)}$ which takes more than two hours to be pumped to $\leq 10^{-6}$ Torr by a diffusion pump with a water baffle and liquid nitrogen cold trap. When the surface effect is important, such as in making Sckottky barriers after implantation and annealing, this vacuum condition is generally found to be unsatisfactory.

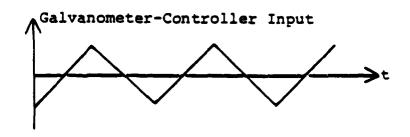
2.2 CW Laser Annealing Apparatus

An Ar⁺-ion laser with 20W maximum multiline (4579-5145Å) output was used for laser annealing. The strongest lines are at wavelengths of 5145 Å and 4880 Å. The basic scanning system used for our CW laser-annealing experiments is shown schematically in Fig. 2.1(a). In order to withstand high laser power, a quartz lens and a dielectric mirror (NRC model DM.5 488.0/514.5 nm) were used in this system. The laser output passes through the quartz lens and is deflected by the dielectric mirror, to be focused on the sample. The sample is held by a vacuum chuck which can be heated from room temperature to 400°C. The dielectric mirror is mounted on a galvanometer (model G-100 PD) which is driven by a controller (model CCX-101) under a servo control mode, which controls the

LASER ANNEALING (LA)



(a)



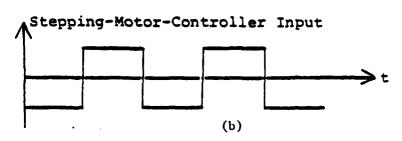


Fig. 2.1 (a) Schematic diagram of CW laser-annealing system. Y-scan mirror is driven by a galvanometer. X-step stage is driven by a stepping motor. (b) Input waveforms for the galvanometer controller and stepping-motor controller. The stepping motor is triggered at either positive or negative transition edges of the input square waveform.

scanning speed in the y-direction. Both the galvanometer and the controller are manufactured by General Scanning Inc. The sample holder is mounted on a translation stage which is driven by a 4-phase stepping motor (SLO-SYN Type SS25-1001) with a home-made controller for the x-step. The detailed circuit diagram and its functions can be found in Appendix A. A synchronous triangular waveform and square waveform, as shown in Fig. 2.1(b), from the outputs of a two-channel function generator (model HP 3300A) were used as input for the galvanometer controller and stepping-motor controller, respectively. The stepping motor was triggered to move one step only during either positive or negative transition edges of the square waveform. This arrangement permits the focused laser beam to be scanned across the sample in the y direction, stepped by a controlled x increment and then scanned back across the sample in the reverse y direction. The scanning speed in the y direction, v. was determined by

$$v = \frac{\Delta y}{1/2} \quad , \tag{2.3}$$

where Δy is the scanning width on the target and 1/T is the frequency of the function generator output. Maximum scanning speed was limited by two factors: (i) the peak-to-peak mechanical rotation of the galvanometer is 20° . (ii) the response time of the stepping motor is ~ 8 ms. Maximum operating frequency of 10 Hz is recommended. In the present system, the maximum scanning speed is

about 25 cm/sec, which can be improved by increasing the distance between the dielectric mirror and sample holder. The step size in the x direction can be 6 μ m, 12 μ m, 25 μ m, or 50 μ m. When the stepping-motor controller is modified with a simple external digital circuit, as shown in Appendix A, a step size of a few hundred microns can be achieved. Therefore, individual scan lines can be made either to overlap or not by appropriate adjustment of the x step. The laser beam diameter, a, (1/e width of the Gaussian beam) at the focal point can be calculated by the equation (4)

$$a = A \cdot \left[1 + \left(\frac{\pi A^2}{4f\lambda}\right)^2\right]^{\frac{1}{2}},$$
 (2.4)

where f is the focal length of the focal lens, λ is the laser wavelength (5145 Å), A is the laser beam diameter (1.58 mm) right after the aperture of the laser tube. Here it is assumed the laser output is a Gaussian beam, neglecting the beam divergence (0.56 mrad) since the distance between the aperture of the laser and the quartz lens is only about 20 cm.

For a focal length of 25 cm, the focused laser spot diaemter is about 103 µm as evaluated from Eq. (2.4). However, the assumption of Gaussian shape is generally found to be unsatisfactory, especially at high laser power. Under high-power conditions, the gain of the laser tube increases and higher-order modes are excited, making the output shape flatter, or even donut-like. This effect will be used to explain some data in the following chapters.

2.3 Scanning-Electron-Beam-Annealing Apparatus

For scanned-electron-beam annealing, a commercial ETEC scanning electron microscope was modified for a high-current mode of operation; this is done by removing the final stage aperture from the beam column to obtain sufficiently high beam currents for annealing. Beam currents as high as 150 µA were achieved at 30 kV accelerating voltage. The beam current was measured by a Faraday cup and the beam diameter was determined by measuring the scanning speed and the rise-time when the beam swept across the edge of a Faraday cup. All electron-beam anneals were done at room temperature.

The basic limitation of using a modified SEM for beam annealing is the sample size which can be annealed. This results from the fact that an increase in scanning angle produces an increase in distance between the sample and the final magnetic lens which is defined as the working distance. This problem is much more serious for scanning-electron-beam annealing (SEBA) than for laser annealing (LA) since the maximum working distance is less than 50 mm in the SEM, while a focal length of 250 mm is typically used in the CW laser-annealing system. In order to reduce this problem, maximum power of the modified SEM should be used in order to have long working distances and large beam diameters. The longest working distance at which the Si sample surface still can be melted by the maximum beam power (30 kV, 150 μ A) was found to be 26 mm. A 3 mm x 3 mm ion-implanted Si sample can be uniformly

annealed with a beam current more than 130 μA . This size sample is satisfactory for the material characterization discussed in the following chapters.

2.4 <u>CW Beam Annealing Processes</u>

Before each CW beam-annealing run, the focusing procedure as described in this section was carried out. Two-inch $\{100\}$ Si wafers implanted with As⁺ at 100 keV to a dose of 4 x 10^{15} cm⁻² (standard implant condition for much of this work) were scribed into \sim 5 mm x 5 mm samples, which were then used to search for the focal point. This energy and dose is sufficient to drive the Si surface amorphous to a depth of 1000 Å giving the sample a milky appearance due to the difference of reflectivity between amorphous Si and single crystal Si. Therefore, surface color and morphology changes were observed to determine the focal point. These samples were beam-scanned horizontally, nearly parallel to a <110> direction.

For laser annealing, 50 µm x-step size was used in the focusing procedure. After increasing the laser power to a certain level, a surface color-change occurred, indicating the onset of the transition from amorphous to single-crystal material. With increasing laser power, slip lines in <110> directions appeared on the wafer surface. Further increase of the beam power resulted in roughening of the central region of the stripe, indicating the occurrence of surface melting. The lens was then moved about 2 mm

towards the sample holder and another sample was irradiated with the melting laser power just found before. The roughening stripe width will either increase or disappear. If it increases, the sample is approaching the focal point, and the laser power should be reduced so that only the central narrow stripe melts. Then, the lens should be moved further toward the sample holder and the above procedure repeated. Whenever the roughening stripe width starts to disappear after moving the lens, the focal point has been passed and the lens should be moved backward. The focal point is thus determined to be the lens positions for which minimum laser power is required to induce narrow stripes of melted material under the same scanning conditions.

For electron-beam annealing, the working distance was initially fixed at 26 mm and 30 kV accelerating voltage was used in this work. The beam current was reduced by increasing the condenser current, and the normal SEM focusing procedure was then followed by adjusting the sample holder translation stage instead of by adjusting the working distance. After modification, the resolution of the SEM image is inferior to normal SEM operation; however, this procedure was found to be very useful for positioning the sample near the focal point. Maximum beam current can be achieved by reducing the condenser current to a minimum. The real focal point can be found by slightly adjusting the sample holder translation stage and beam current in a manner similar to the laser focusing procedure, until a near circular region is observed in the center

of the sample where there is evidence of dissociation or melt shown in Fig. 2.2(a) as observed by an optical microscope, and in Fig. 2.2(b) as observed with the EBIC mode of the SEM (whose principle will be discussed in Chapter 3); in the latter case, both the residual ion-implantation damage (dark stripes on the periphery of Fig. 2.2(b)), and electron-beam-induced defects (darker stripes between these, in the oval area in the center of Fig. 2.2(b)) can be clearly observed. One interesting phenomena is that the recrystallization of amorphous Si can be monitored in situ during electron-beam scanning by observing the appearance of the electronchanneling pattern on the cathode ray tube (CRT) display as shown in Fig. 2.3(a) for {100} and Fig. 2.3(b) for {111} samples. This reveals the recrystallization of the annealed lawers with the substrate crystal orientation during annealing. These electronchanneling patterns can not be observed with beam current below that required for recrystallization.

Typical beam-annealing conditions are given in Table I. Unless otherwise specified the results reported in this thesis are from samples annealed under these standard conditions.

2.5 Mechanisms and Important Parameters for CW Beam Annealing

It is well established that the recrystallization mechanism for both CW laser annealing and scanning electron beam annealing is solid-phase epitaxy $^{(5-7)}$. A heavy-dose ion implantation makes the front surface of Si amorphous as shown in A of Fig. 2.4. When this

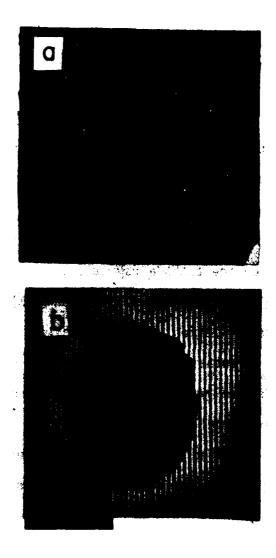


Fig. 2.2 Si surface dissociated or melted by a focused electron beam (a) optical micrograph. (b) EBIC micrograph where the darker stripes in the oval area in the center are due to electron-beam -induced defects. Adjacent beam scans are not overlapped and the residual amorphous Si can be observed as dark lines across the whole sample.

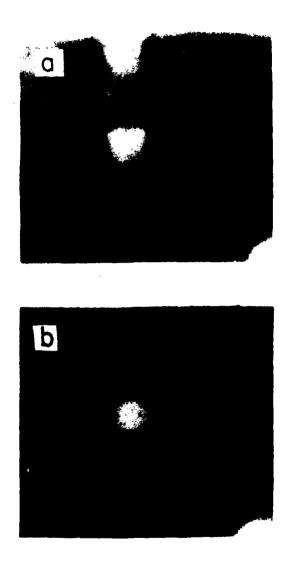


Fig. 2.3 Electron-channeling patterns taken "during" electron-beam annealing. (a) {100} (b) {111} samples.

TABLE I
BEAM ANNEALING PARAMETERS

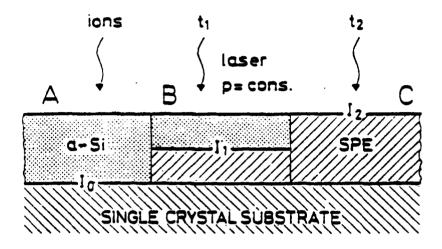
	LASER	ELECTRON-BEAM
	Spectra Physics Argon laser Model 171-19	ETEC Scanning Electron Microscope modified for high current operation
Substrate temperature	250°C	20°C
Beam power	10-15 W	130 ~ 150 µa at 30 kV
Working distance		26 mm
Beam size	100 µm	20 µm
X-step	6 µm	11 µm
Y-scan	6 cm/sec	20 cm/sec

amorphous surface was irradiated by CW lasers or electron beams, the regrowth starts at the interface between the amorphous layer and the underlying single crystal and proceeds to the surface. The temperature rise of the implanted layer induced by these beams determines the regrowth speed. If the dwell time of CW beam on the surface is sufficiently long, the recrystallization can be complete to the top surface as shown in C of Fig. 2.4. Therefore, for CW beam annealing, the mechanism is the same as conventional furnace annealing. The kinetics of solid-phase epitaxy for furnace annealing have been well studied by Rutherford backscattering and channeling experiments⁽⁹⁾. The epitaxial growth rate v can be expressed as a function of temperature with an activation energy of 2.3 eV

$$v[A/sec] = 1.55 \times 10^{14} exp(-2.3 eV/kT)$$
 (2.5)

From the above equation, the time required to regrow 500 Å of amorphous Si at 1000°C is less than 10 ms. Therefore, the typical dwell time for CW beam annealing is in the millisecond range.

The following assumption are usually made: the incoming beam flux acts as a heat source G, and the beam power P, is uniformly (instead of Gaussian distribution) absorbed in a circle of radius a in the (x,y) plane on the surface of a semiinfinite solid perpendicular to the direction of beam propagation (z). The temperature rise T induced by CW beams can then be estimated by solving the conduction heat transfer equation



Solid-phase epitaxy of implanted silicon

Fig. 2.4 Schematic representation of solid-phase epitaxial (SPE) reconstruction of an amorphous silicon layer. Frames A, B, and C show the initial implant and the intermediate and final stages of regrowth (after Ref. 8).

$$\nabla^2 T = \frac{C}{k} \frac{\partial T}{\partial t} - \frac{G}{k} \qquad , \tag{2.6}$$

where C is the heat capacity, k is the thermal conductivity, k/C has the units cm^2/sec of a diffusion constant, D. The time to reach steady state is approximately

$$t \sim \frac{a^2}{D} \qquad . \tag{2.7}$$

For silicon, the thermal diffusion constant at 1000°C is $0.12\,\text{cm}^2/\text{sec}^{(10)}$. Therefore, for a beam radius of 50 µm, it takes about 200 µsec to reach steady state. Thus, for dwell times of more than 1 msec, the steady state can easily be achieved. For simplicity, it is further assumed that k is constant and independent of temperature. The boundary condition that conductive heat flow from the single solid surface to the air may be neglected is $\partial T/\partial z = 0$ at the sample surface z = 0. The steady-state solution of Eq. (2.6) is then found to be⁽¹¹⁾

$$T(r,z) - T_0 = \frac{P}{\pi a k} \int_0^\infty e^{-\lambda z} J_0(\lambda r) J_1(\lambda a) \frac{d\lambda}{\lambda} , \qquad (2.8)$$

where T_0 is the substrate temperature as r and z become large compared with the beam radius a. Typically, the sample thickness is more than 10 mils and this semi-infinite assumption can be satisfied. J_0 and J_1 are zero-order and first-order Bessel functions of the first kind. At the central point of the beam spot, r = 0 and z = 0, the temperature is a maximum

$$T_{\text{max}}(0,0) - T_0 = \frac{P}{\pi a k} \int_0^\infty J_1(\lambda a) \frac{d\lambda}{\lambda} = \frac{P}{\pi a k} \qquad (2.9)$$

From this simplified derivation, the maximum temperature on the surface is linearly proportional to beam power divided by beam radius. P/a.

The temperature rise induced by a Gaussian beam intensity distribution that decays exponentially from the surface of the solid has been found by solving the heat diffusion Eq. (2.6), using a heat source term (12)

$$G(r,z) = \alpha \exp(-\alpha z) \frac{P}{\pi a^2} \exp(-\frac{r^2}{a^2})$$
, (2.10)

where α is the attenuation constant of the beam in the solid. Its maximum temperature on the surface is (12)

$$\tau_{\text{max}} - \tau_{\text{o}} = \frac{P}{2\sqrt{\pi} ka} \quad , \tag{2.11}$$

which differs from the simplified solution of Eq. (2.9) only by the constant $\sqrt{\pi/2}$. The more general steady-state temperature profiles with temperature-dependent thermal conductivity (14) and moving heat source (13,14) have also been calculated. In any case, the temperature rise on the sample surface is determined by the ratio of the power to the beam radius, which is the most critical parameter for CW beam annealing. Scanning speed and beam overlap determine the

dwell time and uniformity on the sample. Increasing the substrate temperature can reduce the beam power required for annealing, which also reduces the thermal gradient. In summary, beam power, beam size, scanning speed, beam overlap, and substrate temperature all control the beam-annealing results. In addition, for electron-beam annealing, the accelerating voltage is an extra important parameter which determines the energy deposition profile.

While the laser beam is exponentially attentuated as it enters the solids, the electron beam can penetrate deep into the solid. The resulting energy-deposition profiles are significantly different from those of the laser-annealing case. In Fig. 2.5, Neukermans et al. $^{(15)}$ use Monte Carlo technique to calculate the depth distribution of the deposited electron-beam energy as a function of depth in Si. For a 30 keV electron beam (which was used in these experiments for electron beam annealing), it can be seen that the effect of beam penetration becomes significantly more important in comparison with the absorption length of the ${\rm Ar}^+$ laser beam in single crystal Si (which is only $\sim 1\text{-}2~\mu{\rm m}$.) The thermal gradient in electron-beam annealing will therefore be considerably less than that for laser annealing.

2.6 Principal Majority-Carrier Results in the Implanted Layer

A number of encouraging results regarding the majority-carrier effects in the implanted layer have been reported for CW beam annealing of implanted Si. The techniques used include sheet

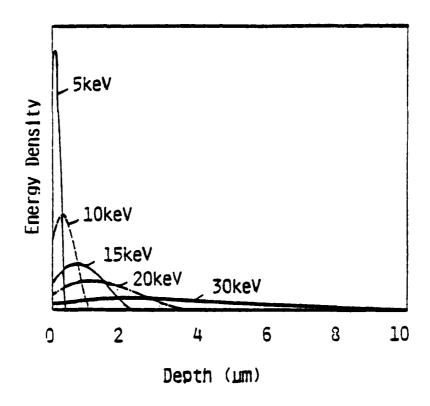


Fig. 2.5 Deposited energy versus depth in silicon as a function of the electron-beam energy (after Ref. 15).

resistivity and Hall mobility measurements, $^{(16)}$ Rutherford back-scattering (RBS) and channelling, $^{(16)}$ transmission electron microscopy (TEM) and ellipsometry. $^{(17)}$ Considerable time has been spent to insure that these results can be reproduced in our laboratory; however the details will not be reported here. The principal majority-carrier results can be summarized as follows:

- (a) The substitutional implanted impurities are high, and a resulting electrical activity of essentially 100% can be achieved. (18) In some instances the solid solubility of the implanted species has been exceeded by Taser annealing compared with furnace treatments. (19)
- (b) Because the dwell time of CW beam annealing is in the millisecond range, during this short time there is no significant redistribution of the implanted impurity. The impurity profile is identical to the as-implanted profile as measured by differential van der Pauw measurements, and confirmed by Secondary Ion Mass Spectroscopy (SIMS). (18)
- (c) In the case of shallow implants of boron and arsenic into $\{100\}$ Si, no residual disorder or damage can be detected by TEM after CW laser annealing. (16)
- (d) In {110} samples after CW laser annealing, a poly-Si ring can be seen in the diffraction patterns, and TEM micrographs show incomplete regrowth with some random structure. In the {111} case, the annealed layer shows even less reordering compared to {110}. (16)

- (e) The CW laser annealing of deep implants of arsenic or silicon in the <100> crystallograph direction results in a polycrystalline structure. (15) For majority-carrier effects, (d) and (e) are the basic limitations.
- (f) The mechanism for the recrystallization of an amorphous layer by CW beam annealing is solid-phase epitaxy. (5-7)

Although most of these results are quite encouraging, these measurement techniques have their limitations. For example, RBS is generally insensitive to low damage, and both RBS and TEM determine only structural imperfection irrespective of the electronic activity. As a new technology for device fabrication, minority-carrier recombination processes and electronically active defects must be investigated. Therefore, beam annealing requires additional characterization using techniques which reflect minority-carrier effects rather than majority-carrier properties.

REFERENCES

- G. Dearnaley, J.H. Freeman, R.S. Nelson, and J. Stephen, <u>Ion</u> <u>Implantation</u>, (North Holland, Amsterdam, 1973).
- R.G. Wilson, <u>Ion Mass Spectra</u>, (Wiley-Interscience, New York, 1974).
- M.Y. Tsai and B.G. Streetman, J. Electrochem. Soc. <u>126</u>, 98 (1979).
- 4. A. Yariv, Quantum Electronics, (Wiley, New York, 1975), 2nd edn., p. 177.
- D.H. Auston, J.A. Golovchenko, P.R. Smith, C.M. Surko, and
 T.N.C. Ventatesan, Appl. Phys. Lett. 33, 539 (1978).
- J.S. Williams, W.L. Brown, H.J. Leamy, J.M. Poate, J.W. Rodgers, D. Rousseau, G.A. Rozgonyi, J.A. Shelnutt, and T.T. Sheng, Appl. Phys. Lett. 33, 542 (1978).
- A. Gat, A. Lietoila, and J.F. Gibbons, J. Appl. Phys. <u>50</u>, 2926 (1979).
- 8. M. Wittmer and G.A. Rozgonyi, <u>Current Topics in Materials</u>
 Science, edited by E. Kaldis, (North-Holland, Amsterdam 1981).
- L. Csepregi, J.W. Mayer, and T.W. Sigmon, Appl. Phys. Lett.
 29, 92 (1976).
- C.Y. Ho, R.W. Powell, and P.E. Liley, J. Phys. Chem. Ref. data
 Suppl. 1, I-588 (1974).
- H.S. Carslaw and J.C. Jaeger, <u>Conduction of Heat in Solids</u>,
 (Oxford University Press, New York, 1959), 2nd edn., p. 216.

- 12. M. Lax, J. Appl. Phys. <u>48</u>, 3919 (1977).
- 13. M. Lax, Appl. Phys. Lett., 33, 786 (1978).
- Y. I. Nissim, A. Lietoila, R.B. Gold, and J.F. Gibbons, J. Appl. Phys. <u>51</u>, 274 (1980).
- A. Neukermans and W. Sperstein, J. Vac. Sci. Technol., <u>16</u>, 1847 (1979).
- 16. A. Gat, <u>CW laser-annealing of ion-implanted single crystal</u> silicon, (Coherent, Palo Alto, 1979).
- 17. K. Nakamura, T. Gotoh, and M. Kamoshida, J. Appl. Phys. <u>50</u>, 3985 (1979).
- A. Gat, J.F. Gibbons, T.J. Magee, J. Peng, P. Williams, V.
 Deline, and C.A. Evans, Jr., Appl. Phys. Lett. 33, 389 (1978).
- A. Lietoila, J.F. Gibbons, T.J. Magee, J. Peng, and J.D. Hong,
 Appl. Phys. Lett. <u>35</u>, 532 (1979).

CHAPTER 3. ELECTRON-BEAM-INDUCED-CURRENT INVESTIGATION OF CW BEAM-ANNEALED Si

The Electron-Beam-Induced-Current (EBIC) mode of a SEM is a powerful technique to characterize semiconductor material by providing a defect imaging mode and a quantitative measurement of charge collection efficiency. In this chapter, EBIC has been used to investigate the beam-induced defects in Si. For CW laser annealing of ion-implantation damage, the range of laser power over which good quality annealed material can be achieved is very limited, and is strongly dependent on the substrate temperature during annealing. At relatively low laser power, the recrystallization is not complete and collection efficiency is reduced by residual ion implantation damage. At relatively high laser power, laser induced damage is observed, and slip dislocations are introduced for laser power just below that required to melt the sub-Therefore, there is a compromise between annealing of ion-implantation damage and laser-induced defects. The optimum laser-annealing condition is obtained at a laser power just above the threshold for the initiation of annealing with a highly overlapping scan of a large diameter laser spot to improve lateral uniformity. Superior results are obtained with the use of a scanning electron beam for annealing: the range of beam power is broader, and the amount of beam overlap for subsequent scans required to achieve good annealing is less for the electron-beam case compared with the case of laser annealing.

3.1 Sample Preparation

Samples were implanted with energies between 40 and 160 keV and typical doses of 5×10^{14} - 2×10^{16} As ions/cm² into p-type Si substrates whose resistivity ranged from 5 to 20 ohm-cm. Other species like P or B have also been implanted on occasion for comparison. To compare our results with those obtained in other laboratories, a few samples were obtained from other sources. One set of samples was both implanted and Ar laser annealed at Stanford University, using their two-mirror scanning system previously described. (1) A second group was implanted at Xerox Corporation, El Segundo, and Kr or Ar laser annealed in our laboratory. However, unless otherwise indicated, all data reported here were obtained on samples both implanted and laser annealed in our laboratory.

After implantation and beam annealing, a clover-leaf pattern of mesa diodes were fabricated by standard photolithographic techniques and plasma etched into the top of the implanted area to form a van der Pauw-type pattern⁽²⁾ for sheet resistivity and Hall mobility measurements. Four metallized ohmic contacts at the corners were formed by aluminum evaporation and photolithography. Because the front surface was implanted with a heavy dose, no sintering cycle was required for ohmic-contact formation. This avoids any thermal treatment effects after beam annealing. For EBIC measurements, substrate ohmic contacts were formed in the following way: the In-metal wire was placed in contact with Ga for a few

moments to form a Ga-In eutectic on the surface of the wire. This was then rubbed gently on the back side of the sample to form the contact. The area of the top ohmic contacts was deliberately made smaller than the mesa area, as shown in Fig. 3.1; electrons can therefore penetrate directly into the sample for EBIC measurements.

3.2 EBIC measurements

The physical basis of the EBIC technique is simple. Its principle is shown in Fig. 3.1. The top of the sample is implanted (usually with As⁺) and annealed to become n-type, producing an n⁺-p junction in the p-type (B-doped) substrate. The shaded area represents the junction depletion region. The electron beam from the SEM produces excess electron-hole pairs in the semiconductor proportional to the beam energy (E_R) and beam current (I_R) . Minority carriers generated in the pear-shaped excitation region diffuse away from that region; those that reach the depletion region drift in the electric field of the junction. This charge collection results in a current, which can be displayed on a cathode ray tube. Because a minority carrier will recombine at defect centers or improperly annealed damage regions before reaching the depletion layer, such regions appear as dark areas because of a reduction in the charge collection efficiency. Thus, the CRT display provides a 2-D map of the region of high and low charge collection efficiency, corresponding to low and high defect density, respectively.

ELECTRON BEAM INDUCED CURRENT (EBIC)

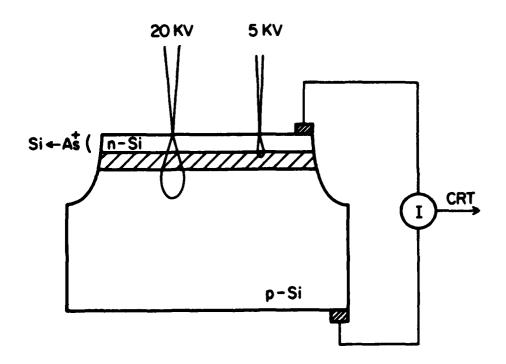


Fig. 3.1 Schematic diagram of the electron-beam-induced current experiments.

Moreover, depth information can also be obtained, since the penetration of primary electrons can be varied by changing the accelerating voltage. For example, the junction plane formed by a 100 keV As implant is approximately 0.2 to 0.3 µm from the surface whereas the penetration range of the electron beam in Si is $0.3~\mu m$ for 5 keV, and 3 µm for 20 keV. (3) Therefore, EBIC pictures taken with 5 kV accelerating voltage contain information mainly from the originally amorphous layer created by ion implantation, while the 20 kV pictures provide some substrate information. These effect are shown schematically in Fig. 3.1. Therefore, plotting charge collection efficiency as a function of accelerating voltage provides information on the relative depth of the recombination cen-Such arguments are, of course, qualitative; clearly, there is some ambiguity due to the profile of the electron beam in the sample, carrier diffusion, and other effects.

To compare similar samples which have been annealed with different laser power, EBIC displays were obtained with identical amplifier gain and incident electron beam current, measured using a Faraday cup. Since the current meter on the SEM at UCSB is calibrated for specimen current instead of induced current, an external current meter must be used to take meaningful quantitative data. Only then will it be possible to calculate back from the measured induced current to obtain the physical properties of the specimen. Typical beam currents were kept below 1 nA with a slightly defocused beam spot to eliminate possible nonlinear effects. To

assure that measurements were taken in the linear, small-signal region, data were checked by observing the linear variation of induced current with beam current. The total EBIC charge collection current, I_{EBIC} , was measured for each sample, and the charge collection efficiency, $\langle \eta \rangle$, was calculated $^{(4)}$ according to

$$\langle \eta \rangle = GI_{EBIC}/E_BI_B$$
 (3.1)

where G is the average energy required for electron-hole pair production and equals approximately three times the minimum energy gap in most semiconductors. For Si, G = 3.67 eV. In Eq. (3.1), $I_{\rm B}$ and $E_{\rm B}$ are the incident electron beam current and energy respectively.

In addition, each sample was used as a simple photodetector and illuminated by a microscope lamp whose spectrum can be considered as approximately black-body radiation, continuously ranging from visible to infrared. The density of photons in the semiconductor varies as

$$\Phi = \phi_0 \exp(-\alpha x) , \qquad (3.2)$$

where Φ is in the units of photon/sec-cm² and α is the absorption coefficient which is a function of wavelength. (5) For n-on-p diodes, the resulting short-circuit photo-current is (6)

$$I_{\text{photo}} = q\alpha\Phi_0 \left\{ \frac{L_h}{1-\alpha L_h} \left[\exp(-\alpha d) - \exp(-d/L_h) \right] + \frac{L_e \exp(-\alpha d)}{1+\alpha L_e} \right\}, (3.3)$$

where d is the junction depth, $L_{\rm e}$ and $L_{\rm h}$ are the minority-carrier diffusion lengths in the p-side and n-side respectively. Under the conditions that $\alpha L_{\rm e}$, $\alpha L_{\rm h}$ << 1, which can be satisfied for incident photon energy in the near infrared range (α < 10^3 cm⁻¹)⁽⁵⁾, then $\exp(-\alpha d) >> \exp(-d/L_{\rm h})$, and Eq. (3.3) can be reduced to

$$I_{photo} = q \alpha \Phi_o (L_e + L_h) \exp(-\alpha d)$$
, (3.4)

which is directly proportional to the sum of the minority-carrier diffusion length on both sides of the junction. However, for the case αL_e , $\alpha L_h >> 1$, which is more reasonable when the incident photon energy is in the visible range, (5) Eq. (3.2) is reduced to

$$I_{photo} = q \phi_o \exp(-d/L_h) , \qquad (3.5)$$

which is more sensitive to the minority-carrier effects on the top n-layer. From the simplified Eq. (3.4) and Eq. (3.5), it can be seen that the short-circuit photocurrent can be used as a measure of the average minority-carrier collection efficiency on both sides of the junction, with an exponential decay as the weighting function; this is clearly different from the electron-beam penetration case.

3.3 EBIC Evaluation of Laser-Annealed Si

A typical EBIC result of an As[†]-implanted n[†]-p junction annealed by a CW Ar[†] laser is shown in Fig. 3.2. In the upper and lower portions of this figure, the EBIC mode has been switched off so that a standard secondary-electron micrograph results. The laser-annealed sample appears to be smooth and defect-free in this mode, as anticipated. However, using the EBIC mode (center of Fig. 3.2), it is clear that laser annealing has produced quite non-uniform minority-carrier effects: high contrast dark lines appear which are parallel to the direction of laser scan. The EBIC darkline spacing is of the order of the laser scan step; the deviations from constant spacing (30 µm in this case) will be discussed later.

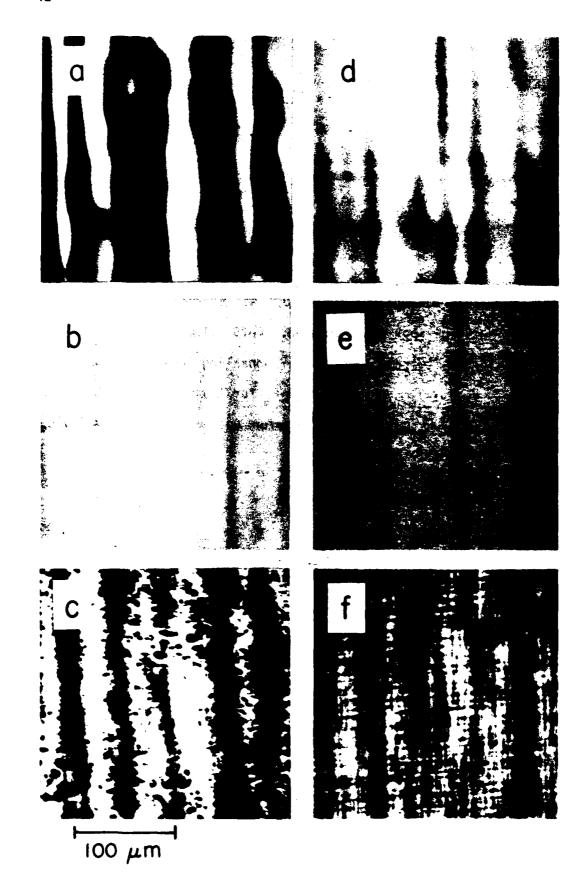
The sample shown in Fig. 3.2 is one of a series of "standard" samples processed at Stanford, the current leaders in CW beam annealing technology, under "optimum" conditions believed to result in good-quality, defect-free single-crystal material as mentioned in Chapter 2. It is clear, however, that laser annealing has produced quite nonuniform minority-carrier effects. Almost all samples studied here show such dark-line contrast. This dark-line contrast can result from two causes: (i) incomplete anneal due to insufficient laser power, allowing either a high density of residual defects or incomplete electrical activation of As donors; or (ii) damage induced by excess laser power, introducing defects which act as recombination centers. By systematic studies with different laser spot diameters (\sim 40 µm - 100 µm), step sizes (\sim 6



Fig. 3.2 EBIC micrograph (center) and secondary electron emission image (top and bottom) excited by 5-keV beam. The sample was implanted with $6\times10^{14}~{\rm As}^+$ ions/cm² and annealed with a 40-µm spot and 30-µm step. In the EBIC mode, dark regions correspond to low charge collection. Substrate temperature $T_S=250^{\circ}{\rm C}$.

 μ m - 50 μ m) and scanning speeds (~ 2 cm/sec - 15 cm/sec), improved results were obtained for a large-diameter laser beam (100 μ m), small x-direction scan step (6 μ m) and slow scan speed (6 cm/sec). High overlap not only improves the lateral uniformity of electrical activation, but also reduces the threshold of laser power required for recrystallization.

An example of the results obtained with these parameters is given in Fig. 3.3 and Fig. 3.4. The left column of Fig. 3.3 (Figs. 3.3a-d) shows the EBIC contrast pattern as a function of laser power using a 5 keV electron beam; the right column (Fig. 3.3e-h) shows patterns obtained on the same 4 samples using a 20 kV accelerating voltage. To make these results more quantitative, the dependence of $I_{\mbox{\scriptsize photo}}$ and the sheet resistivity, $\rho,$ on laser power are shown in Fig. 3.4 for the same set of samples. In this case, $\rho =$ 45 Ω/\square when the laser power is higher than 70% of the power required to melt the Si surface, P_M , as defined in Chapter 2. A Hall mobility $\mu_e = 40 \text{ cm}^2/\text{v-sec}$ was achieved. This corresponds to 100% activation for the implanted dose $As^+ = 4x10^{15} cm^{-2}$. For $P \le 0.6$ $P_{\mathbf{M}}$, little EBIC contrast is observed, but the value of $I_{\mathbf{photo}}$ is very low, as shown in Fig. 3.4. This value of P is clearly below the threshold for laser annealing. At P = 0.64 P_{M} , I_{EBIC} and I_{photo} increase, but strong contrast appears in the EBIC pattern for 5 keV injected electrons, as seen in Fig. 3.3(a), whereas little contrast is observed at 20 keV (Fig. 3.3(e)). When the laser power is inFig. 3.3 EBIC micrographs for 4×10^{15} As $^+$ ions/cm 2 annealed with a 100- μ m spot and 6- μ m step. Left column (a)-(d) for 5 and right (e)-(h) for 20 keV. Annealing laser power was 0.64 P_{M} for (a) and (e), 0.75 P_{M} for (b) and (f), 0.85 P_{M} for (c) and (g) and 0.92 P_{M} for (d) and (h). $T_{S} = 250^{\circ}$ C.



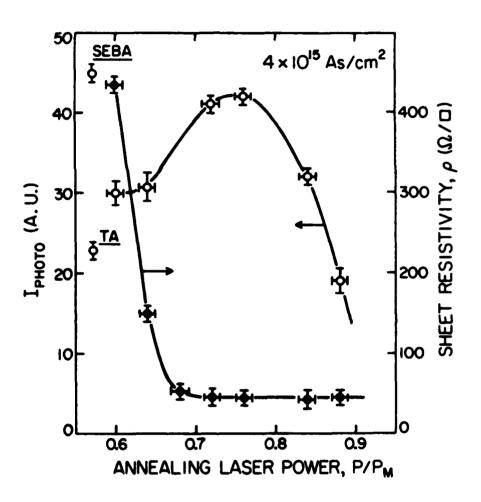


Fig. 3.4 Dependence of short-circuit current I_{photo} in arbitrary units and sheet resistivity ρ on annealing laser power P for 4×10^{15} As $^+$ ions/cm 2 sample with 100- μ m laser spot and 6- μ m step. Laser power is normalized by the melting power P_{M} . $T_{S} = 250^{\circ}$ C. Also shown are electron-beam-annealed (SEBA) and thermally-annealed (TA) samples.

creased slightly above the threshold power to achieve 100% activation of the implanted dopants, as shown in Fig. 3.4, $I_{p,hoto}$ reaches the maximum value at P = 0.75 P_M. For this sample, the dark lines are faint at 5 kV accelerating voltage (Fig. 3.3(b)) and almost featureless at 20 kV accelerating voltage (Fig. 3.3(f)). After increasing the laser power, P = 0.85 P_M, I_{photo} decreases with a corresponding increase in EBIC contrast at 5 kV (Fig. 3.3(c)). Moreover, strong EBIC contrast is also observable at 20 kV accelerating voltage (Fig. 3.3(g)). A further increase in laser power to P = 0.92 P_M produces a dramatic decrease in I_{photo} . In this case, a cross-hatched appearance is observed (Fig. 3.3(h)), resulting from the formation of slip dislocations due to the thermal gradient-induced stress at this high laser power.

These results are typical; very similar effects in which dark stripe contrast increases with laser power were observed in many sets of samples implanted with energies between 40 to 160 keV and doses of 1×10^{14} to 2×10^{16} As $^+$ ions/cm² prepared for these studies. These results are interpreted as follows. The true "window" for optimum laser annealing, as determined by minority-carrier charge collection, is quite narrow, corresponding to \sim 70 - 75% of $P_{\rm M}$. At lower P, the anneal is incomplete. At values of P above the peak, the charge-collection efficiency drops off rapidly. A very interesting range of laser power is observed which induces stripe-like damage but not slip dislocations; this is shown in Fig. 3.4 between the dashed line A and B. Line A indicates the optimal power, while

slip dislocations form when the laser power exceeds line B. In this range of laser power, the dark stripe contrast increases with laser power, especially at high accelerating voltage (20 kV; compare Fig. 3.3(f) and (g)), for which the electron range is \sim 3 μ m while the implanted amorphous layer is only about 0.2 μ m. This is a direct evidence of laser-induced damage, and this damage is clearly observed at high accelerating voltage, suggesting that the damage is deep, as discussed below.

The depth and/or density of this laser-induced damage increases with the laser power, as derived from the measured EBIC collection efficiency as a function of annealing laser power for different accelerating beam voltages, as shown in Fig. 3.5. For 20 kV and 30 kV accelerating beam voltages, the EBIC collection efficiency decreases at high laser power, and the corresponding contrast of dark lines in the EBIC display becomes more obvious, even before the appearance of slip dislocations. On the other hand, for low accelerating voltage, the EBIC collection efficiency increases with laser power. The recyrstallization near the surface is more complete near the surface at high laser power due to faster solid-phase epitaxial rate at higher temperature. Thus, the material near the surface appears to improve relative to the material deeper into the substrate as the annealing laser power is increased. Although it is difficult to extract accurate quantitative defect depth information from such experiments, the results with high accelerating voltage strongly suggest that the laser-induced

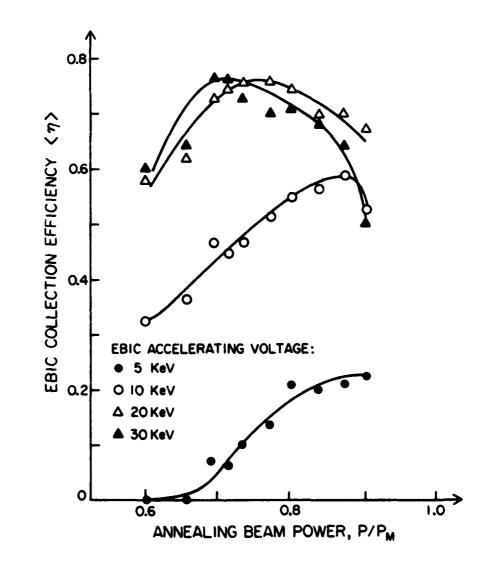


Fig. 3.5 Dependence of EBIC collection efficiency < η > on laserannealing power for different SEM accelerating voltages. The samples were implanted with As † as 100 keV to a dose of 4×10^{15} cm $^{-2}$ and annealed by CW laser.

damage may extend considerably deeper than the implanted amorphous layer. This is consistent with the profile of non-radiative defect centers measured by DLTS to be discussed in Chapter 5.

These dark lines were frequently found to be asymmetric with respect to the x-direction steps, and the spacing was not necessarily equal to the scan step. These effects can arise from a variety of causes, including the possibilities that: (i) the laser is not operating in the lowest-order TEM_{oo} mode. Higher order modes are excited at higher laser power. The multimode conditions appear as complex variations in the intensity pattern. Although the aperture control allows adjustment for true single-mode output, it also reduces the output power. As the aperture closes, the "donut" mode usually appears first, and then, as the aperture is closed further, the TEM₀₀ condition is established. Since high laser power is required to anneal Si, the aperture was usually left open in this work, so that single-mode conditions were not maintained. However, it is believed that laser annealing with a single-mode laser may not be advantageous, since the presence of higher modes "flattens out" the beam profile, making it easier to overlap successive (ii) each successive laser scan may be affected by the partial anneal produced by the preceding scan, resulting in an asymmetrical anneal profile. The multiple heating cycles during this process make the contrast more complex. (iii) the image resolution of EBIC display is limited by the generation volume. (7)

3.4 Substrate Temperature Dependence for Laser Annealing

The data shown in Fg. 3.6 determines the "window" for optimum laser annealing, as determined by these minority carrier measure-The dependence of this window on processing parameters is of considerable interest for device application. In Fig. 3.6 the effect on this window of changing the substrate temperature during laser annealing is shown. A somewhat arbitrary definition of the annealing window has been used as follows: the threshold power for good annealing corresponds to 100% activation, given by the point at which the sheet resistivity reaches a minimum value (e.g., P = $0.70~P_{\rm M}$ in Fig. 3.4). The upper limit for good annealing is defined as the power at which $I_{\mbox{\footnotesize photo}}$ is reduced to 80% of its maximum value. The melting power itself is dependent on substrate temperature (also shown in Fig. 3.6), as expected from calculation. Although no appreciable change in window width is observed over a wide range of temperature, it is noted that the position of the window with respect to the melting power is clearly dependent on substrate temperature. This is of particular importance for the practical application of Si laser processing.

3.5 EBIC Evaluation of Electron-Beam Annealed Si

In general, the use of the scanned electron beam from the electron microscope gives results that are somewhat similar but generally superior to those obtained with the scanned laser beam. A direct comparison between the two techniques is given in Fig.

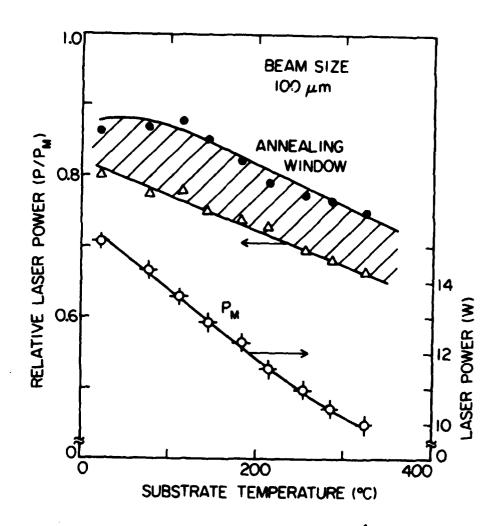


Fig. 3.6 Dependence of the laser power required for melting (P_M) , and the window for good annealing, on substrate temperature. Triangles give the threshold (i.e., lowest) power for good annealing, closed circles represent the upper-limit power for annealing as described in the text.

3.7, which shows samples that have been optimally annealed using the two techniques. For the laser-annealed sample, shown in Fig. 3.7(a), dark-line contrast is observable (though weak), while the EBIC display in the electron-beam annealed sample (Fig. 3.7(b)) is almost featureless. Correspondingly, the optimum value of $I_{\rm photo}$ is slightly higher for electron-beam than for laser annealing. This implies that the electron-beam-annealed sample has better lateral uniformity of the minority-carrier collection efficiency.

In Fig. 3.7, the laser annealing was performed with a high degree of overlap of each consecutive scan (i.e., more than 90% overlap). On the other hand, the degree of overlap required for uniform annealing using the electron beam is much less than that for laser annealing. This is shown in Fig. 3.8, with different degrees of electron-beam overlap. With an x-step of 44 µm, there is no overlap between successive scans (Fig. 3.8(c)); the unannealed portion remained amorphous, as confirmed by observing the reflectivity with an optical microscope; thus, dark lines appear in the EBIC display because of low charge collection. When the step is reduced to 22 μ m, the width of the dark lines is expected to be narrower as observed in Fig. 3.8(b). Finally, laterally uniform EBIC results have been obtained using an $11 \mu m$ step (Fig. 3.8(a)). The beam diameter was estimated to be \sim 20 μm by scanning it across a Faraday cup, although there is some ambiguity in determining this diameter, particularly because the electron beam spreads as it penetrates the sample. However, within the depth of the implanted

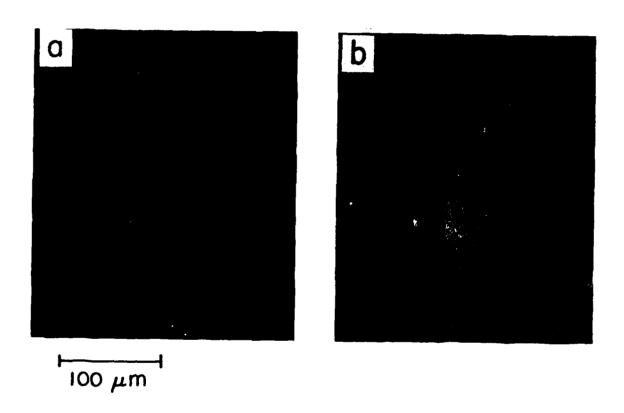


Fig. 3.7 EBIC micrographs for (a) laser annealing and (b) electronbeam annealing under optimal anneal conditions for each technique. An acceleration voltage of 5 kV was used for the measurements.

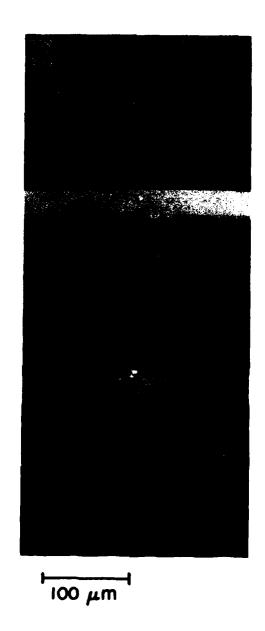


Fig. 3.8 EBIC micrographs for electron-beam annealing showing the effect of beam overlap. Scan step is (a) 11 μm , (b) 22 μm , (c) 44 μm . Diameter of electron beam is ~20 μm . A 5 keV electron beam was used in the EBIC measurements.

layer from the top surface (< $0.2~\mu m$), the beam blooming would be at most a small fraction of the original beam diameter, and is therefore probably insignificant. At any rate, this figure shows that less overlap is required for electron-beam compared to laser annealing.

Furthermore, the window for electron-beam annealing is wider and flatter than that observed for laser annealing, as shown in The plot of I_{photo} versus laser power for the laser annealed (LA) sample at 250°C is identical to that shown in Fig. 3.4. However, for comparison with the scanning-electron-beam annealing (SEBA) done at room temperature, the LA curve obtained with a substrate temperature of 25°C, also shown, is more appropriate. Two major differences between the LA and SEBA cases are immediately apparent. First, the electron-beam annealing produces a wide, flat window, compared to the laser-anneal curve, which peaks sharply at a power determined by the substrate temperature. Secondly, when the electron-beam curve falls off, it does so precipitously; that is, the sample goes from good quality material to a state of high slip-plane density for a very small increase in It is difficult to observe an intermediate region, beam power. where damage is introduced by the laser without the formation of dislocations, in the case of the electron beam. These slip dislocation networks are shown in Fig. 3.10. Networks are formed for both LA and SEBA, with only slight differences in appearance, which may be due to the different power level involved in annealing. It

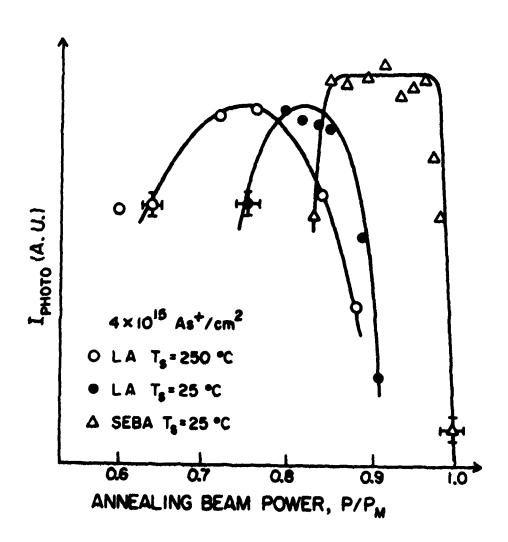
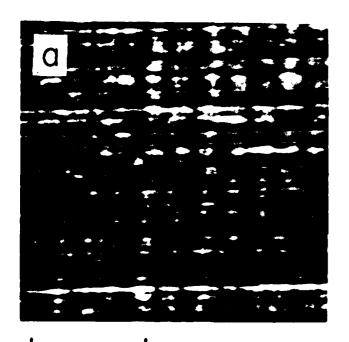
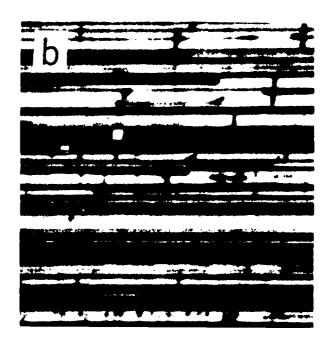


Fig. 3.9 Dependence of short-circuit current, I_{photo} , in relative units, on annealing laser power for samples laser-annealed (LA) at two different substrate temperatures, and for samples electron-beam annealed (SEBA) at room temperature. Beam power is normalized by the melting power, $P_{\rm M}$.





100 μm

Fig. 3.10 EBIC micrographs showing the introduction of slip dislocations for (a) laser annealing and (b) electron-beam annealing.

should be noted that the SEBA data shown in Fig. 3.9 are in good quantitative agreement with independent measurements done elsewhere (25).

Figure 3.11 is a quantitative EBIC comparison of laser annealing and electron-beam annealing results. The EBIC collection efficiency of SEBA is higher than that of the optimal LA sample at low EBIC accelerating voltage. At high accelerating voltage, the EBIC collection efficiency is comparable for SEBA and optimal LA. This suggests that the sample quality near the surface is better after SEBA than after optimal LA. However, as shown in Fig. 3.11, falls off at high accelerating voltage for the high-power LA sample, but it is comparable to SEBA at low EBIC accelerating voltage. There seems, therefore, to be a compromise between good surface recrystallization and laser-induced damage for optimal LA power. This problem has not been observed for SEBA; i.e., the SEBA results represent the "envelope" of the best results obtained by laser annealing. The reasons for these differences are presently unclear, but will be discussed further at the end of this chapter and in Chapter 6.

3.6 <u>Determination of Minority-Carrier Diffusion Length by EBIC</u>

The complexity of the phenomena associated with interactions of electron with solids, and factors such as the excitation geometry, carrier diffusion, carrier recombination, surface recombination and barrier geometry involved in the current measurement, make the quantitative interpretation of EBIC measurements difficult.

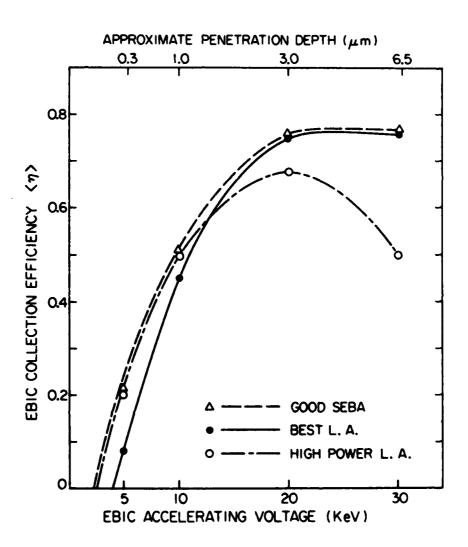


Fig. 3.11 Comparison of EBIC collection efficiency $\langle \eta \rangle$ as a function of accelerating voltage for SEBA, optimal LA $(P/P_M=0.75)$ and high power LA $(P/P_M=0.9)$.

Previous EBIC investigations (3,9) of minority-carrier diffusion lengths in semiconductors have used angle-lapped diodes. Simplified models have been developed to analyze EBIC in this case. Thus, the exponential decrease of induced current with increasing distance between the excitation point source and the collection junction is used in semiconductors to determine the minority-carrier diffusion length in fairly uniform crystals. However, this technique has the undesirable effect of complicating the measurement because of special sample preparation and, in addition, is not applicable to spatially varying recombination.

In this section, an attempt is made to derive the approximate minority-carrier diffusion length from the EBIC collection efficiency $\langle \eta \rangle$, with the electron beam penetrating perpendicularly to the n^+ -p junction (i.e., the configuration used in this work, cf. Fig. 3.1). Under steady-state generation and low-level injection conditions, the minority-carrier transport can be expressed by the steady-state continuity equation

$$D_n \nabla^2 \Delta n - \frac{\Delta n}{\tau_n} = g \qquad , \tag{3.6}$$

where D_n is the diffusion constant for excess minority carriers, Δn is their density, and τ_n is their lifetime; g is the point generation rate due to the electron-beam interaction with the material. Two assumptions have been made in Eq. (3.6) for simplicity: (i) the junction is very shallow, so that the effect of the n^+ layer

can be neglected. (ii) surface recombination is also neglected. Both assumptions are more appropriate for high accelerating voltage. The following boundary conditions are assumed: $\Delta n=0$ at z=0 (i.e., the depletion region is at the surface) and at $z=\infty$. The induced current I_{EBIC} as derived from the solution of Δn in Eq. (3.6) is $^{(10)}$

$$I_{EBIC} = I_B \int_0^\infty \frac{1}{g} \frac{dE}{dz} \exp(-\frac{z}{L_e}) dz , \qquad (3.7)$$

where dE/dz is the depth-dose function, i.e., the energy loss of the electrons per unit depth. The other symbols are the same as defined before (cf. Eq. 3.1). The penetration range, R_g , for silicon, is commonly taken as $^{(3)}$

$$R_g(\mu m) = 0.0171 E_B^{1.75}(keV)$$
 (3.8)

The depth-dose function can be represented by the polynomial (3)

$$\frac{dE}{dz} = \begin{cases} \frac{(1-f)E_B}{R_g} \left[0.60+6.21(\frac{z}{R_g})-12.40(\frac{z}{R_g})^2+5.69(\frac{z}{R_g})^3\right] & \text{for } z \leq 1.1 R_g \\ 0 & \text{for } z > 1.1 R_g \end{cases}, \tag{3.9}$$

where f is the fraction of backscattered electrons. For silicon, f = 0.08. (3) From Eqs. (3.1), (3.7) and (3.9), the EBIC collection efficiency < η > can be expressed as

$$\langle \eta \rangle = \frac{GI_{EBIC}}{E_{B}I_{B}} = (1 - f) \int_{0}^{1.1} [0.60 + 6.212 - 12.402^{2} + 5.692^{3}]$$

$$\exp(-Z/L)dZ = (1 - f)\{[0.00039L + 0.04153L^{2} - 12.754L^{3} - 34.14L^{4}]\}$$

$$\exp(-1.1/L) + 0.60L + 6.21L^{2} - 24.8L^{3} + 34.14L^{4}\} , \qquad (3.10)$$

where $Z = z/R_{cl}$ and $L = L_{el}/R_{cl}$. From the above result, the EBIC collection efficiency as a function of the incident electron-beam energy for various diffusion lengths is plotted in Fig. 3.12. For low accelerating voltages, the collection efficiency is large, approaching 1 - f = 0.92; this is obviously different from the experimental results shown in Fig. 3.11. This deviation is due to surface recombination effects which are not considered in the above derivation. Therefore, the results in Fig. 3.11 are good only for high accelerating voltage, in accordance with the assumptions made before. Because the maximum available voltage of the SEM is 30 kV, the EBIC collection efficiency is plotted as a function of the diffusion length for this accelerating voltage in Fig. 3.13. It can be seen that, for $L_a > 20 \mu m$, the collection efficiency becomes less sensitive to the variation of the diffusion length. Therefore, a 5% experimental error in measuring <n> might lead to an error by a factor of more than 2 in determining the diffusion length from Fig. 3.13. This is the major difficulty in accurately determining the minority-carrier diffusion length in optimally beam-annealed samples, for which <n> is about 0.8, as shown in Fig. Nevertheless, by comparing the data for 30 kV in Fig. 3.5

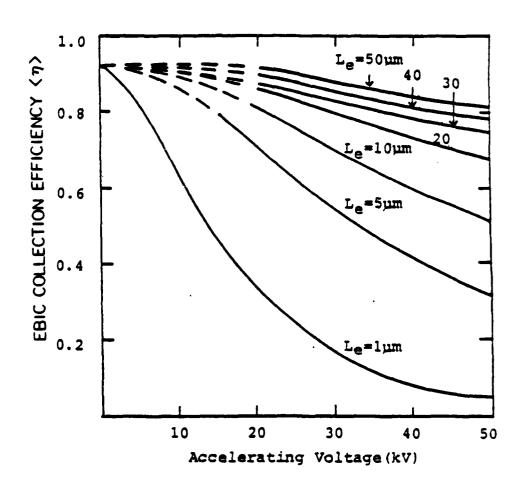


Fig. 3.12 EBIC collection efficiency $\langle \eta \rangle$ as a function of accelerating voltage for different diffusion lengths, calculated from the theory (Eq. 3.10).

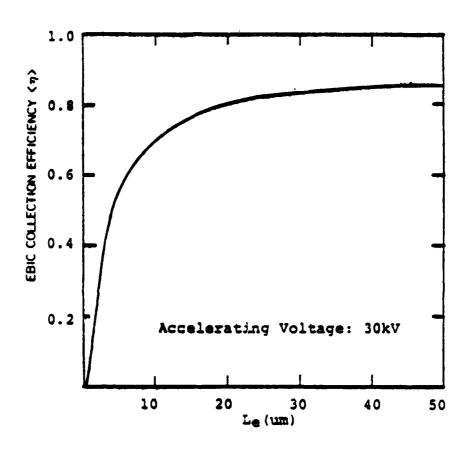


Fig. 3.13 EBIC collection efficiency as a function of diffusion length for 30 keV electron beam as calculated from Eq. 3.10.

with the calculations shown in Fig. 3.13, it can be concluded that high laser power degrades the diffusion length from $L_e > 15~\mu m$ to $L_e \sim 5~\mu m$. It is, therefore, obvious that the minority-carrier lifetime in the substrate near the junction is greatly reduced by high laser power.

3.7 Relation of Laser-Induced Damage with Original Crystal Quality

In order to learn more about the nature of the laser-induced damage which appears as dark stripes in slip-free samples, two sets of ion-implanted Si samples were pre-annealed either by SEBA or by conventional thermal annealing (pre-TA); these samples were then laser annealed. Figure 3.14 shows that the short-circuit photocurrent collection efficiency of electron-beam pre-annealed samples is not degraded by LA until the laser power is high enough to produce slip dislocations. No dark lines in the EBIC display were observed in this set of samples. Pre-TA samples on the other hand, show quite different results, also shown in Fig. 3.14; thermallyannealed samples show considerably poorer collection efficiency. In general, samples subjected only to thermal annealing usually contain residual lattice structure defects, and the implanted impurity is often redistributed during the thermal process. Moreover, the annealing facility and process used in the investigation at UCSB are not state-of-the-art. It is believed that all these effects contribute to the low apparent collection efficiency of TA samples relative to optimal LA and SEBA samples. After laser

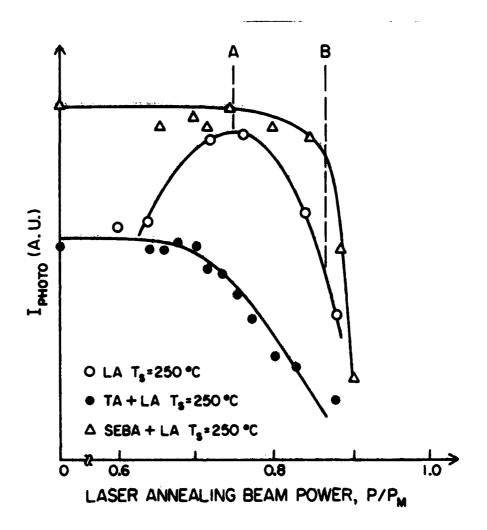


Fig. 3.14 Dependence of short-circuit photo-current on annealing laser power for samples subjected to laser-annealing (LA) only, and for samples pre-annealed prior to LA, either by thermal annealing (TA) or optimal SEBA. All the samples were implanted with ${\sf As}^+$ at 100 keV to a dose of $4\times10^{15}/{\sf cm}^2$.

annealing these pre-TA samples, the collection efficiency starts to degrade at 70% of melting power, which is below the optimal LA power. Defects after TA alone were observed as dark ${\sf spots}^{(11)}$ in the EBIC display at 5 kV accelerating voltage in our samples. After laser annealing with power higher than 0.70 $\mathbf{P}_{\mathbf{M}},$ not only can laser-induced stripe damage be observed, but the original dark spots also grow deeper, because they can be observed at higher EBIC accelerating voltage. Comparing the results of the two pre-anneal experiments shown in Fig. 3.14, it seems that the extent of laser induced damage depends on the original crystal quality of the Once good-quality single-crystal material has been recrystallized (as, for example, by SEBA), the laser scan itself will not produce stripe-like damage. However, since the crystal quality is only partially recovered by $TA^{(12)}$, further laser scanning induces more defects in the sample. Furthermore, if samples are thermally annealed after damage-stripes are induced by laser annealing, the laser-induced stripe damage cannot be eliminated by post-TA at 900°C.

In order to prove further that this laser-induced damage is related to the original condition of the sample, shallow implants were investigated. For the case of ${\rm As}^+$ implants at 40 keV, laser-induced damage does not appear to be as deep as in the case of 100 keV implants. Figure 3.15 shows the EBIC display for both 40 keV and 100 keV ${\rm As}^+$ implanted samples, laser annealed using the same laser power (0.85 ${\rm P}_{\rm M}$). For the shallow implant shown in Fig. 3.15(a), dark stripes in the EBIC display can be observed only at

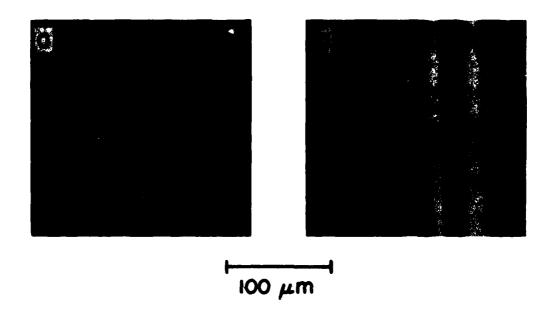


Fig. 3.15 EBIC micrograph for (a) 40 keV, 5×10^{14} cm⁻², (b) 100 keV, 4×10^{15} cm⁻² As⁺-implanted Si, annealed with laser power P=0.85 P_{M} . Electron-beam accelerating voltage for (a) is 2.5 kV and (b) is 30 kV.

low accelerating voltage (2.5 kV and 5 kV); the display appears featureless when the accelerating voltage is higher than 10 kV. On the other hand, for the 100 keV implantation case, even at 30 kV accelerating voltage, the laser-induced dark stripes still have strong contrast. Note that the penetration depth of a 2.5 keV electron beam in Si is \sim 0.1 μ m, while 30 keV electrons can penetrate approximately 6 μ m; the relative defect depth distribution in these two samples is therefore obviously different, as is the implant depth. This laser-induced dark-stripe damage also depends on the implanted dose. For a 100 keV implant, the minimum dose required to observe these dark stripes was 1×10^{15} cm⁻² for B⁺, 5×10^{13} cm⁻² for P⁺, and 5×10^{12} cm⁻² for As⁺. Thus, lower dose is required for heavier ion mass.

3.8 The Nature of Laser-Induced Damage

Lattice defects in CW laser-annealed Si have been studied by several research groups using TEM. In an earlier study, Gat et al. (13) reported the realization of an almost defect-free recrystallized layer. This encouraging result differed, however, with later results of Rozgonyi et al. (14) who observed a high density of small dislocation loops. Because of this discrepancy, Ishida et al. (15) studied in detail the dependence of lattice defects in the CW laser-annealed layer on laser power and implanted As⁺ dose. At low laser power, clusters of small point defects were observed. With increasing laser power, these point defect clusters developed

into a high density of interstitial type dislocation loops. The density of the dislocation loops increased with implantation dose. At still higher laser power, the generation of slip dislocation results in observable slip lines in the <110> direction on the sample surface. The electronic activity of these lattice defects cannot be determined by TEM.

Since the discovery of laser-induced defects by measurements as described in this chapter was first reported, their nature, nucleation, formation mechanism and ultimate suppressions have become topics of interest from both fundamental and applied points of view. Combining x-ray topography and high voltage TEM, Rozgonyi and Baumgart et al. (16-21) have studied a single CW laser recrystallized spot with and without slip formation. For the slip-free case, strain contrast is revealed by x-ray topographs at the boundary between the single crystal spots and the surrounding amorphous field. A similar level of strain contrast has also been observed at the border of the ion-implanted amorphous and nonimplanted single crystal (17). When ion implantation produces an amorphous layer near the surface of crystalline Si, expansion in volume is known to accompany such a crystalline-to-amorphous transformation. The increased volume of the implanted layer is detectable directly by upheavals on the surface and, on the other hand, by the strain which affects the surrounding more perfect regions of the crystal (observable using x-ray topography (22)). The strain surrounding the individual laser-recrystallized spots is

caused by tensile stress because the expanded volume of the amorphous layer contracts during the laser-assisted epitaxial recrystallization. Inside the slip-free spot, the recrystallization of the damaged layer is perfect; no residual defects were observed in x-ray topograph. A model of the dislocation generation alide and processes, which accompany this $proposed^{(17-19)}$ as a result of the high-voltage TEM analysis of laser-recrystallized spots with slip dislocations; the model is shown in Fig. 3.16. Small dislocation half-loops nucleate at the surface in the central region of an annealed spot and glide under the action of the dilational strain imposed by the temperature gradients in both the lateral and normal directions; (cf. Fig. 3.16). In both slipped and nonslipped laser annealed spots, submicron dislocation loops (the small circles in Fig. 3.16) were found along the recrystallized perimeter, but not in virgin wafers irradiated by the laser. Dislocation loops can be formed by the clustering of point defects, and are commonly referred to as interstitial- or vacancy-type depending on the nature of the clustered species. Those submicron dislocation loops found in CW laserannealed samples have been shown to be interstitial character(18-21). This is consistent with a mechanism of formation by agglomeration of interstitial atoms during the rapid cooling associated with laser annealing. The absence of these submicron dislocation loops in the spot center is attributed to an annihilation by $climb^{(23)}$ in the inner, higher-temperature region.

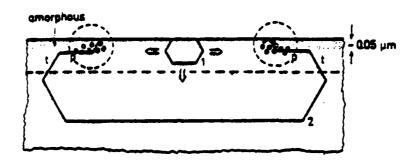


Fig. 3.16 Schematic representation of dislocation nucleation and subsequent glide in laser-annealed silicon. The initial stage is indicated in position (1) and position (2) shows the final stage of an expanding dislocation half-loop. p:-dislocation segment parallel to the surface, t:-threading dislocation (after Ref. 19).

Although isolated CW Ar $^+$ annealed spots only show strain contrast at the amorphous to single-crystal border, the strain is still present if a large single-crystal area is obtained by substrate scanning. It has been shown that the same dark-stripe features found in the x-ray topographs of CW laser-scanned, slip-free samples, with a one to one correspondence between the dark stripes in the EBIC image and the x-ray topograph. (19-21) A high density of submicron dislocation loops due to interstitial atoms has been observed by TEM in the dark-stripe region. (20,21) It is therefore concluded that these interstitial submicron dislocation loops are electronically active and that they are responsible for the EBIC contrast of the laser-induced defects.

A model is proposed here which fits most of the experimental observations. As shown in Fig. 3.17, the first scan creates a tapered amorphous/single-crystal interface, I_1 , because of the slower solid-phase epitaxial rate at the flank of the laser beam (where the laser power is reduced), than at the center. The existence of this wedge-shaped boundary has been demonstrated because its refractive index is different from both amorphous and single-crystal $\mathrm{Si}^{(14)}$. Although the solid-phase epitaxy starts from the amorphous-to-single-crystal interface, I_0 , the temperature in the partially annealed region above I_1 , is higher than that in the recrystallized region right below I_1 . The effect of the lateral temperature gradient on the residual implant damage is as follows: a high density of small dislocation loops is formed in

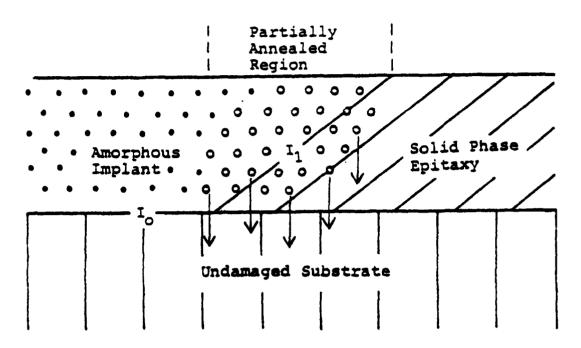


Fig. 3.17 Schematic representation of dislocation loop nucleation and subsequent climb in laser-annealed Si. Laser scanning direction is prependicular to the page. Dislocation loops (o) were created in a tapered partially annealed region along the edge of the laser beam. Successive overlapped scan induces a negative climb of dislocation loops as shown by the arrows. The depth of this climb depends on the laser power.

the partially annealed region by creating an excess number of interstitial atoms which are quenched in place during the rapid cooling process. The next successive overlapping scan completes the recrystallization in the partially annealed region; however, the interstitial atoms diffuse into the substrate, inducing negative climb (23) of dislocation loops. The depth of this process increases with laser power. Therefore, once the loop nucleates, it cannot be eliminated by a second, overlapping scan. This model can explain the dependence of laser-induced defects on laser power (Fig. 3.3), the absence of dislocaton loops in virgin Si irradiated by a laser $^{(18,19)}$ and the dependence of laser-induced-defect depth on the implant depth, as observed in Fig. 3.15. For 30 keV electron-beam annealing, on the other hand, the electrons penetrate deeply into the substrate. This not only reduces the temperature gradient, but reverses its direction; that is, the temperature in the partially annealed region above I_{1} is lower than the recrystallized region right below \mathbf{I}_1 . Both of these effects might reduce the quenched-in interstitial atoms and nucleation of dislocation loops in the partially annealed region. It is interesting to note that the best annealing results achieved to date for the compound semiconductors GaAs and InP were obtained with the use of a randomly scanned electron beam(24) instead of using an Ar $^+$ laser.

References:

- 1. A. Gat and J.F. Gibbons, Appl. Phys. Lett. <u>32</u>, 142 (1978).
- 2. L.J. van der Pauw, Philips Res. Repts. 13, 1 (1958).
- 3. T.E. Everhart and P.H. Hoff, J. Appl. Phys. 42, 5837 (1971).
- 4. L.C. Kimerling, H.J. Leamy, J.L. Benton, S.D. Ferris, P.E. Freeland and J.J. Rubin, in <u>Semiconductor Silicon/1977</u>, (Electrochemical Society, Princeton, 1977), p. 468.
- 5. S.M. Sze, <u>Physics of Semiconductor Devices</u>, (Wiley, New York, 1969), p. 661.
- 6. ibid, p. 647.
- 7. C. Donolato, Appl. Phys. Lett. <u>34</u>, 80 (1979).
- 8. Y.I. Nissim, A. Lietoila, R.B. Gold, and J.F. Gibbons, J. Appl. Phys. <u>51</u>, 274 (1980).
- 9. K. Karaya and S. Okayama, J. Phys. D5, 43 (1971).
- 10. J.Y. Chi and H.C. Gatos, J. Appl. Phys. 50, 3433 (1979).
- D.E. Ioannou and S.M. Davidson, Phys. Stat. Sol. (a) 48, K1 (1978).
- 12. H. Nakashima, Y. Shiraki, and M. Miyao, J. Appl. Phys. <u>50</u>, 5966 (1979).
- A. Gat, J.F. Gibbons, T.J. Magee, J. Peng. V.R. Deline, P. Williams, and C.A. Evans, Jr., Appl. Phys. Lett. <u>32</u>, 276 (1978) and Appl. Phys. Lett. <u>33</u>, 389 (1978).
- 14. G.A. Rozgonyi, H.T. Leamy, T.T. Sheng and G.K. Celler, <u>Laser-Solid Interactions and Laser-Processing 1978</u>, edited by S.D. Ferris, H.J. Leamy, and J.M. Poate (AIP, New York, 1979), p. 457.

- K. Ishida, H. Okabayashi, and M. Yoshida, Appl. Phys. Lett.
 37, 175 (1980).
- G.A. Rozgonyi and H. Baumgart, J. de Physique, <u>41</u>, Suppl. 5,
 p. C4-85 (1980).
- H. Baumgart, G.A. Rozgonyi, and R. Uebbing, J. Phys. Soc.
 Japan 49 (1980), Suppl. A. p. 1291-1294.
- H. Baumgart, F. Phillipp, G.A. Rozgonyi, and U. Gosele, Appl. Phys. Lett. 38, 95 (1981).
- 19. G.A. Rozgonyi, H. Baumgart, and F. Phillip, <u>Laser and Electron-Beam Solid Interactions and Material Processing</u>, edited by J.F. Gibbons, L.D. Hess, and T.W. Sigmon (North Holland, 1981), p. 155.
- 20. H. Baumgart, O. Hildebrand, F. Phillip, and G.A. Rozgonyi, Proceedings of 2nd Oxford Conference on Microscopy of Semiconducting Materials, Oxford, April 6-10, 1981 (Institute of Physics, London).
- 21. H. Baumgart, F. Phillipp and H.J. Leamy, to be published in Laser and Electron Beam Interactions with Solids, edited by B.R. Appleton and G.K. Celler (North Holland, 1982).
- K.N. Tu, P. Chaudhari, K. Lad, B.L. Crowder, and S.I. Tan, J. Appl. Phys. 43, 4262 (1972).
- D. Hull, <u>Introduction to Dislocations</u>, (Pergamon Press, 1975),
 2nd edn. p. 72.

- 24. N.J. Shah, R.A. McMahon, A.G. Cullis, and H. Ahmed, <u>Laser and Electron-Beam Solid Interactions and Materials Processing</u>, edited by J.F. Gibbons, L.D. Hess, and T.W. Sigmon (North Holland 1981), p. 201.
- 25. N.M. Johnson, private communication.

In this chapter, low-temperature photoluminescence has been used to investigate minority-carrier recombination processes in implanted and laser-annealed Si. The range of laser power over which good quality annealed material can be achieved, as determined by the relative luminescence efficiency of excitons bound to implanted donors and conventionally doped acceptors after laser annealing, is limited. These results are consistent with those of EBIC; both indicate that the laser-induced damage is produced deeper in the substrate than the implanted layers. At high laser power, when laser-induced damage has been observed by EBIC as discussed in the previous chapter, a slight broadening and shifting of the bound-exciton luminescence lines was observed. Attempts to measure the defect luminescence directly were not successful.

4.1 <u>Luminescence and Exciton States</u>

The control and analysis of impurity- and defect-dominated extrinsic effects are most conveniently achieved by luminescence techniques. Electron-hole pairs are generated by light, electron bombardment or by injection. The recombination of the excess carriers can be radiative and can also emit phonons. The intensity of the luminescence depends on the radiative quantum efficiency, and the luminescence spectrum gives the detailed information about the levels involved. This technique is non-destructive in prin-

ciple, and can be performed with high resolution, both in photon energy and in spatial position on the sample. These features are significant because electrical analysis requires contacts and sufficient space for handling; thus electrical measurements often lack spatial resolution.

For a variety of semiconductors, bound-exciton luminescence studies have often helped considerably in the identification of impurities. An exciton can be postulated as a composite particle consisting of an electron and a hole, both of which are mutually attracted according to the screened electron-hole Coulomb interaction. As shown in Fig. 4.1(a) the recombination of a free exciton emits light with energy

$$hv = E_G - E_x ,$$

where E_G is the energy gap and E_χ is the binding energy of an exciton. When dopant atoms are added to silicon, the impurity serves as a recombination center, capturing excitons and subsequently allowing these bound excitons to recombine, with or without phonon asssistance. For zero-phonon peaks, the energy of the bound-exciton recombination luminescence is given by

$$hv = E_G - E_x - E_{bx} = E_G - E_{BX}$$

where E_{bx} is the exciton binding energy at an impurity center. As shown in Fig. 4.1(b), E_{BX} is defined as: $E_{BX} \equiv E_x + E_{bx}$. The value of E_{bx} depends on the impurity species, and corresponds to

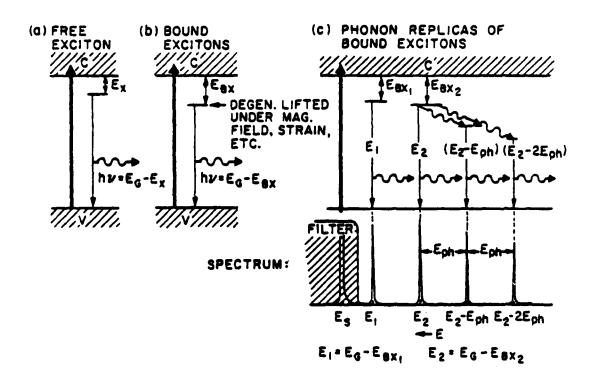


Fig. 4.1 A schematic representation of (a) free- (b) bound-exciton states and (c) phonon replicas of bound excitons.

different transition energies in the photoluminescence spectrum of the bound exciton. This enables us to identify the specific impurities involved for the purposes of material characterization. The energy of the luminescence transition due to phonon replica of the bound exciton, as shown in Fig. 4.1(c), is

$$hv = E_G - E_{BX} - E_{ph}$$

where $E_{\rm ph}$ is the phonon energy, which can be determined from the phonon dispersion curves of the semiconductor of interest. For Si. the existence of excitons bound to various group-III and group-V impurities was studied in detail in the 1960's. (1-3) Impurities can also bind more than one exciton to form bound multiexciton $complexes^{(4,5)}$ which can be observed as a series of satellite lines with energies a few meV below the bound exciton line as the excitation intensity increases. At more intense excitation levels, the electron and hole in an exciton give up their exclusive association and enter a "sea" of particles in which they are bound equally to all the other charge carriers in the droplet, and the satellite line series grows into a broad luminescence band due to the formation of electron-hole droplets. (6) Electron-hole pairs also can recombine at defect centers which can be either radiative or non-radiative; if non-radiative, the bound-exciton photoluminescence intensity is reduced. The binding of various exciton complexes has been reviewed by Hopfield. (21)

4.2 Experimental System

A schematic diagram of the photoluminescence system is shown in Fig. 4.2. Low-temperature photoluminescence measurements were carried out with the samples mounted in a liquid-He immersion dewar. Temperatures as low as 1.6 K could be achieved by pumping the He below the lambda point. Luminescence was excited by low power output (typically < 300 mW) from the same Ar ion laser used for annealing experiments. The excitation wavelength was 5145 A, corresponding to a 1/e penetration of the exciting light of approximately 2-3 µm. A 1-meter McPherson monochromator with a dispersion of 16 A/mm, and an S-1 response photomultiplier (ITT-FW118) cooled to -100°C, with either phase-sensitive (PAR model 124 lock-in amplifier with PAR 184 current sensitive preamplifier) or photon-counting (PAR quantum photometer model 1140A) techniques, were used to detect the luminescence. The resulting resolution was sufficient to detect individual bound-exciton lines and determine broadening and shifts of these lines induced by stress. slit width is shown in each figure of the data. A photoconductive PbS detector cooled by dry ice, with phase-sensitive (PAR model 124 lock-in amplifier with PAR model 116 differential preamplifier), was used to measure long-wavelength (> $1.1 \mu m$) defect luminescence.

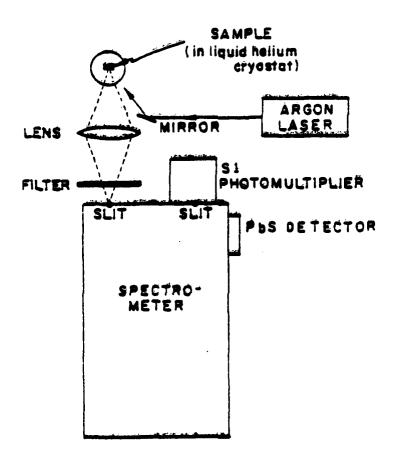


Fig. 4.2 A schematic diagram of photoluminescence system.

4.3 Photoluminescence Evaluation of Laser-Annealed Si

Low-temperature, bound-exciton luminescence of donors and acceptors in Si has been studied in detail. (1-12) However, there are two additional complications involved in the investigation of luminescence from ion-implanted materials: (1) the luminescence intensities are generally quite weak, because of the presence of unannealed strain and damage in the vicinity of the implanted ion, and (2) the penetration of the implanted ions is quite low, typically only a few tenths of a µm, so that efficient overlap of the impurity distribution and the exciting light is difficult. first of these difficulties is, of course, the point of using low-temperature luminescence to investigate the quality of beamannealed material. For the second difficulty, a multiple-energy implantation of P^{++} was performed with a maximum energy of 180 keV to create a deep and uniform P concentration profile, so that enhanced luminescence intensity could be obtained. Typically, a flat profile of P with a concentration of 10^{16}cm^{-3} to a depth of ~0.6 µm was used; under these conditions, the surface did not become amorphous. This concentration was chosen to prevent concentration quenching of the luminescence (9). Since the penetration of the Ar^+ laser excitation into the sample was ~2-3 μm , which is deeper than the implanted layer thickness of ~0.6 µm, some of the luminescence observed was from the B doping of the p-type substrate. This luminescence was used to evaluate any deterioration or creation of damage in the substrate as a result of the implant or the beam processing. Phosphorus-related luminescence is expected only from the implanted layer, since there was no additional P doping other than the implant. Some thermally annealed samples (1000° C, 30 min., N_2) were used for comparison.

A typical luminescence spectrum obtained for a P-implanted and thermally-annealed sample is shown in Fig. 4.3. The higher energy region of the spectrum shows the recombination of excitons bound to neutral B and P; these are no-phonon lines, and are designated B_{NP} and P_{NP} . (2,3) Additional weak lines, denoted $B_{NP}(b_i)$, etc., result from bound multiexciton complexes. (4,5,11,12) In the lower energy region, the emission lines consist of momentum-conserving phonon replicas of the no-phonon lines; these are denoted by B_{LO} , B_{TO} , etc., to indicate the type of phonon involved. Note that in this and the following figures, the intensities of the no-phonon lines and the TO phonon lines are independently normalized for clarity of presentation. The actual intensity ratios B_{NP} to B_{TO} and P_{NP} to P_{TO} are typically ~0.05 and ~1.4 respectively.

Very similar spectra were obtained from laser-annealed samples with annealing laser power ranging from 0.6 to 0.95 of the melting power (P_M) for Si. Figure 4.4 shows the results for P: the luminescence intensity for the P_{NP} emission line is plotted as a function of the annealing power, relative to the melting power, P_M . No luminescence signal is observed below 0.6 P_M , indicating that this laser power was insufficient for activation of the implanted

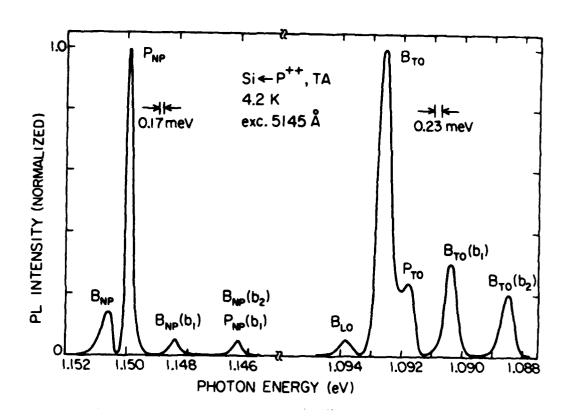


Fig. 4.3 Low temperature photoluminescence spectrum for P^{++} implants into B-doped Si, followed by conventional thermal anneal. The implant conditions and the resulting spectral features are explained in the text.

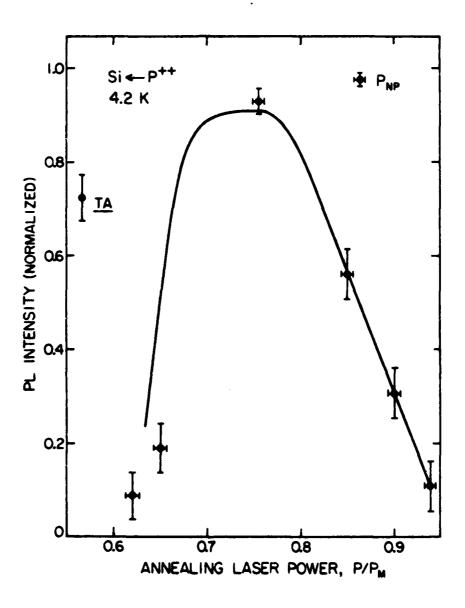
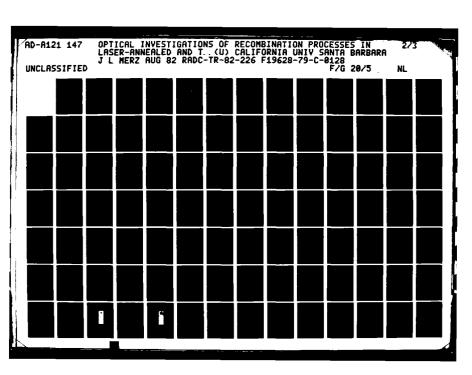
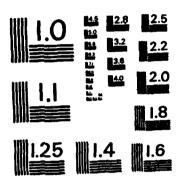


Fig. 4.4 Low temperature photoluminescence intensity, in normalized units, as a function of annealing laser power for Phosphorus no-phonon line (P_{NP}) . The intensity of these luminescence lines for thermally-annealed material is indicated by TA. Implant conditions are the same as Fig. 4.3. $T_S = 250^{\circ}\text{C}$.





MICROCOPY RESOLUTION TEST CHART NATIONAL BUREAU OF STANDAROS-1963-A

However, a sharp increase is observed between 0.6 and 0.7 $P_{\rm M}$, which clearly shows activation of the implanted species. result is fully consistent with the electrical activation results obtained by sheet resistivity measurements (cf. Fig. 3.4), for which 4×10^{15} As⁺ ions/cm² were implanted into the same substrate material and laser annealed. The luminescence results, on the other hand, were obtained for low-dose P++ implants below the dose necessary to make the Si amorphous. The similarity of these results suggests that the implant dose does not have a strong influence on the laser power required for the activation of implanted impurities. After reaching a maximum intensity, the luminescence decreases with increasing laser power despite the fact that there is no change in the degree of electrical activation (as shown by the sheet resistivity data of Fig. 3.4). This decrease in intensity must therefore result from a deterioration of the minority carrier lifetime and/or creation of non-radiative defects. An alternate explanation, involving small displacements of the P atom from its substitutional lattice site (for which electrical measurements are far less sensitive than optical measurements), is considered unlikely on the basis of the very small lattice displacements estimated from the optical data to be described below.

For the case of B luminescence, a similar dependence on laser power was observed, as shown in Fig. 4.5. However, the reason for this power dependence must be somewhat different than that for the P case, since this luminescence originates from B acceptors in the

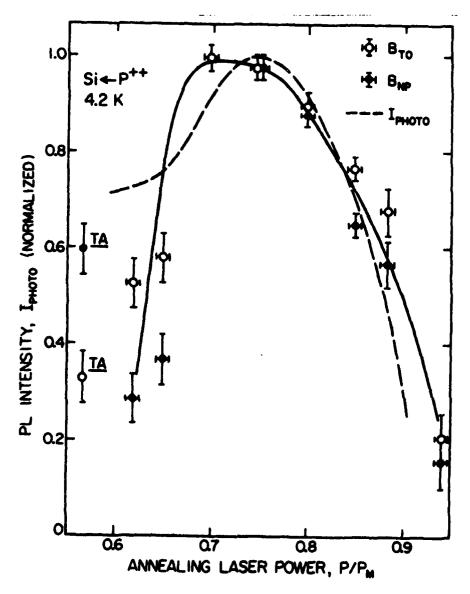


Fig. 4.5 Low temperature photoluminescence intensity, in normalized units, as a function of annealing laser power, for Boron no-phonon line (B_{NP}) and TO-phonon line (B_{TO}). The intensity of these luminescence lines for thermally-annealed material is indicated by TA. The broken line is the dependence of I_{photo} for a heavier dose implant, taken from Fig. 3.4. Implant conditions are the same as Fig. 4.3. $I_{S} = 250^{\circ}\text{C}$.

original substrate material. The exciting light penetrates deeper than the implanted layer, exciting luminescence from the substrate boron. Thus, even for laser power less than 0.6 $P_{\rm M}$ (for which no P luminescence was observed), the B luminescence intensity was already ~30-40% of its maximum value. For increasing laser power, the B luminescence intensity also increases, as a result of at least two effects: (1) B in the implanted layers also becomes optically active as a result of the laser annealing, and (2) the absorption coefficient of the implanted layer is reduced, so that more substrate B can be excited. Finally, the reduction in luminescence intensity above 0.75 $P_{\rm M}$ can be attributed to the production of defects at high laser power, as was the case for the Pluminescence. However, there is again the difference that most of the optically active B is expected to be in the substrate below the implanted layer, suggesting that the laser-induced defects also extend quite deep into the substrate. This is consistent with the short-circuit photocurrent, I_{photo} , obtained for a higher dose implant, and also plotted in Fig. 4.5.

The strain which exists after laser annealing can also be estimated from the detailed line shape of the no-phonon lines. For this purpose, a high-resolution spectrum in the region of the no-phonon lines is shown in Fig. 4.6. For a sample doped with P during growth, the half-width measured for the $P_{\rm NP}$ lines is very small, and is instrument-limited in Fig. 4.6. However, for P-implanted samples, both a conventional thermal anneal (TA) and a

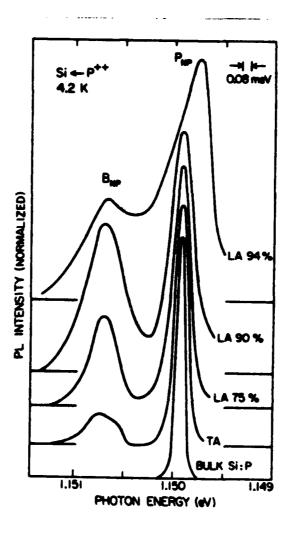


Fig. 4.6 High resolution spectra of B and P no-phonon luminescence lines for bulk Si conventionally doped with P, and for P^{++} implanted samples that have been thermally annealed (TA) or laser annealed (LA) at the laser power (normalized to the melting power) indicated. Implant conditions are the same as Fig. 4.3. $T_S = 250^{\circ}\text{C}$.

laser anneal show increased half-widths, indicating that the implant damage has not been completely removed. As the laser power increases, the linewidth also increases until, at ~0.94 P_M , the peak of the line begins to shift to lower energy. This laser power is sufficient to induce damage; consequently a strain field exists at the impurity. By comparing this data with published uniaxial stress data for P-doped Si, $^{(10,11)}$ an estimate can be made of the strain-induced lattice displacement, $\Delta a/a$. The maximum displacement observed in these experiments, at a laser power corresponding to 0.94 P_M , was only $\Delta a/a = 10^{-4}$, a surprisingly small amount. For this value of laser power, slip dislocations form, as was seen in Figs. 3.4 and 3.10. Thus, the strain field is relaxed by the introduction of these dislocations. At lower laser power, where no slip was observed, the lattice displacement is clearly seen to be very small.

4.4 Defect Luminescence in CW Laser-Annealed Si

While bound-exciton luminescence of Si has been investigated in detail during the last two decades, there is relatively little information and understanding about defect luminescence in Si. This slow progress is partly due to the weak Si defect luminescence which is in an unfavorable spectral range for available detectors, and partly due to the fact that the resulting deep levels are generally non-radiative. Several sharp peaks have been reported for electron irradiated (13,14) and ion implanted (11,16) Si; however, their microscopic origins are still uncertain.

The defect luminescence of solid-phase CW laser-annealed Si has also been reported; (17,18) this spectrum bears no resemblance to those observed in electron- and ion-bombarded Si, $^{(13-16)}$ suggesting that a different set of defects is present. The spectrum and intensity of CW laser-annealed Si depend on both substrate temperature (T_S) during annealing and beam-overlap, but not on substrate dopants. Figure 4.7 shows a typical defect luminescence spectrum (from Ref. 18) for Czochralski-grown p-type Si implanted with SiH^{+} at 80 keV to a dose of 2 \times 10 15 cm⁻² and annealed by a CW Ar laser. It consists of a multitude of broad bands the properties of which can be summarized as follows. (1) Substrate temperature effects: For $T_c = 350$ °C, the spectrum is dominated by a peak at 912 meV, as shown in Fig. 4.7(a). However, for $T_S = 50^{\circ}\text{C}$, the defect luminescence has an entirely different spectrum, and, although not plotted in Fig. 4.7, is much weaker. For the sample laser-annealed at $T_s = 50^{\circ}\text{C}$, post-thermal annealing at 350°C increases the intensity by an order of magnitude, with 935 meV as the dominant peak (Fig. 4.7(b)). This result suggests that the substrate temperature during laser annealing is an important para-(2) Overlapping effects: The sample of Fig. 4.7(a) was annealed with a 40 μm beam spot and a 15 μm step size, which gives ~60% overlap. Discernible lateral nonuniformity consisting of amorphous or poly stripes between the laser scans can be observed by an optical microscope. By increasing the beam spot to 80 μm with a 15 μ m step size (overlap ~80%), the defect luminescence is

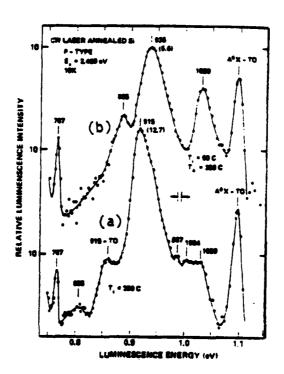


Fig. 4.7 Luminescence spectra of CW laser-annealed p-type Si, showing the effects of substrate temperature and thermal annealing. Peak positions are given in meV. The numbers in brackets give relative luminescence intensities (after Ref. 18).

reduced by a factor of 30. Therefore, it was concluded that this defect luminescence was associated with an imperfect interface between adjacent laser-annealed zones.

The defect spectra shown in Fig. 4.7 were obtained in another laboratory. (18) In order to study this defect luminescence in more detail, we have tried to repeat these experiments. We used the same implant conditions, except that Si⁺ was implanted instead of SiH^T. The samples were annealed using our typical annealing conditions. However, photoluminescence showed only bound-exciton spectra; no defect luminescence could be observed. The sensitivity of the PbS detector in the bound-exciton region is about one order of magnitude less than that of the S-1 photomultiplier; nevertheless, the defect peak at 915 meV (which we did not observe) should be stronger than the bound-exciton lines, denoted as AXO-TO in Fig. 4.7(a), which we did observe. We also examined a sample supplied by N.M. Johnson which is similar to those used in Fig. 4.7. In this case, broad-band defect luminescence from 1.0 eV to 0.8 eV could be measured, but no sharp peaks (such as the one at 915 meV) appeared in the spectrum. We do not understand the apparent inconsistency between our results and those of Johnson; to do so will probably require a more sensitive detector. Uebbing et al. (19) also observed no defect luminescence from solid-phase CW laserannealed samples. By correlating photoluminescence, EBIC and X-ray topography, Baumgart et al. (20) concluded that the dark stripe defects observed in EBIC and X-ray topograph consist of nonradiative defects. For deep-level non-radiative defects, DLTS is the most senstive technique, as will be discussed in the next Chapter.

References

- 1. J.R. Haynes, Phys. Rev. Lett. 4, 361 (1960).
- P.J. Dean, J.R. Haynes, and W. Flood, Phys. Rev. <u>161</u>, 711 (1967).
- P.J. Dean, W.F. Flood, and G. Kaminsky, Phys. Rev. <u>163</u>, 721 (1967).
- 4. R. Sauer, Phys. Rev. Lett. 31, 376 (1973).
- 5. K. Kosai and M. Gershenzon, Phys. Rev. B9, 723 (1974).
- 6. R.B. Hammond, T.C. McGill, and J.M. Mayer, Phys. Rev. B 13, 3566 (1976).
- K.R. Elliot et al., Phys. Rev. B<u>17</u>, 1808 (1978); S.A. Lyon et al., ibid B<u>17</u>, 2620 (1978).
- 8. T.C. McGill, Solid State Electr. 21, 1339 (1978).
- 9. M. Tajima, Appl. Phys. Lett. 32, 719 (1978).
- R. Sauer and J. Weber, Phys. Rev. Lett. <u>36</u>, 48 (1976).
- 11. M.L.W. Thewalt and J.A. Roatworowski, Phys. Rev. Lett. 41, 808 (1978).
- 12. G. Kircenow, Can. J. Phys. <u>55</u>, 1788 (1977).
- C.E. Jones, E.S. Johnson, W.D. Compton, J.R. Noonan, and B.G.
 Streetman, J. Appl. Phys. 44, 5402 (1973).
- E.S. Johnson, W.D. Compton, J.R. Noonan, and B.G. Streetman,
 J. Appl. Phys. <u>44</u>, 5411 (1973).
- J.R. Noonan, C.G. Kirkpatrick, and B.G. Streetman, Rad. Eff.
 21, 225 (1974).

- C.G. Kirkpatrick, J.R. Noonan, and B.G. Streetman, Rad. Eff.
 30, 97 (1976).
- R.A. Street, N.M. Johnson, and J.F. Gibbons, J. Appl. Phys. 50, 8201 (1979).
- 18. R.A. Street and N.M. Johnson, <u>Laser and Electron Beam Processing of Materials</u>, edited by C.W. White and P.S. Peercy (Academic Press, N.Y., 1980), p. 435.
- R.H. Uebbing, P. Wagner, H. Baumgart, and H.J. Queisser, Appl. Phys. Lett. <u>37</u>, 1078 (1980).
- 20. H. Baumgart, F. Phillipp, and H.J. Leamy, to be published in Laser and Electron Beam Interactions with Solids, edited by B.R. Appleton and G.K. Celler (North Holland, 1982).
- 21. J.J. Hopfield, <u>Physics of Semiconductors</u>, (Proceedings of the 7th International Conference, Paris 1964), p. 725.

CHAPTER 5. DEEP LEVELS IN CW BEAM-ANNEALED SI

Deep Level Transient Spectroscopy (DLTS) as first described by $Lang^{(1)}$ is perhaps the most recent and most popular of the variety of capacitance methods used for the study of electrically active defects in semiconductors. DLTS is based on the previously established technique of transient capacitance, (2) in which the occupation of a defect state in the depletion region is varied by isolating it from free carriers and subjecting it to external stimuli such as heat or light. What distinguishes DLTS from other techniques is the measurement of the transients which result from the periodic repetition of the excitation, using a fixed rate window and a variable measurement temperature. Capacitance spectroscopy is complementary to luminescence in that it is particularly good for the study of deep levels, whether they are radiative or not; shallow levels, on the other hand, (less than 0.1 eV from the band edges) are easily detected by photoluminescence but difficult to be detected by DLTS.

A good DLTS system is capable of measuring the trap concentration N_T , the trap energy level E_t , the trap profile in the diode junction region, the capture cross section σ , the optical cross section σ^o and the trapped-carrier thermal emission rate e. Transient capacitance spectroscopy can distinguish between and characterize both majority- and minority-carrier traps. It can also monitor the defect reactions in semiconductors and study the kine-

tics of these defect reactions. However, DLTS is not suitable to identify the microscopic structure and chemical nature of the defect centers involved. It is insensitive to very shallow defect levels or electrically inactive defects.

In this chapter, the use of DLTS to study the deep levels in ion-implanted Si after CW beam annealing is described. The background of this technique has been excellently reviewed in Refs. 3 and 4. The basic principles of DLTS as described in the above review papers will be summarized in Section 5.1. The DLTS system used in this work will be described in Section 5.2, followed by experimental results. A dominant hole trap (E_v + 0.45 eV) was observed in CW laser-annealed samples immediately after sample preparation. The concentration of this defect level increases more than one order of magnitude with increasing laser power. At room temperature, this defect level decays as a function of time and transmutes to another shallow level (E_v + 0.10 eV). The recovery of this 0.45eV defect level can be stimulated by low temperature annealing and minority-carrier injection. furnace-annealed control samples, rapid quenching from sufficiently high temperature into water produces defects observable by DLTS which have the same energy level and annealing characteristics as the laser-induced defects. Correlated with the literature, a model involving interstitial Fe and Fe-B pair reactions are proposed to explain the peculiar annealing characteristics and recombinationenhanced defect reactions of both thermally induced quenched-in defects and laser-induced defects in Si. The sources of Fe contamination in Si will be discussed.

5.1 <u>Transient Response of a Semiconductor Junction with Traps and</u> DLTS Spectrum

The existence of a space-charge or depletion layer at a p-n junction or Schottky barrier is a general characteristic of semiconductors. The capacitance associated with this depletion layer offers the possibility of "looking" inside the semiconductor. For simplicity, this discussion will be limited to one-sided p^+ -n junctions on uniformly doped material. It is well known that the width of the depletion layer is given by

$$W = \sqrt{\frac{2\varepsilon \left(\left| V_{bi} \right| + \left| V_{R} \right| \right)}{qN}}; \qquad (5.1)$$

and the small-signal capacitance corresponding to this depletion layer is

$$C = \frac{\varepsilon A}{W} = A \sqrt{\frac{\varepsilon q N}{2(|V_{bi}| + |V_{R}|)}}, \qquad (5.2)$$

where C is the depletion region capactiance, A is the junction area, q is the electronic charge, ϵ is the semiconductor dielectric constant, N is the ionized impurity concentration, V_{bi} is the built-in potential, and V_R is the applied reverse bias. Because states within the depeletion layer under reverse bias are empty, as shown in inset 1 of Fig. 5.1, emission processes of carriers from these states can only be observed following the forced introduction

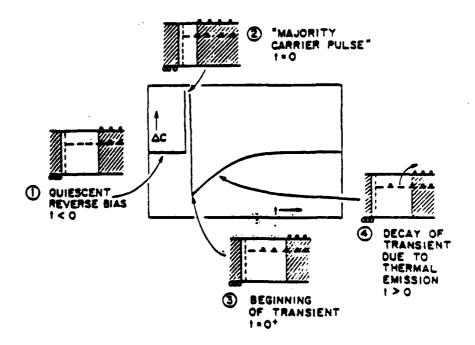


Fig. 5.1 Capacitance transient due to a majority-carrier trap in a p⁺-n diode. The small insets labelled 1 through 4 schematically show the charge state of the defect level and width of the space charge region (unshaded portion) at various times before and during the transient (after Ref. 3).

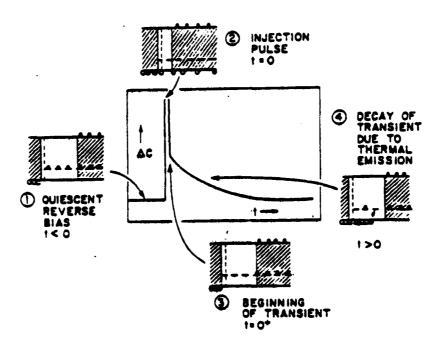


Fig. 5.2 Capacitance transient due to a minority-carrier trap in a p⁺-n diode. The small insets labelled 1 through 4 schematically show the charge state of the defect level, width of the space charge region (unshaded portion) and the injected minority carriers at various times before and during the transient (after Ref. 3).

of carriers which are to be captured. This preparation of defect charge states can be conveniently accomplished by reducing the bias momentarily, as shown in inset 2 of Fig. 5.1; part of the region which was formerly within the depeletion layer is now in neutral material so that the deep levels are below the Fermi level and may capture majority carriers to become filled. When the pulse is turned off and reverse bias V_R reestablished, as shown in inset 3 of Fig. 5.1, the junction capacitance is reduced according to Eq. (5.2), because compensating majority-carrier charge has been trapped in the space charge region. Subsequent emission of these carriers produces a capacitance transient. The capacitance transient due to majority-carrier emission is always negative, as shown in inset 4 of Fig. 5.1. The emission rate \mathbf{e}_n is related to fundamental properties of the defect as

$$e_n = 1/\tau_n = \sigma_n < v_n > N_c \exp[-(E_c - E_T)/kT]$$
 , (5.3)

where τ_n is the emission time constant, σ_n is the electron capture cross section, $\langle v_n \rangle$ is the average thermal velocity of electrons, N_C is the effective density of states at the bottom of the conduction band and E_C – E_T is the energy position of the trap center. A pulse into forward bias can be used to inject a minority-carrier population. Using analogous arguments, it can be shown that a capacitance transient due to minority-carrier emission is always

positive. Figure 5.2 shows such a transient, with insets describing the conditions of the space charge layer during the various phases of the transient, similar to the case described in Fig. 5.1.

If trap-filling pulses are repetitively applied to the sample, the resulting signal consists of a series of transients with a constant repetition rate. As the sample temperature is scanned, the time constant of the capacitance transient varies exponentially with 1/T while the capacitance itself decays exponentially as a function of time as shown in Fig. 5.3. Using a double boxcar as a signal processor, this transient can be sampled at two times, t_1 and t_2 , following each pulse; these times determine the "rate window". The DLTS signal is the difference between the transient amplitude at these two times. As seen in Fig. 5.3, there is zero difference between the signal at these two gates for either very slow or very fast transients, which correspond to low and high temperature, respectively; the difference passes through a maximum at an intermediate temperature, when the time difference $(t_2 - t_1)$ is comparable to the decay time, τ , of the transient. Specifically, this condition is given by (1):

$$\tau_{\text{max}} = \frac{t_1 - t_2}{\ln(t_1/t_2)}$$
 (5.4)

The resulting DLTS signal versus temperature dependence is called the DLTS spectrum. The peak in Fig. 5.3 will shift to a different temperature with different values of t_1 and t_2 . This peak shift

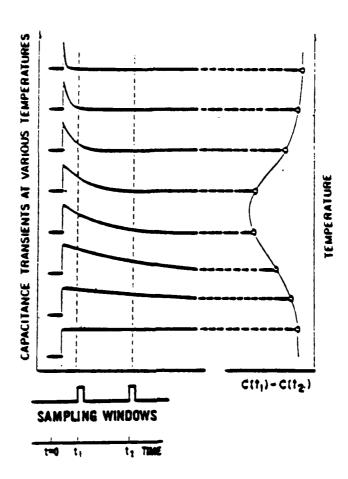


Fig. 5.3 Implementation of a rate window by means of a double-boxcar integrator. The output corresponds to the difference of the amplitudes at the sampling times t_1 and t_2 (after Ref. 1).

allows the determination of the corresponding activation energy E_{T} from an Arrhenius plot of log \mathbf{e}_{n} versus 1/T according to Eq. (5.3), repeated here as

$$\ln e_n = \ln \sigma_n < v > N_c - (E_c - E_T)/kT$$
 , (5.5)

where the term $\ln \sigma_n$ <v> N_C has been assumed to be a constant. This assumption is generally not true. Two working assumptions can be made to estimate the true defect energy level more accurately. First of all, a parabolic density of states in the band is assumed, which implies

$$N_c \alpha T^{3/2}$$
 (5.6)

In general, it is also true that

$$\langle v \rangle \alpha T^{\frac{1}{2}}$$
 (5.7)

Therefore, Eq. (5.5) can be modified as

$$\ln (e_n/T^2) = \alpha - (E_c - E_T)kT$$
 , (5.8)

where α is assumed to be a constant. From the above equation, it can be seen that an Arrhenius plot of log (e_n/T^2) versus 1/T, instead of log e_n vs. 1/T, provides the correct temperature dependence.

dence, as contained in Eqs. (5.6) and (5.7). In the simple treatment described above, capture cross sections are generally considered to be independent of temperature. While this assumption may be true for some deep levels, it is not in general true. In fact, many deep levels in III-V semiconductors have capture cross sections which are thermally activated and can be expressed as

$$\sigma_{n} = \sigma_{\infty} \exp(-E_{s}/kT) \quad . \tag{5.9}$$

Therefore, \mathbf{E}_{s} must be subtracted from the measured activation energy derived from Eq. (5.8) to get the true energy level. The measurement of capture cross sections as a function of temperature is therefore very important.

In experiments involving both thermal capture and emission, the rate equation for the occupation of a defect state of concentration N_{T} is

$$dN_t/dt = (c_n + e_p) (N_T - N_t) - (c_p + e_n) N_t$$
, (5.10)

where N_t is the concentration of defects occupied by electrons at time t and c_n and c_p are electron and hole capture rates, respectively; these are typically defined in terms of capture cross sections σ_n and σ_p , average thermal velocities $\langle v_n \rangle$ and $\langle v_p \rangle$, and free-carrier concentrations n and p as

$$c_{n} \equiv \sigma_{n} \langle v_{n} \rangle n , \qquad (5.11)$$

$$c_{p} \equiv \sigma_{p} \langle v_{p} \rangle p . \qquad (5.12)$$

For convenience in expression, let

$$a = c_n + e_p$$
 , (5.13)

$$b = c_p + e_n$$
 (5.14)

For a trap initially filled with electrons at t = 0, the solution of Eq. (5.10) gives

$$N_{t} = \begin{cases} N_{T} & t \leq 0 \\ \frac{a}{a+b} N_{T} + \frac{b}{a+b} N_{T} \exp \left[-(a+b) t\right], & t > 0 \end{cases}$$
or a trap initially empty, the solution of Eq. (5.10) is

For a trap initially empty, the solution of Eq. (5.10) is

$$N_{t} = \begin{cases} 0, & t \leq 0 \\ \frac{a}{a+b} N_{T} \{1 - \exp[-(a+b) t]\}, & t > 0 \end{cases}$$
 (5.16)

From Eqs. (5.13) and (5.14), the equilibrium occupation of a trap is given by

$$N_{\infty} = \frac{a}{a+b} N_{T} . \qquad (5.17)$$

It is common practice to assume that only one of the four rates dominates in a particular thermal capture and emission process; this considerably simplifies the solution to Eq. (5.10). For example, the electron capture process by an initially empty electron trap, as shown in the inset 2 of Fig. 5.1, is

$$N_t = N_T [1 - exp(-c_n t)]$$
 , (5.18)

from Eq. (5.16), with all rates except c_n set equal to zero. Therefore, the capture rate c_n can be determined by measuring the trap peak heights in the DLTS spectrum as a function of the trapfilling pulse width which is equivalent to t in Eq. (5.18). The capture cross section can then be determined from Eq. (5.11). If the pulse width is wide enough to fill up all the trap, the subsequent emission process is given by

$$N(t) = N_T \exp(-e_n t) , \qquad (5.19)$$

from Eq. (5.14), with all rates except $\mathbf{e}_{\mathbf{n}}$ set equal to zero. Exactly analogous expressions hold for capture and emission of holes.

The concentration of a trap can be obtained directly from the capacitance change corresponding to filling completely the trap with a wide saturating pulse. The capacitance change, ΔC , immediately after the voltage change, due to trap concentration, N_T , can be derived from Eq. (5.2) as

$$\frac{N_T}{N_s} = \frac{c_o^2 - (c_o - \Delta C)^2}{c_o^2} , \qquad (5.20)$$

where N_S is the net dopant concentration on the side of the junction where the trap is observed, and C_o is the capacitance of the diode under quiescent reverse-biased conditions. If $\Delta C \ll C_o$, then Eq. (5.20) can be simplified to

$$N_{T} \cong 2 \left(\frac{\Delta C}{C_{0}}\right) \cdot N_{s} \quad . \tag{5.21}$$

It is easy to show that ΔC can be extrapolated from the DLTS peak height, $[C(t_1) - C(t_2)]_{max}$, by the following relation

$$\Delta C = \frac{[C(t_1) - C(t_2)]_{max}}{\exp(-t_1/\tau_{max})(1 - t_1/t_2)}$$
 (5.22)

It is interesting to note that DLTS has been developed under the assumption that the transient capacitance is "exponentially" decaying. However, what really takes place inside the semiconductor is an emission process from an occupied trap. It is the trap occupation, not capacitance, which decays exponentially, as shown in Eq. (5.19). Only when $\Delta C \ll C_0$, (i.e. defect concentration is much smaller than the dopant concentration), does ΔC vary linearly with N_T, as shown in Eq. (5.21); ΔC then decays exponentially. Otherwise, when the defect concentration is comparable with or even larger than the dopant concentration, the non-

exponential behavior of the capacitance transient can be easily deduced from Eq. (5.20) and its analysis becomes more complicated.

The more convenient way to measure the spatial profiles of deep levels is to record the magnitude of a series of capacitance transients produced with majority-carrier pulses of increasing amplitude with fixed reverse bias. This method has the effect of probing the deep-level concentration inward from the depletion edge as the majority-carrier pulse is increased from zero.

Because it is so powerful for defect studies, a variety of DLTS measuring techniques have been developed; the use of these has spread rapidly in recent years. (3,4) A limitation of this method, however, is the accuracy of energy level determination. Many factors such as non-exponential decay, field-enhanced emission, non-constant capture cross sections and difficulties with sample temperature measurements may affect the energy level determination. It would not be surprising to find deviations of energy levels of \pm 5% for the same defect from author to author. For this reason, a defect can not be uniquely identified as a specific defect reported in the literature simply by its energy level. Its annealing characteristics, capture cross section, or other signatures are generally found very useful to assist in this kind of identification. The accuracy of energy-level measurements reported in this chapter is considered to be \pm 5%.

5.2 DLTS Spectrometer System

A DLTS system is a combination of different instruments. strong general background in electronic instrumentation is very helpful in building such a system. The overall experimental DLTS system used in this work is shown in Fig. 5.4. Because of its availability, a Boonton 71AR 1 MHZ capacitance meter was used to measure the capacitance transient. This meter has certain shortcomings. First, the rather slow output response time (~ 6ms) makes it impossible to measure transients faster than 6 ms. This limits the range over which emission rates can be determined to one decade only and reduces the accuracy with which the energy level of the trap can be measured. Secondly, the normal bias input reaches the sample through a heavily filtered dc network which has such a long time constant that it is impossible to use microsecond pulses; therefore, in most cases, it is impossible to measure the capture cross section directly by varying the pulse width, as discussed in the previous section. This meter incorporates a bridge circuit in which the fixed capacitance of the diode is balanced out with an ordinary capacitor. This balancing procedure permits high amplification of small capacitance changes. A home-made signal processor similar to a double boxcar signal averger was used for setting the rate window. The circuit diagram and details of its function can be found in Appendix B. The gain of this signal processor is fixed at 112. Compared with a commercial double boxcar, this home-made signal processor gives a better signal to noise ratio with the same

DEEP LEVEL TRANSIENT SPECTROSCOPY [DLTS]

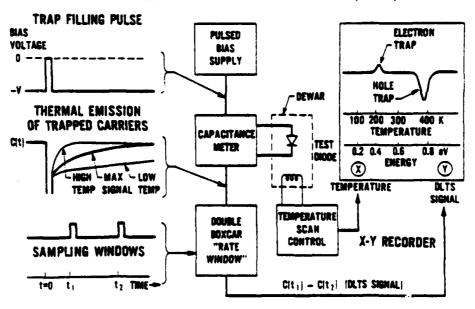


Fig. 5.4 Block diagram showing the essential features of a DLTS spectrometer (after Ref. 4).

time constant. Its disadvantage is that it has only dc coupling. The input signal must be constantly monitored to keep it within \pm 10 mV by adjusting the zero setting in order to prevent the operational amplifier from saturating. Should it be necessary to use a commercial double boxcar to replace the home-made one, care must be taken to avoid signal distortion because of another problem: the output impedance (1M Ω) of the Boonton 71AR does not match the input impedance (50 Ω) of the commercial double boxcar. Therefore, a preamplifier (e.g., PAR 113) must be used to couple the signal from the capacitance meter to a commercial double boxcar (such as the PAR 164) when the latter is used. The system described here can detect trap concentrations about 3 to 4 orders of magnitude smaller than the majority carrier concentration in the diode substrate. This sensitivity was found to be adequate for general purposes.

A digital temperature controller (Eurotherm Model 919) with a programmer (Eurotherm Model 125) was used to control the temperature scan. Two identical "type-T" thermocouples (Copper-Constantan) were used to measure the sample temperature: one for temperature controller input, the other for the x-axis input of the x-y recorder; this elimiantes loading problems. Electrical bridge cold-junction compensators (Model OMEGA-CJ) were employed with these thermocouples for accurate temperature measurements. The output of the temperature controller was buffered by a home-made circuit and fed to the input of a DC power supply (Sorensen Model DCR 40-13B) the output of which was connected to a heater directly

below the sample in the gas flow dewar. The complement of the temperature controller output (i.e. $V_2=10~{\rm volts}-V_1$, where V_1 is the temperature controller output), is fed to an identical DC power supply to control a second heater in the liquid nitrogen (LN₂) dewar. Therefore, during the cooling cycle, the output of the heater in the LN₂ dewar increases with time while the heater output in the gas flow dewar decreases. These functions are reversed during the heating cycle. The details of this home-made circuit for temperature scanning can be found in Appendix C. A temperature accuracy of 1-2K could be achieved with such a system.

5.3 <u>Sample Preparation for DLTS Measurements</u>

Boron-doped (\sim 10-20 Ω -cm) Si with <100> orientation was implanted with As⁺ at 100 keV to a dose of 4×10^{15} cm⁻² and then annealed with either a CW Ar⁺ laser at elevated substrate temperatures, or with a scanning electron microscope (SEM) modified for high-current operation. After beam annealing, the resulting n⁺-p junction diodes were processed by conventional photolithography and plasma etching to define circular mesa structures of diameter 1.2 mm for standard DLTS measurements. Front- and back-side ohmic contacts were formed as described in Chapter 3. The final mesa diodes were mounted on TO-5 headers and hand-bonded with conducting epoxy and Au wires. During the processing, the temperature was kept below 100° C after beam annealing. The samples mounted in this way were then put into a gas-flow dewar for DLTS measurements.

Both n- and p-type Si wafers were also implanted with Si^+ at 80 keV to a dose of $2 \times 10^{15} / \mathrm{cm}^2$. After beam annealing, Schottky barriers were made by evaporating Au on n-type and Ti on p-type Si, respectively.

5.4 Deep Levels in Ion-implanted Si after Beam Annealing

Figure 5.5 shows a typical DLTS spectrum (with 10 V reverse bias) immediately after the samples were beam-annealed and processed. For CW laser annealing, Fig. 5.5(a), a dominant hole trap with energy level close to mid-bandgap, about 0.45 eV above the valence band, has been observed in slip-free samples. For convenience, it is denoted as H(0.45) here H stands for hole trap. At low laser power, this defect signal is small. However, the signal increases rapidly with increasing laser power, as shown by curve (b). The energy level of this defect does not appear to depend on substrate temperature (at least in the range $250^{\circ}\text{C} < T_{c} < 350^{\circ}\text{C}$) during annealing. When the laser power is sufficiently high to produce slip dislocations, the spectrum is in general broad and the dominant defect level does depend on the substrate temperature: for $T_s = 250$ °C it appears at 0.43 eV above the valence band, H(0.43), as seen in Fig. 5.6(a), with two small peaks, H(0.20) and H(0.32). For $T_s = 350^{\circ}C$, the dominant defect level appears at $E_v +$ 0.32eV superposed on a broadband background, as seen in Fig. The SEBA result is quite different, as shown in Fig. 5.5(c); for slip-free samples, only a weak signal is observed at $\rm E_{v}$ + 0.40 eV, which does not depend strongly on electron-beam power.

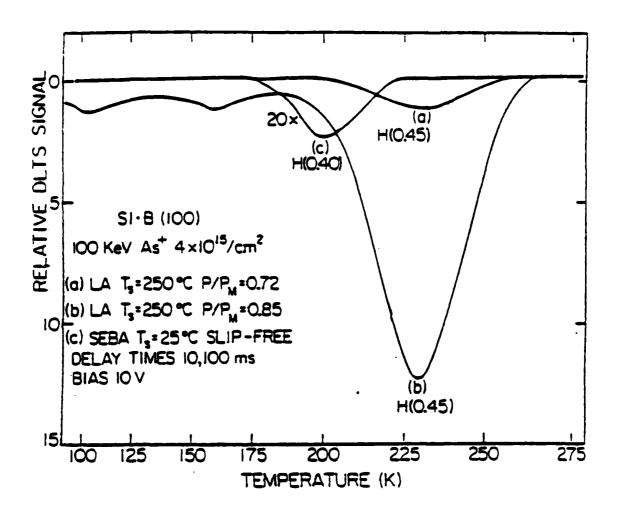


Fig. 5.5 Capacitance transient spectrum of p-type Si implanted with As⁺ and annealed by either a CW Ar⁺ laser (LA) using three different values of laser power, or annealed with a scanning electron beam (SEBA). T_S is the substrate temperature during beam annealing. All samples in this figure are slip-free.

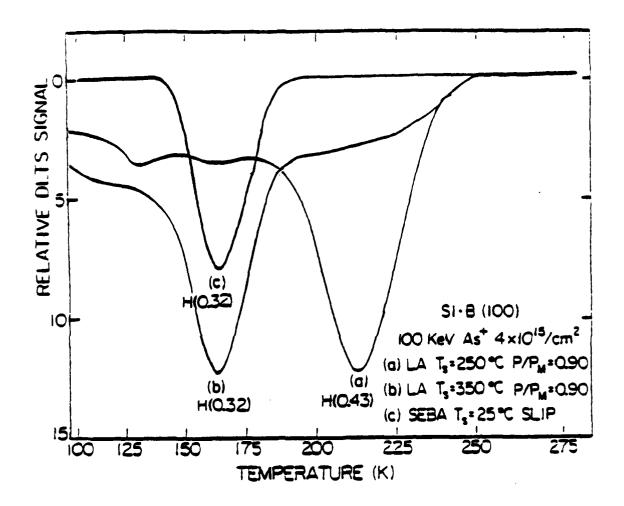


Fig. 5.6 Capacitance transient spectrum of laser- or electron-beam-induced slip dislocations. $T_{\rm S}$ is the substrate temperature during beam annealing.

This defect spectrum in Fig. 5.5 differs from that reported earlier in beam-annealed Si.(5,7) When the electron beam introduces slip dislocations, the defect level appears at $E_{\rm v}$ + 0.32 eV; a defect at this level also appears in all laser-induced slip samples as seen in Fig. 5.6. It is interesting to compare this result with the EBIC display in Fig. 3.10 where the dominant slip line in the SEBA sample is perpendicular to the beam scanning direction. suggests that the other defect levels in LA samples containing slip might be related to dislocations extending in other directions. Since the dislocation acts as a very efficient sink for point defects, those defects remaining after beam quenching may interact with the dislocations to form different centers. In slip-free samples, on the other hand, these point defects may coalesce to form new defect structures. For these reasons it is not surprising that the defect spectrum in slip-free samples (Fig. 5.5) is so different from that in slipped samples (Fig. 5.6). In Fig. 5.7, the defect concentration is plotted as a function of beam power. In general, the defect concentration of scanning-electron-beamannealed samples is lower than laser-annealed samples and is relatively insensitive to electron-beam power. However, for laserannealed samples, the defect concentration increases more than one order of magnitude with increasing laser power. For high-power laser-annealed samples, the defect concentration is comparable to the substrate dopant concentration. If this is compared with the

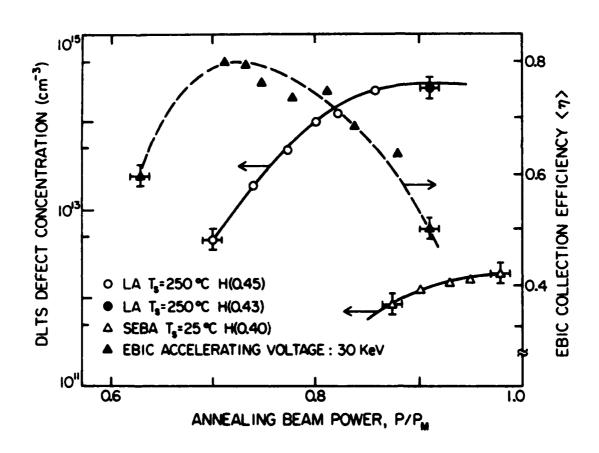


Fig. 5.7 Defect concentration measured by DLTS, as a function of annealing beam power. The broken curve displays the EBIC charge-collection efficiency as a function of laser power.

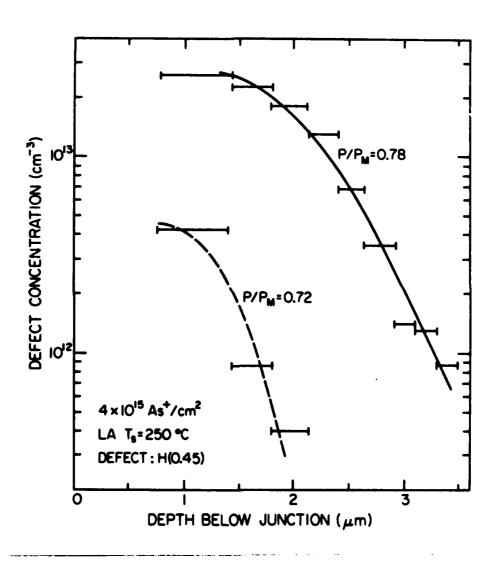


Fig. 5.8 Spatial depth profile of the defect H(0.45) for two samples annealed with different laser power.

EBIC results, shown by the broken curve in Fig. 5.7, it can be seen that the EBIC charge collection efficiency decreases as this defect concentration increases. In Fig. 5.8 the defect depth profile is displayed for two samples annealed at different laser power. As the laser power increases, not only does the defect concentration increase, but also the defect depth increases. These laser-induced defects can extend several microns below the implanted junction. Similarly deep defects have also been observed in beam-annealed Si by Johnson et al. (5,6)

5.5 Thermal Behavior of Laser-Induced Defects

The thermal behavior of the laser-induced defect, H(0.45), is extremely interesting, because it is not stable at room temperature. In Fig. 5.9 the defect concentration is plotted as a function of time, and for various annealing procedures. For laser-annealed samples with slip dislocations, the defect H(0.43) is very stable, as shown by the solid points. However, for slip-free samples the defect density decays dramatically with time (open circles). Ten days after annealing, this dominant defect is not detectable. However, after this defect level disappears, it can be made to reappear by low temperature thermal annealing at $\sim 100^{\circ}$ C. The density of the reactivated defect depends on the annealing temperature and time, as shown in Fig. 5.9. Finally, this defect level can be completely elminated, never to be observed again, by annealing at 300°C for 30 min.

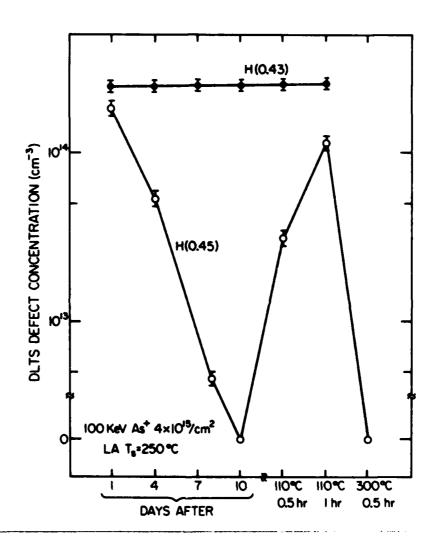


Fig. 5.9 Thermal behavior of laser-induced defects. The defect accompanied by slip formation is stable (solid points). For slip-free samples (open circles), the defect signal decays with time and can be reactivated by low temperature annealing.

In order to gain more information about the defect-reaction behavior in CW laser-annealed samples, liquid helium was used to complete this study. Figure 5.10 shows a typical DLTS spectrum scanned from 43K to 300K with a bias pulse from 10 V to 0 V. Four hole traps are visible with energy levels as follows: $E_v + 0.10$ eV, E_V + 0.20 eV, E_V + 0.28 eV, and E_V + 0.45 eV; these are denoted as H(0.10), H(0.20), H(0.28) and H(0.45) respectively. The H(0.10)defect level was not observed in Fig. 5.5 because low-temperature measurements were not made. The H(0.28) level has been reported by Johnson et al.(5) in similar CW laser-annealed samples; in this study it is not present when the substrate temperature (T_s) is 250°C during annealing, but it appears for $T_s = 350$ °C. The concentrations of both H(0.20) and H(0.28) are small compared with the two dominant defects, H(0.10) and H(0.45); however, the concentrations of the latter are strong functions of the time after sample preparation and of subsequent thermal treatments. This is shown in The behavior of H(0.45) with annealing between room temperature and a few hundred degrees has already been shown in Fig. 5.9. Figure 5.11 shows that H(0.10) behaves oppositely. It is clear from these data that H(0.45) and H(0.10) are related to each other; creation of one of these defects is accompanied by the annihilation of the other. Immediately after laser annealing, H(0.45) is dominant; however, it gradually decays at room temperature, while H(0.10) simultaneously increases. The recovery of H(0.45) can be stimulated by low-temperature annealing (100°C-

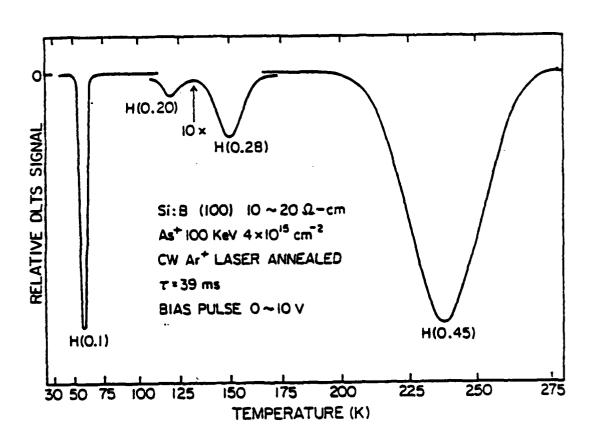


Fig. 5.10 Typical capacitance transient spectrum of p-type Si implanted with As^+ and annealed by a CW Ar^+ laser. This spectrum was obtained ~4 days after sample preparation, so that the H(0.10) and H(0.45) peaks are of comparable strength.

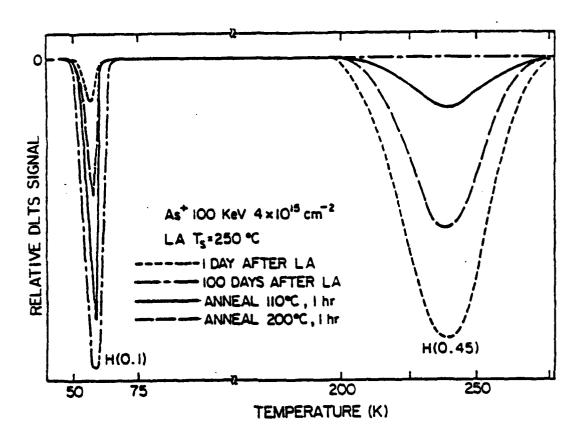


Fig. 5.11 The transmutation between the deep level H(0.45) and the shallow level H(0.10) during room-temperature anneal. The restoration of H(0.45), and consequent annihilation of H(0.10), can be stimulated by annealing at $100-200^{\circ}C$.

 200° C), also shown in Fig. 5.11, with the accompanying decrease in H(0.10). The sum of the concentrations of both traps always remains constant.

The kinetics of this defect reaction is certainly complicated and systematic study is required. Laser-annealed samples were stored at room temperature for 3 months and then isothermally annealed at various temperatures below 200° C. The recovery of H(0.45) was observed to increase with annealing time and eventually to saturate. The reversible thermal equilibrium between

$$H(0.10) \quad H(0.45)$$
 (5.23)

can be established by low-temperature annealing. The equilibrium concentration of H(0.45) increases with annealing temperature in the temperature range studied here. From chemical reaction kinetics, the equilibrium constant K in Eq. (5.23) can be expressed as

$$K = \frac{[H(0.45)]}{[H(0.10)]} = \exp(\frac{\Delta S}{k}) \exp(-\frac{\Delta H}{kT})$$
, (5.24)

where ΔS is change in entropy and ΔH is change in enthalpy. Figure 5.12 shows an Arrenhius plot of the logarithm of equilibrium concentration ratio, [H(0.45)]/[H(0.10)], versus inverse temperature. The data can be fitted to Eq. (5.24) with slope ΔH = 0.66 eV and extrapolated intercept ΔS = 19.26k.

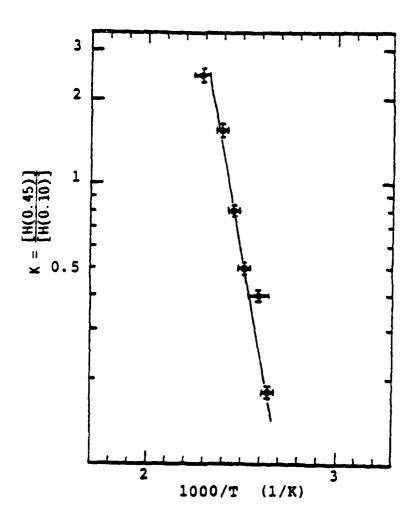


Fig. 5.12 Arrenhius plot of the equilibrium constant. K = [H(0.45)]/[H(0.10)], versus inverse temperature.

5.6 Recombination-Enhanced Defect Reaction

The recovery of H(0.45) can be stimulated not only by thermal activation, as described in the previous section, but also by minority-carrier injection. By forward-biasing the junction, a similar transmutation behavior from H(0.10) to H(0.45) has been observed, as shown in Fig. 5.11. The recovered concentration of H(0.45) increases with injected current and time. The reaction rate can be estimated by assuming a first-order reaction, for which

$$dN_{T}(t)/dt = -N_{T}(t) \exp(-E_{a}/kT)$$
 , (5.25)

where $N_T(t)$ is the defect concentration, i.e. [H(0.10)] in this case, at time t and E_a is the activation energy. Integration of Eq. (5.25) yields

$$f = N_T(t)/N_T(0) = \exp(-t/\tau)$$
, (5.26)

where $1/\tau$ is the reaction rate and is related to the activation energy \boldsymbol{E}_a by the expression

$$1/\tau = v \exp(-E_a/kT)$$
 , (5.27)

where v is the frequency factor for this reaction.

In Fig. 5.13 the logarithm of the defect concentration, H(0.10) (normalized to t=0) is plotted as a function of time, for

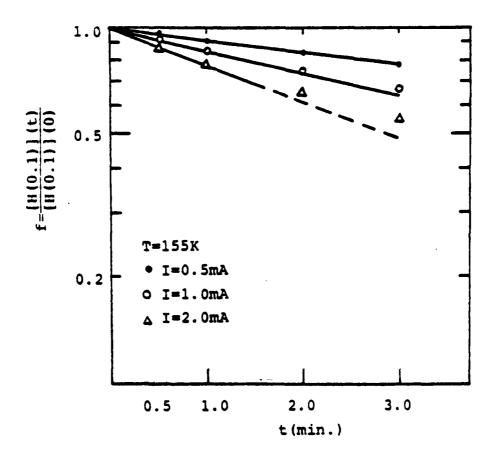


Fig. 5.13 The ratio of defect concentration, H(0.10), after and before current injection as a function of injection time at T=155K.

various values of injected current. During current injection, the sample was kept at T = 155K for these data. Although the results deviate from a straight line, especially at high current injection, they can be approximated to a first-order reaction, as in Eq. (5.26), and the reaction rate can therefore be estimated from the slope. Figure 5.14 shows how the reaction rate, determined in this fashion, increases with injection current. Attempts to determine the activation energy of this reaction by measuring the reaction rate at different temperature, according to Eq. (5.27) were not successful because the reaction rate was relatively insensitive to temperature in the range of 133K to room temperature. This implies that the activation energy, E_a , must be very small. Finally, the stimulation of this reaction by minority-carrier injection can be effectively quenched at 77K.

The role of electron-hole recombination in electronic stimulation processes has been reviewed by Kimerling. (8,9) This mechanism, known as recombination enhancement, refers to any reaction path in which vibrational energy deposited locally at a defect center by a non-radiative electronic transition serves to increase the reaction rate. Therefore, a defect in an exicted vibrational state may experience reactions (such as diffusion, dissociation, and annihilation) which would not proceed under the equilibrium Boltzman distribution of energies determined by the temperature of the quiescent host lattice. Clearly, a detailed understanding of recombination-enhanced defect processes is very important, for it

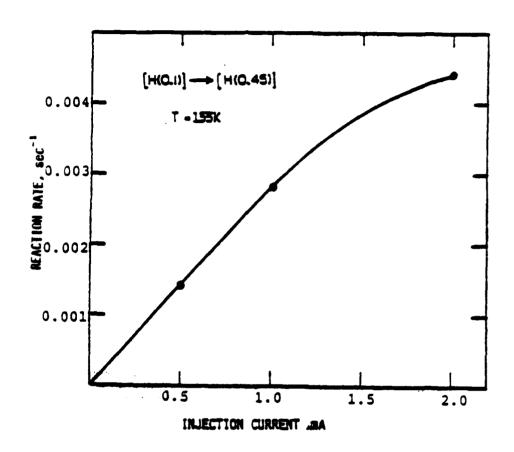


Fig. 5.14 Minority-carrier injection stimulated defect reaction rate as a function of injected current at T=155K.

will greatly increase our understanding not only of defect motion but also of possible mechanisms of nonradiative recombination as well. In this respect, DLTS provides a unique and powerful ability to isolate and monitor electronic stimulation processes directly by measuring the defect concentrations and the rate of electronic transitions at a particular defect. It has been successfully applied to characterize the recombination-enhanced process for defect states in larger-energy-gap materials, such as ${\rm GaAs}^{(10)}$ and ${\rm GaP}^{(11)}$. The concept of recombination-enhanced defect reaction was also introduced to explain the degradation of light emitting diodes⁽¹²⁾ and laser diodes⁽¹³⁾ during forward bias injection but not under reverse bias. Its effects on the performance of laser-annealed devices will be very interesting. These have been under investigation⁽¹⁴⁾ at Bell Laboratories since the preliminary results of this chapter were published.

5.7 Deep Levels in Laser-Annealed Self-Implanted Si

Both p- and n-type Si wafers were implanted with Si $^+$ ions at 80 keV to a dose of $2x10^{15}$ cm $^{-2}$ and then annealed by a CW laser. The study of these self-implanted samples serves two purposes. First, it is possible that the majority carrier DLTS signals in As $^+$ implanted n $^+$ -p junctions might be due to electron traps in the n $^+$ recrystallized layer, instead of hole traps in the p-type substrate. This is unlikely, since most of the depletion region is on the p-side for an abrupt n $^+$ -p junction. Nevertheless, a very high

density of electron traps on the n⁺-side could be mistaken for hole traps in the substrate. Secondly, in the event that all defects reported above really are from the substrate, the study of self-implanted samples (i.e., Si⁺ implants) makes possible a search for other deep levels in the recrystallized implanted layer. This was done by applying a Schottky barrier to the surface, since no p-n junction is formed by self implants. It was found that the deep-level spectrum of self-implanted p-type samples annealed by CW laser is exactly the same as that for the As⁺-implant case (i.e. Fig. 5.10), and no other defects have been observed. Therefore, it can be concluded that all those deep levels in Fig. 5.10 are from the p-side of the sample.

Deep levels in self-implanted and laser-annealed n-type Si have been studied in detail by Johnson et al., $^{(6)}$ who observed high densities of deep levels. The spectrum shown in Fig. 5.15 for Czochralski-grown wafers has been repeated in this work. The dominant electron trap is E_c - 0.49 eV; it is found in this work that the concentration of this trap is weakly dependent on laser power. This defect level is only partially removed by a 600°C anneal, and is completely removed after a 800°C anneal. No microscopic structure for this defect has been proposed. It is interesting to note that, in n-type wafers implanted with B^+ at 100 keV to a dose of 1×10^{15} cm² and annealed by CW laser, we have observed no defect levels in this kind of p^+ -n junction. Therefore, the spectrum shown in Fig. 5.15 must be related to defects in

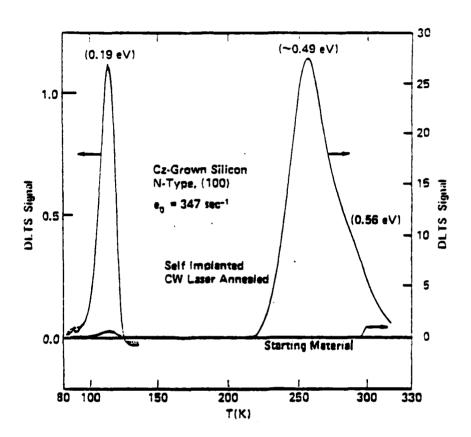


Fig. 5.15 DLTS spectrum of self-implanted, CW laser-annealed Cz-grown silicon. Note the polarity of the DLTS signal in this figure has been reversed (after Ref. 6).

the recrystallized amorphous layer, instead of defects in the substrate.

5.8 <u>Comparison with Furnace-Annealed Control Samples</u>

In order to investigate the nature of these laser-induced defects, the above results are compared with furnace-annealed control samples. In Fig. 5.16, the broken line is plotted for samples annealed at 1100° C in N₂ ambient for 1 hr, followed by different cooling time before quenching in water. When the sample was gradually removed from the furnace and slowly cooled, no defects have been observed. However, for rapid quenching, the H(0.45) defect appears immediately after sample preparation. This defect concentration increases with quenching rate. In another experiment, shown by the solid line, samples were furnace-annealed at different temperatures for 1 hr, followed by rapid quenching in In this case the same defect H(0.45) appears with a concentration that depends on annealing temperature. This H(0.45) defect in thermally-annealed material also decays and transmutes with time to the shallow defect H(0.10). It also shows the same overall low-temperature annealing behavior and minority-carrierinjection-enhanced reaction as that for the laser-annealed case. similarity between laser-induced defects and thermally This quenched-in defects can be understood by the fact that the dwell time of the laser spot is only a few milliseconds; hence, laser annealing is also a thermal quenching situation. However, it is

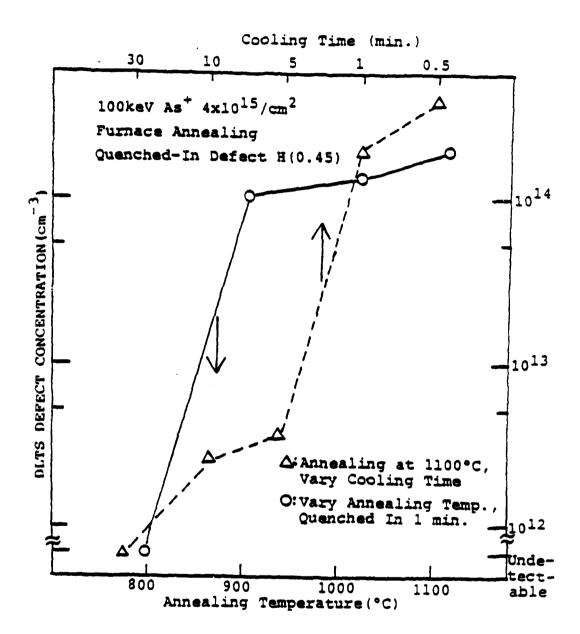


Fig. 5.16 The dependence of defect concentration, H(0.45), on thermal annealing temperature (solid line) and on cooling time (dashed line). Δ: furnace-annealed at 1100°C for l hour with different cooling time. o: Furnace-annealed at different temperature and quenched into water for l minute.

not at all clear why the electron-beam annealing does not produce the same defects.

5.9 Identification of Quenched-In Defects in CW Laser-Annealed Si

There is a considerable body of information in the literature, published during the last two decades, concerning a quenched-in defect in Si. The original experiments reported electrical measurements (15-17). These experiments consistently indicated that a carrier trap (E_v + \sim 0.40 eV) exists in quenched silicon, with a formation enthalpy ~2.5eV. In 1977, this quenched-in defect was first identified microscopically, using electron spin resonance (ESR) as Fe on the tetrahedral interstitial site $^{(18)}$, although Fe was not expected to be present. Gerson et al (19) extended the ESR result using DLTS on similarly-quenched Si samples which were again thought not to contain Fe. A deep level at $E_{_{\rm V}}$ + 0.45 eV was correlated with interstitial Fe as the most important thermallyinduced quenched-in defect in Si. Both $ESR^{(18)}$ and $DLTS^{(19)}$ signals due to interstitial Fe decay with time if the samples were stored at room temperature. Since then, the presence of Fe in silicon has been the subject of growing interesting. The present understanding of the structure of defect sites due to transition metal impurities is based on the pioneering ESR studies of Ludwig and $Woodbury^{(20)}$. The interstitial Fe reacts with shallow acceptors such as B, Al, Ga and In at room temperature to form pairs which are oriented in a <111> -direction (with the exception of Fe-In which shows <100>-symmetry). Feichtinger (21) has proposed that an Fe-B pair exists with a defect state located at $E_{\rm V}$ + 0.1eV. Graff et al. (22,23) and Kimerling et al. (24,25) have recently confirmed this assignment with respect to the H(0.10) peak of the DLTS spectrum of Fe diffused silicon. In those investigations, Fe was intentionally diffused into B-doped Si and quenched, and then studied in detail using DLTS, minority-carrier lifetime measurements, infrared absorption spectroscopy and x-ray topography. A deep level E_{ij} + 0.43 eV was observed due to interstitial Fe. This defect concentration decays with time and transmutes to $\rm E_{v}$ + 0.10 eV, which was attributed to Fe-B pairs. After quenching, the minority-carrier lifetime was considerably reduced. The dissociation of Fe-B pairs to interstitial Fe can be stimulated by lowtemperature annealing and light illumination. (22) Recombinationenhanced dissociation of Fe-B pairs to interstitial Fe by minoritycarrier injection was also observed in n⁺-p junctions containing $Fe^{(25)}$. By annealing above 300°C, both interstitial Fe and Fe-B pairs disappeared due to precipitation of Fe. This was detected by x-ray topography since the DLTS signal disappears. By correlating the above literature results with all of the experiments described in this chapter, it is noted that the furnace-annealed and quenched control samples exhibit defect behavior identical to those observed in laser-annealed samples: the defect energy levels, transmutation behavior, low-temperature annealing and recombination-enhanced dissociation are all the same. It is clear, therefore, that the dominant defect levels, H(0.45) and H(0.10), in the CW laser-annealed samples resulted from quenched-in interstitial Fe and Fe-B pair reactions in Si. The detailed kinetics of this pair reaction is still not well understood. From isothermal annealing experiments, the activation energy required for the quenched-in defect migration was determined to be 0.69 eV⁽¹⁸⁾, which is very close to the $\Delta H = 0.66$ eV as determined in Section 5.5. The isochronal annealing studies also showed that the quenched-in defect annealing temperature varies as a function of boron concentration⁽¹⁹⁾. This indicates that the boron effect is complex and not clear.

The other defect observed in this work, H(0.28), has been proposed to be due to interstitial carbon⁽⁷⁾; however, there is no experimental evidence to support this assignment. The microscopic origin of other defects, such as H(0.20) in laser-annealed samples and H(0.40) in electron-beam annealed samples, have not been identified. Nevertheless, their concentrations are much less than that of the laser-induced quenched-in defects, H(0.45) and H(0.10).

5.10 Sources of Fe in Si

Since Fe was first identified as the most important thermal quenched-in defect in presumably clean Si wafers from eight different suppliers using different heating methods $^{(18)}$ and since those results are reproducible in different laboratories $^{(21,26)}$, the presence of Fe in Si has been the subject of growing interest. The solubility of Fe in Si as a function of temperature can be expressed as $^{(22,27)}$

[Fe] =
$$5x10^{22} \exp(7.3 - 2.87 \text{ eV/kT})$$

Fe diffuses interstitially into Si with a large diffusion constant $D \sim 4 \times 10^{-6} \text{ cm}^2 \text{s}^{-1}$ at 1100°C with an activation energy of about 0.9 eV⁽²⁷⁾. Because of its high solubility and large diffusion constant, Fe is easily introduced into Si during any form of heat treatment or chemical processing. Using neutron activation analysis (NAA), concentrations of 1×10^{12} to 5×10^{13} Fe atoms/cm³ have as-received commercial float-zone detected in wafers, (22,27) and about a factor of 5~10 higher has been observed in Czochralski-grown wafers. After thermal annealing and quenching these as-received wafers, Fe contamination as high as $\sim 10^{15}/\text{cm}^3$ has been detected by either NAA $^{(27)}$ or ESR $^{(18)}$. By studying the dependence of the total Fe concentration in Si on the heating time, Webber (27) et al. have concluded that Fe was introduced into Si in two steps. In the first step, Fe contamination of the surface of the sample (most probably from the solvents used) diffuses into the specimens, whereas the second step consists of Fe - possibly from the hot quartz tube - transferred to the sample by the flushing gas.

For laser-annealed samples, it is less likely that Fe diffuses from the environment (i.e., the second step described above) into Si during the short dwell time of each laser spot. Therefore, lower Fe contamination in laser-annealed samples can be expected. The fastest quenching rate in the thermal annealing experiment,

Fig. 5.16, is ~35°C/sec, which is much slower than the quenching rate of our typical laser-annealing conditions ($\sim 5 \times 10^{5}$ oC/ sec). However, the Fe concentration in Fig. 5.16 is comparable to or higher than that observed in laser quenched-in samples (Fig. 5.9). Therefore, the quenched-defect concentration in laser-annealed samples appears to be reduced because there are fewer sources of Fe contamination. Thus far, any experiment with implants in this work has been unable to completely eliminate these Fe-related laserinduced defects, despite care in processing. In an attempt to find the source of Fe in our CW laser-annealed samples, a piece of Float-zone (FZ) Si wafer with low Fe contamination ($\sim 10^{11}$ cm⁻³ as specified by the supplier) from Bell Laboratories was compared with another piece of Czochralski-grown (CZ) wafer used for most of the experiments reported in this thesis. Each wafer was cut into two halves; one was implanted with As at 100 keV to a dose of 4×10^{15} cm⁻² and the other remained as original. These four sets of samples were chemically processed at the same time, handled with Teflon tweezers, and laser-annealed in the same run. Figure 5.17 shows the defect concentration due to interstitial Fe, H(0.45), in these samples immediately after sample preparation. For samples subjected to As implants, this Fe-related defect concentration and its dependence on laser power are quite similar for both FZ (solid circles) and CZ (solid triangles) samples. However, for laserannealed non-implanted samples, it is surprising to observe a high concentration of the quenched-in defect in supposedly low Fe-

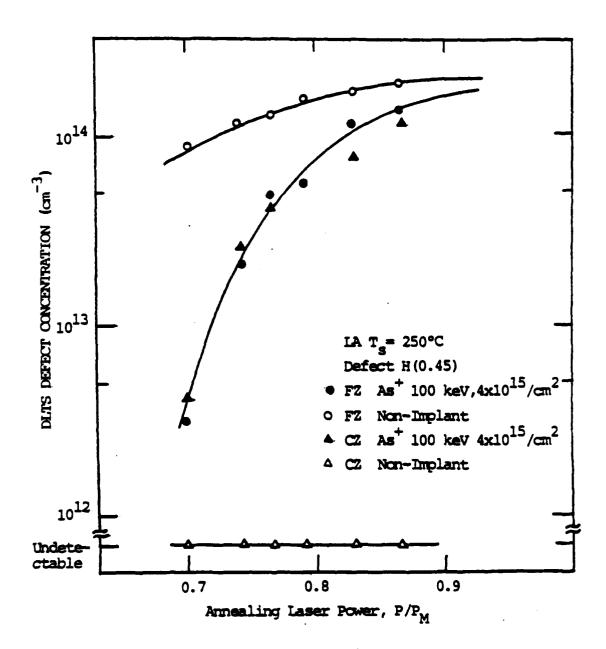


Fig. 5.17 Fe-related defect concentration measured by DLTS, as a function of annealing laser power, for four sets of samples processed at the same time.

contaminated FZ samples (open circles), but not in CZ non-implanted samples (open triangles). Since the depletion region of the Schottky barrier can extend to the surface, the higher defect concentration of non-implanted FZ samples compared to the same wafer with implants suggests the near-surface region of this wafer has been contaminated by Fe. This contamination is less likely to be introduced in our laboratory during the processes, since no Fe-related defects were observed in the ion-implanted CZ samples. However, both FZ and CZ samples have similar Fe concentration after implantation; this suggests that Fe was introduced into Si during the implantation process. It is proposed therefore, that the presence of Fe in laser-annealed samples may result from the following sources. Initially, the sample surface is contaminated during chemical processing - from the solvents, beakers and tweezers used for standard processing. During ion-implantation, this surface Fe is driven into the wafers by the high-energy incident ions. It has also been reported (28) that, for high-dose implantation, considerable sputtering occurs, introducing Fe and other heavy metals from various apertures of the implant accelerator into the wafers (28). In both cases, the contamination of Fe increases with implant accelerating voltage, ion mass and dose. Since the surface of the samples prepared for laser annealing is usually amorphous, the original Fe in the substrate has the tendency to be gettered to the damaged surface during annealing, so that it is quenched near the junction. All of these sources make it difficult to keep Si wafers free from Fe.

It has been found, however, that by increasing the substrate temperature from 250°C to 350°C, a significantly lower concentration of laser-induced defects is observed; this is also shown in Fig. 5.18. This may result from either of two effects: (1) the laser-induced defects are partially annealed because of the 350°C substrate temperature, which causes Fe to precipitate, or (2) fewer defects are produced by the laser, because much lower laser power is required to anneal the implant damage due to the higher substrate temperature. In either case, the concentration of H(0.45) is reduced by higher substrate temperature during annealing.

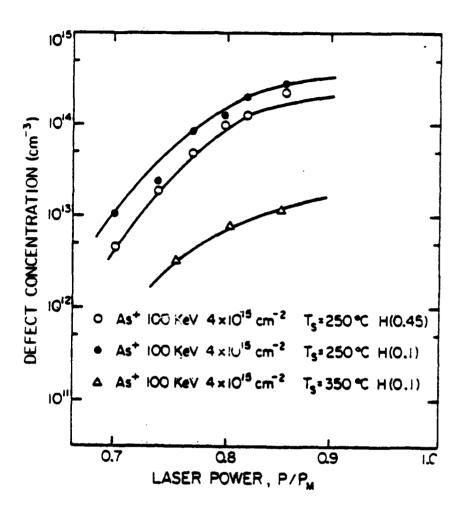


Fig. 5.18 Defect concentration measured by DLTS, as a function of annealing laser power. $T_{\rm S}$ is the substrate temperature during laser annealing; $P_{\rm M}$ is the laser power for melting.

References

- 1. D.V. Lang, J. Appl. Phys. 45, 3023 (1974).
- For a review, see C.T. Sah, Solid-State Electron. 19, 975 (1976).
- G.L. Miller, D.V. Land and L.C. Kimerling, Ann. Rev. Mater.
 Sci. 7, 377 (1977).
- D.V. Lang, <u>Thermally Stimulated Relaxation in Solids</u>, edited by P. Braunlich, (Topics in Applied Physics, Vol. 37, Springer-Verlag, Berlin, 1979) p. 93.
- N.M. Johnson, D.J. Bartelink, M.D. Moyer, J.F. Gibbons, A. Lietoila, K.N. Ratnakumar, and J.L. Regolini, <u>Laser and Electron Beam Processing of Materials</u>, edited by C.W. White and P.S. Peercy (Academic Press, New York, 1979) p. 423.
- 6. N.M. Johnson, R.B. Gold, and J.F. Gibbons, Appl. Phys. Lett. 34, 704 (1979).
- 7. N.M. Johnson, J.L. Regolini, D.J. Bartelink, J.F. Gibbons, and K.N. Ratnakumar, Appl. Phys. Lett 36, 425 (1980).
- 8. L.C. Kimerling, Solid-State Electron. Vol. 21, 1391 (1978).
- 9. L.C. Kimerling, <u>Defects and Radiation Effects in Semiconductors 1978</u>, edited by J.H. Albany, (Inst. Phys. Conf. Ser. No. 46, 1979), p. 56.
- 10. D.V. Land and L.C. Kimerling, Phys. Rev. Lett. <u>33</u>, 489 (1974).
- 11. D.V. Lang, L.C. Kimerling, and S.Y. Leung, J. Appl. Phys. <u>47</u>, 3587 (1976).

- 12. H. Kressel and N.E. Byer, Proc. IEEE 57, 25 (1969).
- R.L. Hartman, B. Schwartz, and M. Kuhn, Appl. Phys. Lett. <u>18</u>, 304 (1971).
- 14. G.L. Miller, private communication (Nov. 1981).
- L. Elstner and W. Kamprath, Phys. Status Solidi, <u>22</u> 541 (1967).
- 16. M. Swanson, Phys. Status Solidi, 33, 721 (1969).
- 17. W. Leskoschek, H. Feichtinger, and G. Vidrich, Phys. Status Solidi, A20, 601 (1973).
- Y.H. Lee, R.L. Kleinhenz, and J.W. Corbett, Appl. Phys. Lett.
 31, 142 (1977).
- J.D. Gerson, L.J. Cheng, and J.W. Corbett, J. Appl. Phys. <u>48</u>, 4821 (1977).
- 20. G.W. Ludwig and H.H. Woodburg, Solid State Physics 13, 223 (1962).
- 21. H. Feichtinger, <u>Defects and Radiation Effects in Semiconductors</u>, edited by J.H. Albany (Inst. Phys. Conf. Ser. 46, 1979), p. 528.
- 22. K. Graff and H. Pieper, J. Electrochem. Soc. <u>128</u>, 669 (1981).
- K. Graff and H. Pieper, <u>Semiconductor Silicon-1981</u>, edited by
 H. R. Huff and E. Sirtl, (Electrochem. Soc., 1981) p. 331.
- 24. L.C. Kimerling, J.L. Benton, and J.J. Rubin, <u>Defects in Semiconductors 1980</u> (Inst. of Physics, London, 1981).
- 25. L.C. Kimerling, <u>Defects in Semiconductors</u>, edited by J. Narayan and T.Y. Tan (North-Holland, 1981), p. 85.

- 26. E. Weber and H.G. Riotte, Appl. Phys. Lett. <u>33</u>, 433 (1978).
- 27. E. Weber and H.G. Riotte, J. Appl. Phys. <u>51</u>, 1484 (1980).
- 28. W. Hass, H. Glawischnig, G. Lichti, and A. Bleier, J. Electron. Mat. 7, 525 (1978).

6.1 Summary

The conclusions obtained in this thesis concerning minority-carrier recombination processes and electronically active defects in CW beam-annealed Si can be summarized as follows:

- 1. All EBIC, photoluminescence and DLTS experiments show that the "window" for successful laser annealing is quite narrow; low charge-collection efficiency, with a high-contrast EBIC pattern of dark stripes running parallel to the laser scan, usually results. The concentration of electronically active defects increases more than one order of magnitude with increasing laser power, as measured by DLTS.
- 2. Optimum laser annealing is obtained for a highly overlapping scan of a large-diameter (approximately 100 µm) laser spots, at a laser power just above the threshold for the initiation of annealing (approximately 70-75% of the power required for melting). At lower laser power, inadequate annealing results in low charge collection efficiency. At higher laser power, there is strong evidence for the existence of laser-induced damage, which extends into the bulk of the wafer below the implanted layers. As the laser power approaches that required to melt the Si wafer, the damage takes the form of slip dislocations.
- 3. Electron-beam annealing is found to be generally superior to laser annealing in most respects thus-far investigated. Dark stripes are difficult to observe in the EBIC display, and the

charge collection current is greater. The concentration of deep levels is smaller.

- 4. The window for successful electron-beam annealing is broader and flatter than that for laser annealing. The required beam overlap is considerably less than that required for good laser annealing. Only when the electon-beam power approaches that required for melting does the charge collection efficiency fall off; it does so rapidly as a result of the formation of slip dislocations.
- 5. The thermal behavior of laser-induced defects is extremely interesting. A dominant, deep hole trap ($\rm E_{V}$ + 0.45eV) was observed right after sample preparation. However, the DLTS signal for this defect level decays with time at room temperature, and transmutes to another shallow level ($\rm E_{V}$ + 0.10eV). A subsequent low-temperature anneal of these samples restores the 0.45eV level. The restored concentration of this defect depends on the annealing temperature and time. By increasing the annealing temperature to 300°C, both the 0.45eV and 0.10eV defect levels can be eliminated. This defect transmutation behavior can also be stimulated by minority-carrier injection.
- 6. For the furnace-annealed control samples, rapid quenching from high temperature into water produces defects, observable by DLTS, which have the same energy level and annealing characteristics as the laser-induced defects. The concentration dependence of these defects on annealing temperature and quenching rate is quite the same as in the laser-induced quenched-in defect case.

- 7. By comparing these results with previous publications, a model involving interstitial Fe and Fe-B pair reactions was proposed to explain the peculiar annealing characteristics and recombination-enhanced defect reactions of both thermally-induced quenched-in defects and laser-induced defects in Si.
- 8. Possible sources of Fe contamination of Si were suggested. During chemical processing, Fe could easily be introduced onto the sample surface. Subsequent ion implantation would then drive this surface Fe into the bulk. Sputtering of Fe from various apertures of the implant accelerator could also take place. Fe originating from any of these sources would then diffuse into the Si, and be quenched on interstitial sites during laser annealing.

6.2 Discussion

The results described in this thesis are believed to be significant in at least three respects. First, the nonuniformity of charge collection in the EBIC display of laser-annealed samples demonstrates that serious, practical problems exist in utilizing CW laser annealing for device fabrication. It is clear that good-quality material suitable for device application can be obtained by laser annealing only by exercising considerable care, since the window for annealing is much narrower than had been indicated in the literature, and damage can easily be introduced by the laser. However, using scanned electron-beam annealing, the control tolerances to achieve good results are somewhat relaxed, and the quality

of the resulting material is generally superior. Second, the defects produced in Si during the fast heating and rapid cooling cycle of the laser-annealing process were demonstrated to be identical to those resulting from the rapid quenching of samples after furnace annealing. These quenched-in defects are identified as interstitial Fe and Fe-B pair reactions in Si. Although these defects can be eliminated at low temperature (300°C), they become precipitates in the region of the p-n junction, and this is certainly not desirable for device fabrication. Third, this thesis demonstrates the power of combining EBIC, photoluminescence and DLTS for minority-carrier investigations and defect studies. gives limited information about lattice structural defects. combining EBIC with TEM (or STEM), the electrical activity of these structural defects can be determined. While shallow levels remain the domain of luminescence studies, deep level spectroscopy (which is electrical in nature) provides a very useful technique complementary to luminescence, especially for radiative or non-radiative transitions where deep-lying levels are involved.

The EBIC results reported here led Baumgart et al. to conclude from their TEM measurements that dislocation loops of interstitial type are responsible for the dark-stripe image in the EBIC display. The DLTS results have aroused the attention of several leading research groups concerned with beam-annealing and/or defect studies. More recently, Miller⁽¹⁾ has found that the minority-carrier lifetime in Si changes during the transmutation between the

0.10eV and 0.45eV defect states. This result has serious implications for Si devices. For example, the switching speed of laser-annealed switching devices can be controlled by minority-carrier injection current. Other possible applications of these peculiar defect reactions, and the problems which they create for device applications, are currently being studied. (1)

This thesis has addressed a number of serious questions concerning the use of laser anneaing for Si material pocessing and device application. However, the results reported here raise additional questions, which should be the subject of future investigations. These questions include the following.

1. It is surprising that the Fe-related deep levels, which dominate the DLTS measurements reported here, were not reported in earlier DLTS measurements of CW laser-annealed Si by Johnson et al. (2) There are two possible explanations for this difference. First, the sample used by Johnson may have been stored at room temperature for too long a time, so that all of the 0.45eV defect level transmuted to 0.10eV level, which could then not be detected by DLTS at temperatures higher than 77K, the temperature range used in Ref. 2. The second possibility is that Fe was simply not present in their implanted samples. This second possibility seems unlikely when one considers the procedures used. Before carrying out their implantation and laser annealing, Johnson et al. usually performed high-dose implants into the back of the sample, followed by high-temperature furnace annealing. This was done to form a

good substrate ohmic contact at low temperature; however, this procedure is known to introduce additional Fe into Si, as described in Chapter 5. Thus, if anything, the samples used by Johnson should have obtained more Fe than those used in this work. This procedure was not needed in our work, because of the technique described in Chapter 3. More recently, Benton et al. (3) have reported that the same Fe-related defect levels have been found in incoherent CW arc lamp annealed Si.

- 2. The difficulties experienced in measuring defect luminescence, discussed in Chapter 4, remain for future, improved experiments to resolve. Recently, it has been reported that the so-called "P-line" in In-doped Si can be increased by more than two orders of magnitude after high temperature furnace heating and rapid quenching. (4) This enormous increase in P-line intensity has also been observed in our laboratory. This P-line shows <100> axial symmetry and has been attributed to Fe-In pairs. (4) It will be interesting to get suitable In-doped Si samples to correlate the P-line in photoluminescence with results using DLTS.
- 3. It is not clear whether the interstitial-type dislocation loops in the dark-stripe region of the EBIC display are directly related to Fe or not. Both EBIC and DLTS are sensitive to recombination centers whose energies are close to mid-bandgap. The H(0.45) level is the major deep level close to mid-bandgap which has been measured. Therefore, it seems likely that these dislocation loops are directly related to interstitial Fe. More experimental evidence is required to make this correlation clear.

4. It is not well understood why electron beam annealing produces results that are superior to laser annealing. This cannot be simply explained by the penetration of the electron beam into Si, since similar dark stripes have also been observed in CW $\rm CO_2$ laser-annealed samples. (5) A fundamental understanding of energy dissipation and electron-solid interactions is required to resolve this problem.

References

- 1. G.L. Miller, private communication.
- N.M. Johnson, P.J. Bartelink, M.D. Moyer, J.F. Gibbons,
 A. Lietoila, K.N. Ratnakumar, and J.L. Regolini, <u>Laser and Electron Beam Processing of Materials</u>, edited by C.W. White and P.S. Peercy (Academic Press, New York, 1979) p. 423.
- J.L. Benton et al., to be published in <u>Laser and Electron</u>
 <u>Beam Interactions with Solids</u>, edited by B.R. Appleton and
 G.K. Celler (North Holland, 1982).
- 4. J. Weber and R. Sauer, to be published.
- H. Baumgart, F. Phillip, and H.J. Leamy, to be published in <u>Laser and Electron Beam Interactions with Solids</u>, edited by B.R. Appleton and G.K. Celler (North Holland, 1982).

7.1. INTRODUCTION

InP has attracted considerable interest recently because of its application to semiconductor lasers, microwave devices and millimeter waves. For the latter of these devices, ion-implantation plays a particularly important role in the planar device processing of this material; a key problem, however, is the annealing of the implanted layer.

Lasers have been utilized to anneal the damage introduced by ion-implantation in a variety of materials. (1) Fairly extensive studies have been conducted for the case of implants into Si; it has been shown that high electrical activation with good mobility is obtainable. (2) Successful recrystallization takes place with both $CW^{(3)}$ and pulsed $^{(4)}$ beam annealing. Only a limited degree of success has been reported, however, for the case of III-V compound semiconductors, especially GaAs and InP. (5) Most of the successful annealing of implanted GaAs has been obtained with pulsed-beam techniques, (6) for which a higher degree of electrical activation can be obtained from samples implanted with a high-dose of n-type impurities, compared to convention ... y-annealed samples. On the other hand, low dose implants into GaAs have not been satisfactorily activated either by CW lasers (7) or pulsed beams. (8) Only one exception has been reported: when an electron beam was raster scanned in a random fashion to anneal Si⁺-implanted GaAs, reasonable carrier activation and high mobility resulted. (9) In this

case, however, the temperature of the sample was uniformly and gradually increased by the beam-annealing procedure, so that the annealing process approximates conventional furnace annealing. main difficulty encountered in activating low-dose implanted III-V compounds is generally believed to result from surface decomposition during the strong, highly-localized heating, even for very short laser pulses. In a recent study of the pulse-annealing of bare (i.e., unimplanted) epitaxial GaAs, (10) the resulting mobilities were degraded for a considerable distance (~0.3 µm) below the surface of the sample; this distance corresponds to the typical projected range of implanted ions. Therefore, compensation of implanted donors may occur by the defects produced by surface evaporation, resulting in poor electrical activation even though the implanted impurities may end up in proper substitutional sites. This may indeed represent a crucial limitation for laser annealing, if the temperature required for complete activation is substantially higher than that associated with the onset of surface decomposition. These thermal effects may differ in degree for the various III-V compounds. Much less is known about the beam annealing of implanted InP than for GaAs.

In this paper we present results concerning the electrical activation of Se-implanted InP using CW Ar^+ laser annealing, both with and without the use of phosphosilicate glass (PSG) as a dielectric cap. Recrystallization occurs by solid-phase epitaxy, so that no melting of the surface occurs, avoiding significant impurity redistribution. The next section describes the experi-

mental procedures used. Results and discussion are presented in Section III, including measurements of the extinction coefficient (k), the sheet resistivity (ρ) and the Hall mobility (μ). Slip line formation observed by optical microscopy, and the depth profiles of both ρ and μ are also discussed in this section. Finally, the results are summarized in Section IV.

7.2 EXPERIMENTAL

Semi-insulating (100) InP:Fe was used throughout this experiment. After samples were chemically-mechanically polished with Br-methanol, Se⁺ was implanted with an accelerating voltage of 160kV into samples which were heated to 200°C (HOT-implant) or held at room temperature (RT-implant). Phosphorus-doped SiO₂ (PSG), typically 1700Å thick, was deposited onto some of the samples at 320-380°C in a silicon reactor. The concentration of P in the PSG was chosen to be ~7-8%, so that the thermal expansion coefficient of the PSG was comparable to that of InP. (11) The composition of PSG was determined by electron microprobe analysis and Auger electron spectroscopy. (12) In some cases, Al metal was evaporated to cover the periphery of the sample; this was done to eliminate the temperature rise at the edge of the sample which usually occurs during annealing. In this way, very small samples could be uniformly annealed.

The multi-line output of a CW Ar laser was used for annealing, together with the laser-scanning system described previously, (13) consisting of a galvanometer mirror drive for scanning

in one direction, and a translation stage for sample motion in the perpendicular direction. The beam diameter was ~100 μ m, and each translation step after a galvanometer scan could be as small as 6 μ m. The scanning speed could be varied between 0.5 and 50 cm/sec.

The refractive index (n) and the extinction coefficient (k) of appropriate samples could be determined from ellipsometer measurements, using a 5461 Å light source. Electrical activation was evaluated from measurements of the sheet resistivity (ρ) and the Hall mobility (μ) of the samples which were processed photolithographically to produce standard van der Pauw mesa patterns.

Slip lines introduced by the laser scan were investigated using the Nomarsky differential interference (NDI) contrast mode of an optical microscope, either before or after processing by an electrochemical surface etching technique which will be described elsewhere. Finally, sample surfaces could be anodically stripped in order to profile the electron carrier concentration and mobility.

7.3 RESULTS AND DISCUSSION

A. <u>Extinction Coefficient</u>

The annealing behavior was first studied by ellipsometric measurements of n and k of the sample. Since we have observed no clear relationship between refractive index and scanned laser power, we restrict our interest to values of k, the extinction coefficient, as a function of laser power. In the samples shown in

Fig. 1, only the thermally-annealed sample has a PSG cap during annealing. As seen in the figure, k is larger for RT-implanted samples than for bare (unimplanted) InP, indicating a disordered state of the implanted sample. This value is dependent on implant dose because of the different degree of amorphism produced by different doses. However, k reaches a constant value for doses exceeding a critical implant dose of 5×10^{13} cm⁻²; this is consistent with results determined by changes in absorbed electron current (14) or by Rutherford backscattering (RBS). (15) A decrease in k is observed after annealing the RT-implanted sample, while maintaining the substrate at room temperature using a vacuum holddown stage. With increasing laser power, k decreases monotonically towards the value observed for bare InP. However, this limit is never reached, since the power first approaches \mathbf{P}_0 , the laser power which produces thermal decomposition of the surface. P_0 was determined by optical microscope observation of the surface after a series of laser single-scans (5 cm/sec velocity); the laser power is increased for each scan until evaporation of P is observed. For the 5×10^{13} cm⁻² dose in Fig. 1, changes in k take place fairly sharply compared to the gradual change observed for the higher-dose cases $(5\times10^{14} \text{ to } 5\times10^{15} \text{ cm}^{-2})$. The reason for this is not clear at this time; however, this implant dose may not produce a fully amorphous state, so that the recovery proceeds more easily even at lower laser power. A considerably sharper decrease of k has been observed for the case of CW laser-annealed Si, as seen in the inset to Fig. 1; in this case, complete electrical activation can be

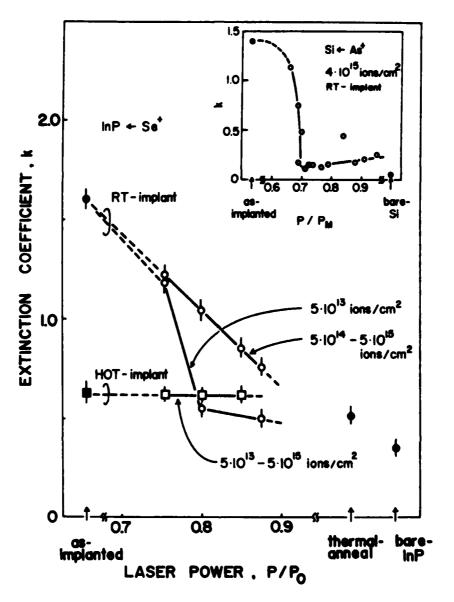


Fig. 7.1 The dependence of the extinction coefficient (k) of InP as a function of annealing laser power (P). P_0 is the power at which surface evaporation is observed using an optical microscope. Laser-annealed samples (open data points) had no PSG cap during annealing. The inset shows the extinction coefficient dependence upon laser power for Si. P_{M} represents the power at which the Si surface melts.

obtained $^{(16)}$ after the sharp, well-defined transition shown in the inset, which clearly corresponds to the amorphous-crystal transition.

The quite different behavior of k for InP compared with Si is believed to be due to a different recrystallization process; in fact, we have observed that the dependence of k on laser power for the case of GaAs is similar to that of InP. Apparently, this gradual decrease of k with laser power is typical of III-V compounds. In the case of GaAs, the recrystallization process during furnace anneal has been studied in detail. (17) At relatively low temperature (150-250°C) an amorphized layer can regrow epitaxially; however, a large density of crystal defects remains, which prohibits the electrical activation of implants and impurities (anneal stage I). An increase in anneal temperature (250-600°C) gives rise to a reduction in the density of crystal defects, resulting in partial electrical activation (anneal stage II). A high degree of electrical activation with correspondingly high mobility cannot be obtained, however, unless the sample is heated to a sufficiently high temperature (600-900°C) to anneal out the small defects and point defect complexes (anneal stage III). Ion-implanted Si, on the other hand, exhibits a single recrystallization stage, for which electrical activation and the removal of dense defects takes place at the same time. Hence a sharp decrease in k with laser power is observed.

In our laser-annealed samples, shown in Fig. 1, no electrical activation was observed even after the reduction in k. According

to the annealing behavior described above, this implies that although the sample underwent anneal stage I, a large density of crystal defects remains because the laser power was insufficient to completely remove disorder. Either the laser power must be increased, or the degree of residual damage decreased in order to obtain a high degree of electrical activity. Quite different results are obtained for HOT-implants, as is also shown in Fig. 1. In this case, the as-implanted sample shows a significantly lower value of k, and this value remains constant after laser annealing, indicating that the HOT-implant procedure can eliminate the annealing stage corresponding to the amorphous-crystalline transition (stage I). This result agrees with RBS measurements. $^{(15)}$ Nevertheless, even for HOT implants, a large density of extended defects remains, so that essentially no electrical activation is observed (and the value of k is still larger than the bare-InP case).

Among all the samples which were implanted HOT and annealed without a cap, only in one case was electrical activation observed, with sheet resistivity comparable to, and mobility somewhat lower than, thermally annealed samples. This case resulted when samples were laser annealed at elevated temperature; the substrate temperature (T_s) was held at 370-400°C. From the blue appearance of the surface of the sample, we deduced that the surface was oxidized during the anneal, which in turn allowed a higher laser power to be used. (18) Control of thickness of such an oxide is both desirable and possible. However, in our experiments the oxide developed

nonuniformly with a thicker oxide at the periphey of the sample. The mobility of the sample was consequently rather low, 200- $400 \text{ cm}^2/\text{Vsec}$, as will be discussed below.

B. <u>Electrical Activation</u>, Sheet Resistivity and Hall Mobility

A large number of samples implanted at doses between 5×10^{13} and 5×10^{15} cm⁻² have been investigated in this work; the results are summarized in Table 1. Let us first consider those samples that are annealed without any sort of capping layer. It is clear that good electrical activation (as indicated by sheet resistivity values comparable to or lower than thermally-annealed samples) is achieved only for high-dose samples. For the lower dose, uncapped samples, we believe that the implanted donor concentration was too low to overcome the density of compensating defect centers introduced by surface decomposition, as has been previously suggested by Davies et al. (10) Therefore, for the 5×10^{15} cm⁻² dose sample ($T_{\rm s} \sim 400^{\circ}{\rm C}$), the implanted impurity concentration must be well in excess of the defect density; this results in reasonable electrical activation but low mobility.

From the results of these studies it is clear that, in order to achieve good electrical activation, higher power must be deposited in the sample in order to achieve the third stage of annealing; to reach such power without surface decomposition, a dielectric cap is necessary. There are several possible caps which could be used to prevent thermal decomposition. PSG is one choice,

TABLE 1. Summary of electrical activation obtained for laser-annealed samples with different implant doses, both with and without a PSG cap. The substrate temperature (T_S) is indicated. Comparison is made with a thermally-annealed control-sample. Sheet resistivity ρ (Ω/\Box) and mobility μ (cm²/Vsec) are given by the upper and lower numbers, respectively, in each pair. The word NO signifies that these parameters were unmeasurable, while blanks represent the absence of an experiment.

	1	LASER-ANNEALED			
DOSE		NO PSG CAP		PSG	
(cm ⁻²)	Timplant	T _s ~ RT	T _s ~ 400C	T _s ~ 400C	THERMALLY ANNEALED
3x10 ¹²	RT				ρ = 1080
	нот			3400 780	μ = 1900
5x10 ¹³	RT	NO		1800 60	100
	нот		NO	120 1430	1550
1x10 ¹⁵	RT	NO			25
	нот			22 790	1040
5 x 10 ¹⁵	RT	NO			18
	нот	NO	75 400		910

which has two obvious advantages: first, the film contains P, which effectively prevents the evaporation of the host atom, and secondly, the concentration of P in the film can be chosen to match the thermal expansion coefficient of InP. HOT-implanted samples with PSG which were annealed at $T_c = 380-400^{\circ}\text{C}$ showed good electrical activation with reasonable mobility; for the case of the $5\times10^{13}~\text{cm}^{-2}$ dose sample, the best values obtained were ρ = 100 Ω/\Box and $\mu = 1550 \text{ cm}^2/\text{Vsec}$, as shown in Table 1. These values were observed using samples of dimension 6×6 mm², without any Al coating, using a laser-scanning velocity of 3 cm/sec. The appearance of the oxide produced during annealing suggests that the annealing was often non-uniform, as mentioned above; the maximum temperature attained was therefore believed to be different between the edge and the center of the sample. To prevent this, Al was evaporated after deposition of the PSG and removed by photolithography and etching from all but the periphery of the sample; this simultaneously produced a van der Pauw pattern on the 3×3 mm² This procedure can be used to eliminate an undesirable temperature rise at the edge of the sample. In addition, this procedure eliminates the processing step usually needed to etch a mesa, because the implanted region underneath the A ℓ -film is not electrically activated, and therefore has a sufficiently high resistivity to allow sheet resistivity measurements of the annealed portion above.

Using the sample configuration described above, the "annealing window" for successful annealing was determined by varying laser

power and scan speed, while monitoring the sheet resistivity and the Hall mobility. The results are shown in Fig. 2 for three different values of scan velocity. Here, V is a normalized, dimensionless velocity which represents the ratio of the dwell time of the laser beam to the time required to reach the steady-state temperature condition; V = va/2D, where v is the velocity of the laser beam (cm/sec), a is the radius of the beam spot (55 μ m in this case) and D is the thermal diffusivity (0.066 cm²/sec) calculated from the known values of the thermal conductivity $(0.13 \text{ W/cm-deg})^{(19)}$ and specific heat C_n $(1.99 \text{ Wsec/cm}^3 \text{deg})^{(20)}$ at 800°C. Apparently, as a result of using the PSG cap, higher power could be delivered to produce electrical activation for each value As the laser power increases, the sheet resistivity decreases; however, the mobility reaches a peak and begins to decrease at still higher power. From observations of the surface using an optical microscope, we found that these samples typically contain slip lines. The limitation of mobility is therefore believed to be due to the increase in slip line density. Similar results have been reported for GaAs. (21,22) for which slip lines are easily introduced during anneal due to a large thermal gradient. The formation of slip is probably not due to the stress between the PSG cap and the InP, because slip can develop even in a bare InP sample by using a high power laser scan. Fig. 3 shows several examples of the development of slip lines, observed using NDI contrast microscopy. By comparing Fig. 3 with Fig. 2, it can be seen that slip lines develop at a fairly low power, for which

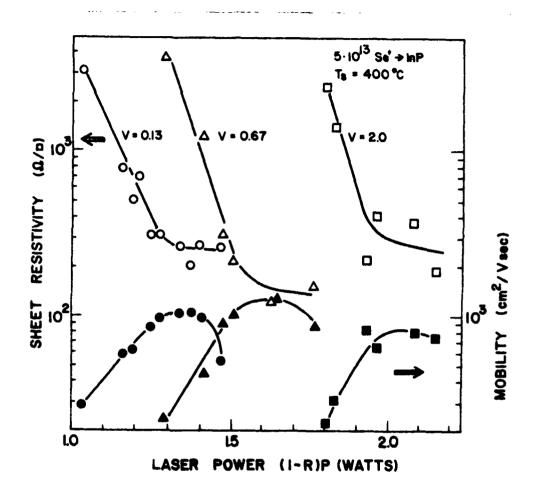


Fig. 7.2 Sheet resistivity (open points) and Hall mobility (solid points) of Se⁺-implanted (5×10^{13} cm⁻², 160KV) and laserannealed InP with a PSG cap, plotted as a function of laser power with three different normalized scan velocities (V). V = $(a^2/D)/(2a/v)$ where a is the radius of the beam ($55 \mu m$), D is the average thermal diffusivity ($0.066 \text{ cm}^2/\text{sec}$ at 800°C), and v is the actual beam velocity (cm/sec). The laser power is plotted after correcting for reflection loss from the PSG surface. Samples are 3×3 mm², with a clover-leaf pattern surrounded by evaporated Al at the periphery of the sample.

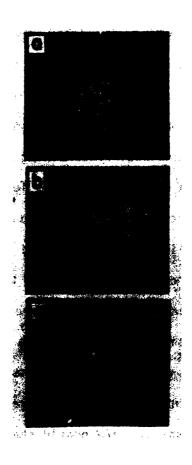


Fig. 7.3 Nomarsky differential interference (NDI) contrast optical micrographs for laser-annealed samples using a normalized beam-scan velocity (V) of 0.13, and different laser power. Annealing powers employed are (a) 1.19W, (b) 1.34W, and (c) 1.41W.

the sheet resistivity has not yet reached a minimum value. As the power increases, the density of slip lines increases remarkably, as seen in Fig. 3a and b. However, the decrease in mobility which occurs upon further increase in laser power must be due to the creation of extended surface defects other than a higher density of slip lines, since no dramatic increase in slip line density is observed in Fig. 3c. In the extreme high power case, cracks in the PSG cap, and the occasional intermixing of InP and PSG were observed; in this case the surface is no longer flat, resulting in severe degradation of the mobility. It has been reported (21) that the density of slip lines can be reduced if the velocity of the laser beam is slow enough to reduce the thermal gradient in the beam-scanning direction. However, we have obtained contradictory results: a lower density of slip lines is observed in the sample scanned at higher beam velocity. This is seen in Fig. 4, where NDI photos are seen for three different scan velocities. The mobility values for the three samples are nearly the same, whereas V varies from 0.13 to 2.0, and minimum slip is observed for V = 0.67. In fact we have achieved higher maximum mobility and lower sheet resistivity with V = 0.67 compared to the values with V = 0.13. Further increases in V, however, result in lower maximum mobility, probably because the dwell time was insufficient to anneal out the defects. This is not surprising for the case V = 2.0.

The influence of slip on the electrical properties of InP seems somewhat different from the GaAs case, reported by Fan et al. (21) In their investigations, slip lines were introduced at

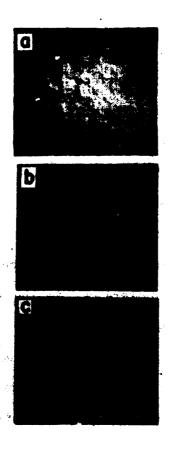


Fig. 7.4 NDI-contrast optical micrographs for samples annealed with different normalized scan velocity (V) and power. Annealing laser power and scanning velocity are (a) 1.34W and V = 0.13, (b) 1.51W and V = 0.67, and (c) 2.08W and V = 2.0.

high scan speeds by increasing the laser power; the sheet carrier concentration was observed to decrease with laser power, until anistropy was observed in the van der Pauw measurements. On the other hand, in the InP results reported here, the sheet carrier concentration always increases monotonically with laser power until heavy deterioration of the surface is observed. The mobility also increases, despite the fact that a large increase in the density of slip lines is observed (Fig. 3a and b). No anisotropy was observed in the measurement of the sheet resistivity, except that etching proceeds very rapidly along the slip lines during the photolithographic process used to make the mesa. The differences of the dependence of the electrical properties on slip between InP and GaAs might be due to differences in the electrical activity of dislocations in these materials; for InP, surface states may not produce energy levels in the forbidden gap, so that non-ionized dislocations do not act as severe scattering centers. Nevertheless, slip lines are undesirable, even if they do not act as mobility killers, because they tend to limit the maximum mobility attainable, and increase surface roughness, a potentially serious problem for device processing. Possible ways to eliminate the formation of slip include (a) increasing the substrate temperature (T_s) to reduce the thermal gradient, and (b) increasing the scan speed in order to shorten the dwell time. The latter case is in fact realized in the case of annealing implanted Si with nsec pulsed laser beams, for which very rapid cooling of the crystal takes place, and no dislocation formation results. (23) In other

words, the velocity of dislocation motion is so slow compared to the cooling time, that the large strain which would develop slip is frozen in the crystal. There is little reliable data concerning dislocation motion in InP; we therefore used the velocity of dislocation in Si. (24) The actual beam velocity, v=48 cm/sec (corresponding to V=2.0) is comparable to or faster than the velocity of dislocation motion in Si (10 cm/sec). The reduction in the density of slip lines with increasing scan velocity, shown in Fig. 4, can be explained in this way. However, from the point of view of defect annealing, this dwell time is so short that a higher temperature is required for the complete removal of lattice defects.

The temperature due to laser heating was estimated using the approach of Lax; $^{(25)}$ the maximum temperature estimated in this way was 670°C at (1 - R)P = 1 watt and 850°C at 1.5 watts with $T_{\rm S}$ = 400°C and a = 55 μm , assuming that the beam is stationary (V = 0; cf. Fig. 5). For the actual moving beam, the maximum temperature rise was estimated to be 650-800°C within the laser power range of 1-1.5 watts when V = 0.13, and 690-780°C at 1.8-2.15 watts when V = 2.0. Temperatures for the non-stationary beam case were determined by shifting the curve obtained for the stationary case. A multiplying factor was used which is the ratio between values of P_0 for which the surface evaporation pattern appears identical for each different value of V. However, regardless of the scan velocity, cracks and/or heavy surface deterioration were observed, as described previously, at substrate temperatures approaching

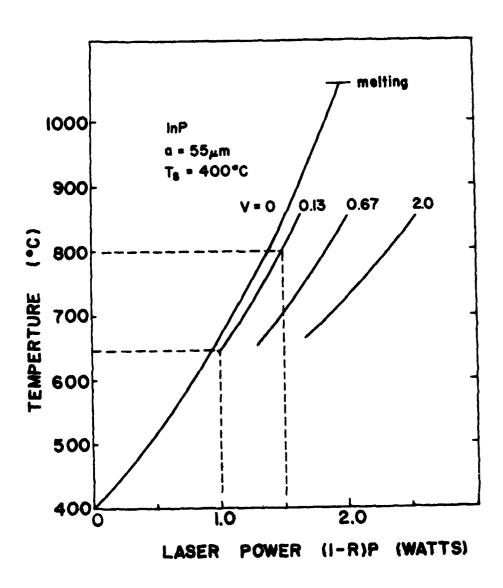


Fig. 7.5 The temperature rise induced by the laser local heating. For the stationary beam case (V = 0), the temperature is calculated including the effect of nonlinear thermal conductivity on temperature, with a substrate temperature T_s of 400°C. For the moving beam case, the curve is simply shifted by a factor which is determined experimentally (see text).

800°C. Therefore, simply decreasing the dwell time and increasing the laser power may not be a suitable way to optimize annealing.

In the range of dose studied here higher sheet carrier concentration, compared to that of the control sample, has been observed for high dose $(5\times0^{14}~\rm cm^{-2})$ samples. This may result from the fact that CW laser annealing is capable of activating implanted impurities whose concentration exceeds the solid solubility. This is the case for the pulsed-beam annealing of GaAs $^{(6)}$ or Si $^{(25)}$ and for the CW laser annealing of Si. $^{(27)}$ On the other hand, in the low-dose regime $(3\times0^{12}~\rm cm^{-2})$, lower mobility has been observed than for the $5\times10^{13}~\rm cm^{-2}$ dose sample. The reason for this behavior is simply not understood.

C. Depth Profiles of the Carrier Concentration and Mobility

Stripping of the layer by anodic oxidation and etching was used to profile the electron carrier concentration and the Hall mobility. $^{(28)}$ The result for a laser-annealed sample, as shown in Fig. 6, indicated little or no redistribution of the implanted species; this result was expected for CW laser annealing. However it was found that the range of the profile was significantly displaced from the calculated LSS profile. This can be explained by the expected mixing of PSG and InP over a distance of 200A; a similar effect has been reported in the case of SiO₂ on InP. $^{(29)}$ The LSS curve drawn in the figure was shifted by 200A towards the surface, and agrees well with the measured carrier profile. This indicates that ~200A of InP was removed during etching of the PSG

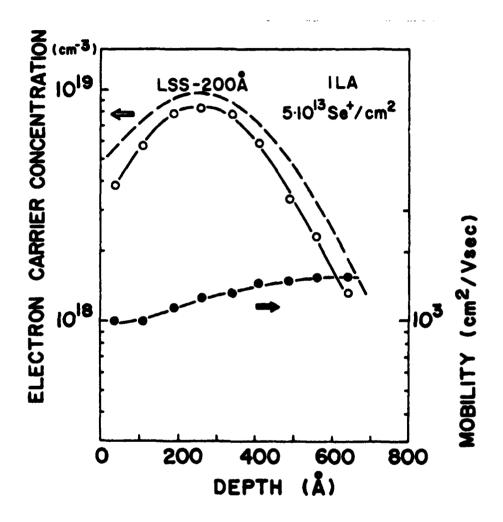


Fig. 7.6 Depth profiles of electronic carrier concentration (open circles) and Hall mobility (solid circles). The broken line represents a calculated LSS range profile, but shifted by 200A towards the surface to include the effect of PSG-InP intermixing.

cap. This intermixing of PSG and InP was also observed for the control sample, which was furnace-annealed in flowing N_2/H_2 at 750°C for 15 min.

Comparison of the concentration and mobility profiles of samples annealed at different laser power shows that there are differences in the mobility profiles, whereas concentration profiles are quite similar, differing only in absolute value. For samples annealed at low power, the mobility is lower at the surface; on the other hand, the mobility is lower below the surface for samples annealed at higher power. In all cases, however, the measured values of mobility are still lower than the values calculated from the carrier concentration measurements. These results suggest that laser-induced-damage and/or slip formation governs the mobility. In the case of the control sample, the mobility is lower in regions where the carrier concentration is high, indicating that the mobility is limited by ionized scattering, rather than by slip-line formation. In fact, slip lines were not observed in the control sample. However, this sample showed a slighlty broadened carrier profile due to the diffusion of implanted Se, as expected for furnace annealing.

It is also interesting to investigate the effect of AL masking, used to avoid excess heating at the edge of the sample, on mobility. Surprisingly, we found that improved values for ρ and μ are obtained without the AL mask (values shown in Table 1 for a dose of 5×10^{13} cm⁻²) compared to the values obtained when AL masking is used (data shown in Fig. 2). This fact may be under-

stood by assuming that the absence of the Al mask allows the overall substrate temperature to increase somewhat, so that less slip formation occurs, and the annealing mechanism is closer to that of the furnace anneal.

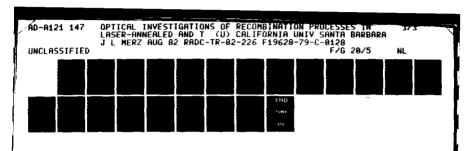
7.4 CONCLUSION

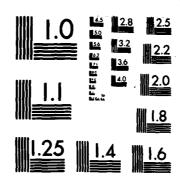
InP implanted with Se was successfully annealed by a CW Artion laser utilizing phosphosilicate glass as a dielectric cap. From the measurement of the extinction coefficient of the implanted layer a gradual anneal stage was observed, instead of the sharp recrystallization seen for Si. A wide range of Se dose was activated for hot implants when the substrate was heated to 400°C during laser anneal. For low-dose implants, μ was somewhat lower than was obtained in thermally-annealed control samples. medium doses, p and p become comparable to the controls, whereas in the high-dose cases, ρ can be lower than the thermal-anneal values. The best results obtained in this work, which were comparable to furnace-annealed control samples, were observed for a HOT-implant dose of $5\times10^{13}~\text{cm}^{-2}$, and laser annealing through a PSG cap with $T_c = 400$ °C. In every case no impurity redistribution was found in laser-annealed specimens. The formation of slip lines, which can be reduced but not eliminated by rapid scanning, is found to have a serious negative effect on the electrical properties of laserannealed InP.

REFERENCES

- Laser and Electron-beam Solid Interactions and Material Processing, edited by J.F. Gibbons, L.D. Hess and T.W. Sigmon (Elsevier, New York, 1981).
- A. Gat, J.F. Gibbons, V.R. Deline, P. Williams and C.A. Evans, Jr., Appl. Phys. Lett. 32, 276 (1978).
- 3 J.S. Williams, W.L. Brown, H.J. Leamy, J.M. Poate, J.W. Rodgers, D. Rousseau, G.A. Rozgonyi, J.A.Shelnutt and T.T. Sheng, Appl. Phys. Lett. 33, 542 (1978).
- 4 G. Foti, E. Rimini, W.S. Tseng and J.W. Mayer, Appl. Phys. <u>15</u>, 365 (1978).
- F.H. Eisen, <u>Laser and Electron-Beam Processing of Materials</u>, edited by C.W. White and P.S. Peercy (Academic Press, New York, 1980) p. 309.
- 6 S.G. Liu, C.P. Wu and C.W. Magee, <u>ibid</u>, p.341.
- 7 C.L. Anderson, H.L. Dunlap, L.D. Hess, G.L. Olson and K.V. Vaidyanathan, <u>ibid</u>, p. 334.
- 8 M.H. Badawi, B.J. Sealy, K.G. Stephans and J.A. Akintude, Japan. J. Appl. Phys. 19, Supp. 19-1, 139 (1980).
- 9 N.J. Shah, H. Ahmad, J.R. Sanders and J.F. Singleton, Electron. Lett. 16, 433 (1980).
- 10 D.E. Davies, J.P. Lorenzo, and T.G. Ryan, Appl. Phys. Lett. 37, 612 (1980).
- 11 J.P. Donnelly and C.E. Hurwitz, Appl. Phys. Lett. <u>31</u>, 418 (1977).

- 12 G. Queirolo and G.U. Pignatel, J. Electrochem. Soc. <u>127</u>, 2438 (1980).
- 13 M. Mizuta, N.H. Sheng and J.L. Merz, Appl. Phys. Lett. <u>38</u>, 453 (1981).
- W. Rothemund and C.R. Fritzsche, J. Vac. Sci. Technol. <u>16</u>, 968 (1979).
- 15 E.F. Kennedy, Appl. Phys. Lett. 38, 375 (1981).
- 16 M. Mizuta, N.H. Sheng, J.L. Merz, A. Lietoila, R.B. Gold and J.F. Gibbons, Appl. Phys. Lett. 37, 154 (1980).
- 17 J.S. Williams and H.B. Harrison, p. 209 in Ref. 1.
- 18 Y.I. Nissim and J.F. Gibbons, in Ref. 1.
- 19 I. Kudman and E.F. Steigmeiner, Phys. Rev. 133A, 1665 (1964).
- 20 M. Boutard and P. Pinard, J. de Physique 33, 787 (1972).
- J.C.C. Fan, J.P. Donnelly, C.O. Bozler and R.L. Chapman, Proc. 7th Int. Symp. on GaAs and Related Compounds, St. Louis, 1978 (Institute of Physics, London, 1979), p. 472.
- 22 C.L. Anderson, H.L. Dunlap, L.D. Hess and K.V. Vaidyanathan, <u>Laser-Solid Interactions and Laser Processing</u>, edited by S.D. Ferris, H.J. Leamy and J.M. Poate (AIP, New York, 1979), p. 585.
- 23 J. Narayan, R.T. Young and C.W. White, J. Appl. Phys. <u>49</u>, 3912 (1978).
- 24 V.N. Erofeev, V.I. Nikitenko and V.B. Osvenski, Phys. Status Solidi <u>35</u>, 79 (1969).
- 25 M. Lax, Appl. Phys. Lett. <u>33</u>. 786 (1978).





MICROCOPY RESOLUTION TEST CHART
DARDS-1963-A

- 26 C.W. White, S.R. Wilson, B.R. Appleton and R.T. Young, J. Appl. Phys. <u>51</u>, 738 (1980).
- 27 A. Lietoila, J.F. Gibbons, T.J. Magee, J. Peng and J.D. Hong, Appl. Phys. Lett. <u>35</u>, 532 (1979).
- 28 J.P. Lorenzo, D.E. Davies and T.G. Ryan, J. Electrochem. Soc. 126, 118 (1979).
- 29 T. Nishioka and Y. Ohmachi, J. Appl. Phys. <u>51</u>, 5789 (1980).

APPENDIX A. STEPPING-MOTOR CONTROLLER

SLO-SYN stepping motor, as shown in Fig. A.1, operates on phase-switched d-c power. The motor shaft advances 200 steps per revolution (1.8° per step) when a four-step input sequence as shown in Fig. A.2(b) is used, and 400 steps per revolution (0.9° per step) when an eight-step input sequence (Fig. A.2(c)) is used. One revolution of shaft rotation moves the translation stage 0.1 in. The basic circuit design requirement is to generate the correct switching sequence, as shown in Fig. A.2(b) and (c), from the input square wave of Fig. A.2(a), in order to excite the stepping motor. The basic functions of this controller can be seen from the four switches (SW1 to SW4 in Fig. A.3) on the front panel of the controller.

- (a) SW1 (ON/RESET): Before start or changing the rotating direction of the stepping motor, this switch must be set in "RESET" postion which defines the initial states shown as the dashed line in Fig. A.2.
- (b) SW2 (Forward/Reverse): This switch controls the rotating direction of the stepping motor which drives the translation stage in either forward or reverse direction.
- (c) SW3 (12 μ m/6 μ m): Choose the number of steps the stepping motor takes to complete one shaft revolution, i.e. select either the switching sequence of Fig. A.2(b) or Fig. A.2(c) to drive the stepping motor.

(d) SW4 (x1, x2, x4): This switch controls the distance of motion of the translation stage for each x-step in CW laser annealing as shown in Fig. 2.1. The distance per step is determined by the setting of SW3 multiplied by the setting of SW4. The minimum x-step of the translation stage is therefore 6 μ m and maximum is about 50 μ m.

Circuit Description

There are four flip-flops in Fig. A.4, two in each SN7474. Three of these flip-flops are used to define the initial state and generate the switching sequence shown in Fig. A.2(b) from the input The stepping motor then can be square wave of Fig. A.2(a). triggered by one step at positive transition edges of the input square wave. The logic circuit shown in Fig. A.3 generates the switching sequence of Fig. A.2(c) which drives the stepping motor 400 steps per revolution. The outputs of the circuits shown in Fig. A.4 or Fig. A.5 are used to control the on-off state of the power transistors in Fig. A.6; these supply the power to drive the stepping motor. The circuit of Fig. A.7 generates a single pulse or double pulse at the rising and falling edges of the input square The outputs of Fig. A.7 can go through SW4 to replace the original input of Fig. A.2(a) to generate the switching sequence. Therefore, the stepping motor can be triggered two or four steps at the edges of Fig. A.2(a) which moves translation stage farther for each transition. In order to further increase the step size, a

sawtooth generator must be used to drive the galvanometer of the laser-annealing system. The square wave of Fig. A.2(a) first passes through an external counter and an AND gate and is fed to the stepping motor controller input. The sawtooth generator is triggered by the falling edge of the counter ouput. Therefore, the stepping motor can move a large number of steps, depending on the counter during the period when the galvanometer stays fixed. For the case of Fig. A.7, if a divide-by-4 counter is used, the step size between successive scans is about 100 μ m if SW3 is in the position corresponding to 12 μ m.

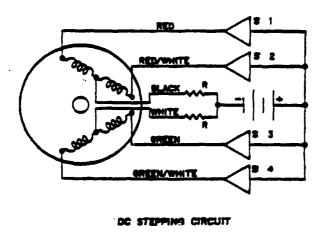
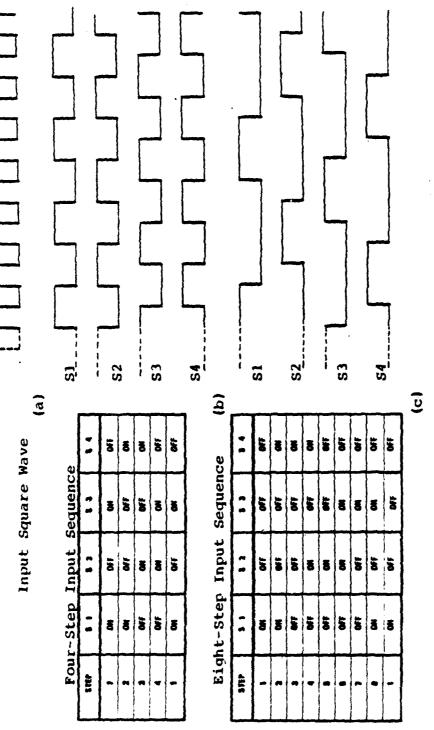


Fig. A.1 Schematic of a four-phase stepping motor.



revolution. To reverse direction of motor rotation, perform switching steps from bottom to top. Dashed lines are the initial states of the stepping motor. (b) Switching sequences for 200 steps per for 400 steps per (a) Input square waveform of the stepping-motor con-(c) Switching sequences revolution. troller. A. 2 Fig.

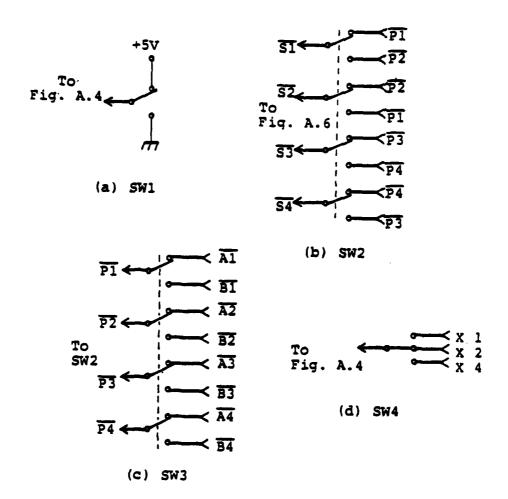


Fig. A.3 Four switches on the front panel. (a) SWI (ON/RESET). (b) SW2 (Forward/Reverse). (c) SW3 (12 μ m/6 μ m). (d) SW4 (Multiple Steps: x1, x2, x4).

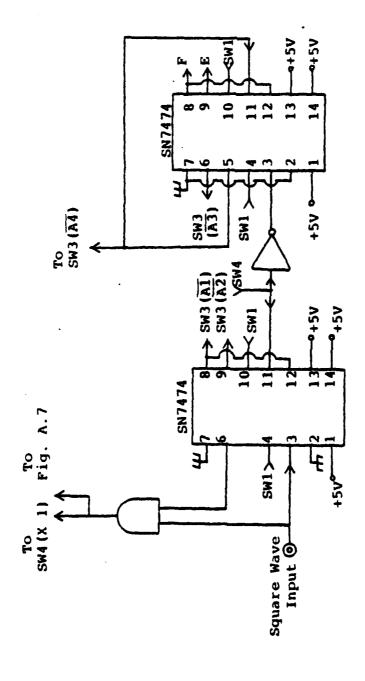


Fig. Fig. A.4 Flip-flops to generate the switching states of

A.2(b) for 200 steps per revolution.

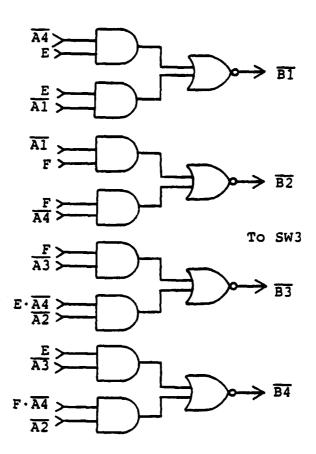


Fig. A.5 Logic circuit diagram to generate the switching states of Fig. A.2(c) for 400 steps per revolution.

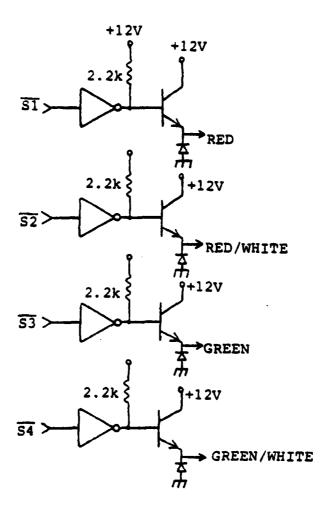


Fig. A.6 Power transistors (MJ 802) to drive the stepping motor.

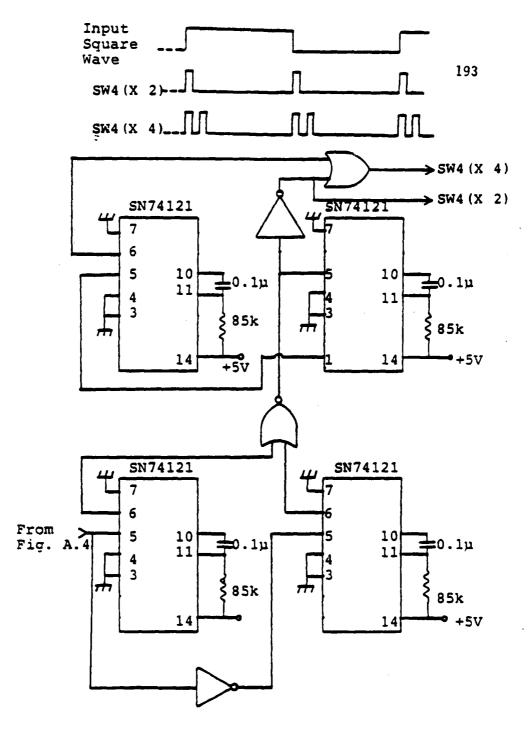
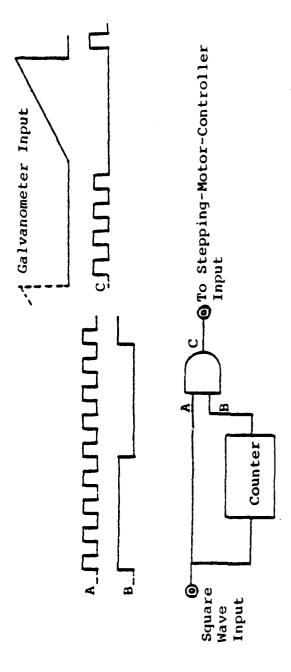


Fig. A.7 Circuit diagram to generate multiple pulses at the positive and negative transition edges of the input square wave.



A sawtooth generator triggered at the falling edges of the counter output (8) is used as The number of steps by which the stepping motor moves during the period when the galvanometer stays fixed depends on the counter. If a divide-by-4 counter used, it moves eight steps and A block diagram to generate waveform of C for steppingthe galvanometer-controller input. motor controller input. corresponds to ~100 µm. Fig. A.8

APPENDIX B: DLTS SIGNAL PROCESSOR

A DLTS system is simply a combination of instruments. The signal analyser used in DLTS is often a commercial double boxcar averager. This instrument is considerably more complex than needed, and becomes unnecessarily expensive for a DLTS measurement. A simple and cheap signal processor, which performs basically the same functions of a commercial double boxcar in a DLTS system, has been built.

The function block diagram is shown in Fig. B.1. The capacitance transient signal from capacitance meter goes to both Channel A and B and is amplified by a factor of ten in both channels. This amplified transient signal is sampled at t_1 in Channel A and at t_2 in Channel B. The sampling pulses at t_1 and t_2 are generated in a digital sampling signal generator to be described later. Therefore, the capacitance transient is sampled and held at $C(t_1)$ in Channel A and at $C(t_2)$ in Channel B. These two sampled signals are amplified by a factor of ten in both channels and fed to a differential amplifier which forms the difference $C(t_1) - C(t_2)$. Finally, this differential output goes through the output filter whose integration time constant can be varied.

The circuit of the digital sampling pulse generator is shown in Fig. B.2. Two sampling pulses are generated in two indentical circuits respectively, one for Channel A and the other for Channel B. NE555 controls the delay time which can be varied by adjusting $R_{\rm D}$ and $C_{\rm D}$. The value of $C_{\rm D}$ determines the range of maximum delay

time, while the R_D (a ten-turn variable resistance pot) is a fine adjustment for each range. In the present system, there are five ranges of delay time to be chosen: 0.1 ms, 1 ms, 10 ms, 100 ms, and 1 sec. Therefore, delay times t_1 and t_2 of the sampling pulses can be adjusted independently from the front panel. The sampling pulse width and R_T is a fine adjustment. In the present system, three ranges of pulse width can be chosen from the rear panel: 5 μ s, 50 μ s and 500 μ s. These two sampling pulses, at different delay time t_1 and t_2 , are then fed to trigger the sampling-hold circuits in Channel A and B of Fig. B.3, respectively.

In Fig. 8.3, the capacitance transient is first amplified by a factor of ten by the operational amplifier CA3140 in both channels. CA3080 and FET 3N138 perform the sampling-hold function which is triggered by the sampling pulses from Fig. B.2. The sampled signals are amplified by the operation amplifier CA3140, whose gain can be adjusted by a 1 kilo-ohm trim resistor. The difference of these two sampled signals in Channel A and B is calculated by the operational amplifier μ A741. The last two operational amplifiers comprise a low pass filter whose integration time constant can be varied from the front panel.

The circuit described here utilises inexpensive, off-the-shelf ICs and is much easier to operate and much cheaper than a commercial double boxcar.

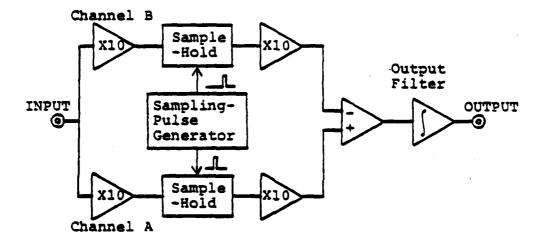


Fig. B.1 Block diagram of the DLTS signal processor.

Received somess sections postable reserved today

CONTRACTOR DESCRIPTION OF THE PROPERTY OF THE

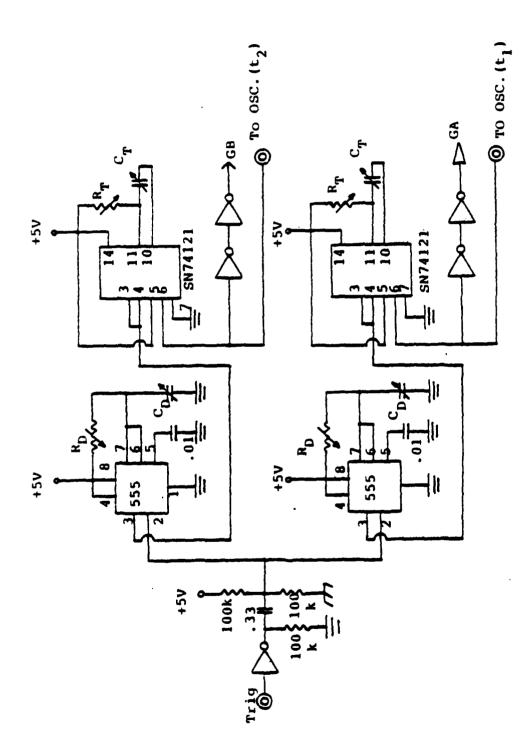


Fig. B.2 Circuit diagram of the digital sampling pulse generator.

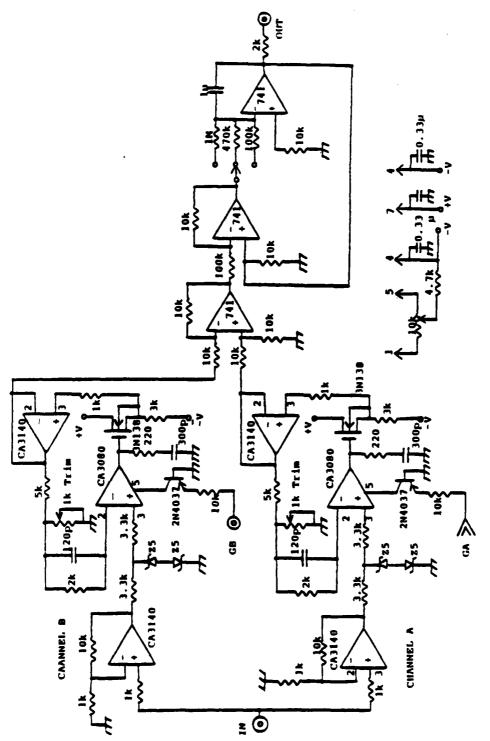


Fig. B.3 Circuit diagram of the analog part of the DLTS signal

processor.

APPENDIX C: TEMPERATURE-SCANNING UNIT

The circuit schematic to scan the temperature for DLTS measurements is shown in Fig. C.1. There are two modes of operation for this circuit. In the automatic control mode, the temperature controller output goes to the non-inverse input of the upper operational amplifier and to the inverse input of the lower operational amplifier. The other input of the upper operational amplifier is fixed at about OV, so that its output is equivalent to the temperature controller output. The non-inverse input of the lower operational amplifier is fixed at about 10V, and its output is equivalent to 10V minus the temperature controller output. Therefore, when the temperature controller output increases, the output of the upper operational amplifier increases while the output of the lower operational amplifier decreases, and vice versa. upper output controls the power supplied to the heater in the gas flow dewar right below the sample, and the lower output controls the power to the heater in the liquid nitrogen dewar. In the manual mode operation, the inputs connected to the temperature controller output is switched to a manually adjusted dc voltage. It is recommended that the heaters from the dc power supply be disconnected using the front panel switches when the heaters are taken out of the dewars to avoid any possible electrical shock.

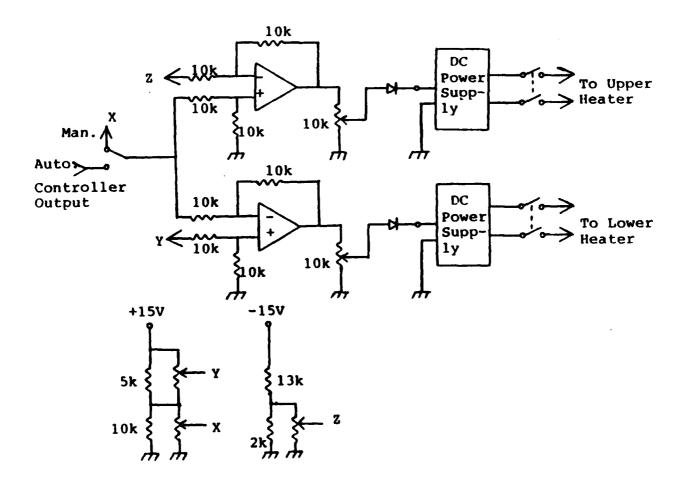


Fig. C.1 Cicuit diagram of the temperature scanning system for DLTS measurements.

MISSION of Rome Air Development Center

RADC plans and executes research, development, test and selected acquisition programs in support of Command, Control Communications and Intelligence (C³I) activities. Technical and engineering support within areas of technical competence is provided to ESD Program Offices (POs) and other ESD elements. The principal technical mission areas are communications, electromagnetic guidance and control, surveillance of ground and aerospace objects, intelligence data collection and handling, information system technology, ionospheric propagation, solid state sciences, microwave physics and electronic reliability, maintainability and compatibility.

END

FILMED

10-85

DTIC